On the Role of Wind Shear and Cloud Droplet Sedimentation on Entrainment in Stratocumulus

Bernhard Schulz

Hamburg 2019

On the Role of Wind Shear and Cloud Droplet Sedimentation on Entrainment in Stratocumulus

Bernhard Schulz

Hamburg 2019

Bernhard Schulz
aus Tübingen, Deutschland

Max-Planck-Institut für Meteorologie
The International Max Planck Research School on Earth System Modelling
(IMPRS-ESM)
Bundesstr. 53
20146 Hamburg

Universität Hamburg
Geowissenschaften
Meteorologisches Institut
Bundesstr. 55
20146 Hamburg

Tag der Disputation: 5. April 2019

Folgende Gutachter empfehlen die Annahme der Dissertation:
Prof. Dr. Gualtiero Badin
Prof. Dr. Juan Pedro Mellado

Vorsitzender des Promotionsausschusses:
Prof. Dr. Dirk Gajewski

Dekan der MIN-Fakultät:
Prof. Dr. Heinrich Graener

Bernhard Schulz

Max-Planck-Institut für Meteorologie
Bundesstraße 53
20146 Hamburg

ABSTRACT

How low clouds respond to global warming is one the most important and most challenging questions in climate science. One reason is the limited understanding of how lower-tropospheric mixing processes—like entrainment—affect cloud lifetimes. In this regard, stratocumulus clouds are particularly important due to their large albedo and particularly challenging to quantify due to their dependence on meter- and submeter-scale mixing processes. Cloud-top wind shear and droplet sedimentation can substantially alter entrainment, however, important aspects of both processes remain unclear. For instance, even though it is well known that droplet sedimentation weakens entrainment and wind shear enhances entrainment, there is no consensus on the relevance of these two processes. For these reasons, this dissertation investigates wind-shear and droplet-sedimentation effects on cloud-top entrainment in stratocumulus by means of direct numerical simulations, resolving the relevant meter- and submeter-scale mixing processes.

Three main findings are obtained. First, we find that, at least for subtropical conditions, sedimentation weakening of entrainment is sufficiently strong to balance shear enhancement of entrainment, namely, sedimentation weakens the entrainment velocity by up to 40% while shear enhances the entrainment velocity by up to 40%. This demonstrates that both processes can be equally important for determining entrainment, which suggests that changes in the droplet size distribution are more important than previously thought. Second, the choice of the reference height where the entrainment velocity is calculated matters for some quantities but not for others. In particular, the separate contributions to the entrainment velocity from mixing, radiative, and evaporative cooling depend strongly on the choice of the reference height, even though the net entrainment velocity depends only weakly on the choice of the reference height (in a quasi-steady state). Together, the first and second point indicate that entrainment velocity parametrizations—as needed in mixed layer models—should estimate the separate contributions to the entrainment velocity at the same reference height and should pay equal attention to shear and to sedimentation effects. Third, two critical cloud-top velocity jumps are identified. Firstly, shear only enhances entrainment if the cloud-top velocity jumps exceeds its critical value $(\Delta u)_{\mathrm{crit}}$; for $\Delta u < (\Delta u)_{\mathrm{crit}}$ shear effects are negligible. Secondly, shear enhanced entrainment does not necessarily deplete the cloud sufficiently to reduce the net radiative cooling of the cloud. For this shear effect to happen, the cloud-top velocity jump needs to exceed its depletion value $(\Delta u)_{\mathrm{dep}}$. Both critical cloud-top velocity jumps are provided as function of in-cloud and free-tropospheric conditions and one finds $(\Delta u)_{\mathrm{crit}} \simeq 1 - 4\,\mathrm{m\,s}^{-1}$ and $(\Delta u)_{\mathrm{dep}} \simeq 3 - 10\,\mathrm{m\,s}^{-1}$. All in all, this dissertation demonstrates the importance of wind-shear and droplet-sedimentation effects for cloud-top entrainment and by doing so, highlights the importance of small-scale mixing processes for stratocumulus.

ZUSAMMENFASSUNG

Wie Wolken auf die globale Erderwärmung reagieren, ist eine der wichtigsten und schwierigsten Fragen der Klimawissenschaften. Ein Grund dafür ist die Unklarheit darüber, wie sich Mischungsprozesse in der untereren Troposphäre auf die Lebensdauer von Wolken auswirken. Stratocumuluswolken sind diesbezüglich einerseits besonders wichtig, da sie über eine große Albedo verfügen und sie sind anderseits besonders schwierig zu quantifizieren, da sie von meter- und zentimeter-skaligen Mischungsprozessen abhängen. Windscherung an der Wolkenoberkante und Sedimentation von Wolkentropfen können Mischungsprozesse in der untereren Troposphäre – d.h. Entrainment – stark beeinflussen, aber trotz alledem sind wichtige Aspekte beider Prozesse unverstanden. Obwohl zum Beispiel gut bekannt ist, dass Sedimentation von Wokentropfen Entrainment schwächt und Windscherung Entrainment verstärkt, ist die quantitative Bedeutung beider Prozesse unklar. Aus diesen Gründen untersucht diese Dissertation wie Sedimentations- und Windscherungsprozesse Entrainment in Stratocumuluswolken beeinflussen. Dazu werden direkte numerische Simulationen analysiert, welche die relevanten kleinskaligen Prozesse darstellen können.

Es ergeben sich drei Hauptergebnisse. Erstens wird gezeigt, dass die Schwächung von Entrainment durch Sedimentation unter subtropischen Bedingungen stark genug ist, um die Verstärkung von Entrainment durch Windscherung komplett auszugleichen. Hierbei schwächt Sedimentation die Entrainmentgeschwindigkeit um bis zu 40%, während Windscherung die Entrainmentgeschwindigkeit um bis zu 40% verstärkt. Dies zeigt, dass beide Prozesse gleich wichtig für Entrainment sind, was nahelegt, dass die Tropfengrößenverteilung wichtiger ist als bisher gedacht. Zweitens wird gezeigt, dass die Wahl der Referenzhöhe, mit Hilfe derer die Entrainmentgeschwindigkeit berechnet wird, wichtig ist für bestimmte Größen, aber unwichtig ist für andere. Vor allem die unterschiedlichen Beiträge zur Entrainmentgeschwindigkeit resultierend aus Mischungs-, Strahlungs-, und Verdunstungskühlung hängen stark von der Wahl der Referenzhöhe ab, obwohl die Entrainmentgeschwindigkeit als solche nur schwach von der Wahl der Referenzhöhe abhängt (zumindest in einem quasi-stationären Zustand). Der erste und zweite Punkt zusammen signalisieren, dass Parametrisierungen der Entrainmentgeschwindigkeit – zum Beispiel für Mixed-Layer-Modelle – die unterschiedlichen Beiträge zur Entrainmentgeschwindigkeit in der selben Referenzhöhe bestimmen müssen, und Sedimentations- und Windscherungsprozessen gleich viel Beachtung schenken müssen. Drittens wird gezeigt, dass zwei kritische Windgeschwindigkeiten existieren. Zu einem wird gezeigt, dass Windscherung Entrainment nur dann verstärkt, wenn die Windgeschwindigkeit einen kritischen Wert $(\Delta u)_{\text{krit}}$ überschreitet. Für $\Delta u < (\Delta u)_{\text{krit}}$ sind Windscherungsprozesse vernachlässigbar schwach. Zum anderen wird gezeigt, dass selbst wenn Windscherung Entrainment verstärkt, diese Verstärkung nicht unbedingt ausreicht, um den Wassergehalt der Wolke signifikant zu senken und somit die

Strahlungskühlung der Wolke zu verringern. Damit dies geschieht, muss die Windgeschwindigkeit einen zweiten kritischen Wert $(\Delta u)_{\text{stra}}$ überschreiten. Beide kritischen Windgeschwindigkeiten werden als Funktion von Wolken und Troposphäreneigenschaften hergeleitet und es wird gezeigt, dass $(\Delta u)_{\text{krit}} \simeq 1 - 4\,\mathrm{m\,s^{-1}}$ und $(\Delta u)_{\text{stra}} \simeq 3 - 10\,\mathrm{m\,s^{-1}}$ gilt. Zusammenfassend verdeutlicht diese Dissertation die Wichtigkeit von Sedimentations- und Windscherungsprozessen für Entrainment und zeigt dadurch die Wichtigkeit von kleinskaligen Prozessen für Stratocumuluswolken auf.

PUBLICATIONS RELATED TO THIS DISSERTATION

Bernhard Schulz and Juan Pedro Mellado. "Wind Shear Effects on Radiatively and Evaporatively Driven Stratocumulus Tops." In: Journal of the Atmospheric Sciences 75.9 (2018), pp. 3245–3263. doi: 10.1175/JAS-D-18-0027.1. See chapter 2.

Bernhard Schulz and Juan Pedro Mellado. "Competing Effects of Droplet Sedimentation and Wind Shear on Entrainment in Stratocumulus." In: Journal of Advances in Modeling Earth Systems 11 (2019). doi: 10 . 1029/2019MS001617. See chapter 3.

CONTENTS

LIST OF FIGURES

ACRONYMS

DNS   Direct numerical simulations

DSD   droplet size distribution

CRS   cloud resolving simulations

ECS   equilibrium climate sensitivity

EIL   entrainment interfacial layer

GCMs   general circulation models

IPCC   Intergovernmental Panel on Climate Change

LES   large eddy simulations

STBL   stratocumulus-topped boundary layer

TKE   turbulent kinetic energy

ON THE CHALLENGE OF UNDERSTANDING AND QUANTIFYING CLOUD PROCESSES

Your assumptions are your windows on the world. Scrub them off every once in a while, or the light won't come in.

— **Isaac Asimov**

How low clouds respond to anthropogenic warming is among the most important and most challenging questions in climate science. Why is that? Clouds organize in meso- and synoptic-scale cloud systems, which interact with the global atmospheric circulation. Yet, small-scale phenomena can substantially alter the lifetime and the temporal evolution of cloud systems. Emerging evidence is obtained that the limited understanding of small-scale lower-tropospheric mixing is among the most important obstacles hampering our ability of predicting and understanding the response of low clouds to anthropogenic warming [e.g. 11, 13, 105, 112, 147, 149]. In this regard, *stratocumulus* clouds are of particular importance due to their role for the Earth's radiation budget as argued in section 1.1. However, as discussed in section 1.2, understanding and quantifying the role of stratocumulus under a warming climate remains challenging, and one major reason therefor is the limited understanding of cloud-top *entrainment* as elucidated in section 1.3. Cloud-top wind shear and droplet sedimentation can substantially alter cloud-top entrainment, however, as argued in section 1.4, both processes are difficult to assess since they critically depend on meter- and submeter-scale mixing processes. Therefore, this dissertation investigates wind-shear and droplet-sedimentation effects on cloud-top entrainment in stratocumulus by means of direct numerical simulations, resolving the relevant meter- and submeter-scales.

Stratocumulus: low-level stratiform cloud system formed by an ensemble of single convective elements [141].

Entrainment: the turbulent mixing processes of environmental air into preexisting cloudy air.

1.1 THE IMPORTANCE OF LOW CLOUDS

Clouds cover on average 70% of the Earth's surface and are essential for determining the Earth's radiation budget. (You can directly jump to section 1.4 in case you are only interested in the results.) On average clouds reflect $\sim 46\,\mathrm{W\,m^{-2}}$ of the incoming solar radiation back to space. However, clouds also reradiate infrared radiation back to the surface from where it is emitted, thus reducing the amount of infrared radiation, which is lost to space by $\sim 28\,\mathrm{W\,m^{-2}}$. Combining the former 'albedo effect' and the latter 'blanketing effect' results in a net radiative cooling of $\sim 18\,\mathrm{W\,m^{-2}}$ [146]. The net radiative cooling associated with clouds is hence five times larger than the heating associated with a doubling of CO_2, which is estimated to be $\sim 3.7\,\mathrm{W\,m^{-2}}$ [e.g. 60]. This illustrates that even subtle changes in cloud properties that might accompany anthropogenic warming can significantly alter that warming — that are *cloud feedbacks* [146]. An alternative

Cloud feedbacks: quantify how an increase in surface air temperature changes cloud properties and how these changes feedback on the surface air temperature.

way to illustrate the challenge of understanding cloud feedbacks is by noting that clouds contain very little water, that is all water (cloud droplets and ice) condensed in clouds would only create a 0.1 mm thin liquid layer when spread uniformly on the Earth's surface. In contrast, there is approximately 250 times more water vapor in the atmosphere and condensing all the water vapor would create a 2.5 cm thick liquid layer. Predicting how clouds respond to anthropogenic warming, therefore, requires the ability to predict how this tiny fraction of water vapor, which is condensed into liquid water to form clouds, changes under a warming climate [108]. All this illustrates the importance of clouds on the one hand and the challenge of quantifying cloud feedbacks on the other hand.

Three main cloud feedbacks are distinguished [145]. First, the cloud amount feedback describes changes in the cloud coverage induced by anthropogenic warming. The sign of this feedback is determined by the competing impacts of low clouds and high clouds. While low clouds cool the Earth due to a dominating 'albedo effect', high clouds do the opposite and warm the Earth due to a dominating 'blanketing effect'. An increase in low cloud coverage would, therefore, cool the Earth and slow down anthropogenic warming (that is a negative feedback) while an increase in high cloud coverage would warm the Earth (that is a positive feedback). High clouds are reported to dominate this feedback, which renders the net cloud amount feedback positive. Second, the cloud altitude feedback describes how cloud-radiative properties change with changing cloud-top heights. Under a warming climate, in particular high clouds are expected to ascend, which cools the cloud top and thus makes high clouds less efficient in emitting infrared radiation to space. Therefore, the sign of the cloud altitude feedback is reported to be positive. Third, the cloud opacity feedback describes how anthropogenically induced changes in the cloud water content and phase (ice vs. liquid) as well as changes in the size of cloud droplets and crystals translate into opacity changes. The sign of this feedback is reported to be negative since changes in the cloud opacity are such that the 'albedo effect' prevails over the 'blanketing effect'. Whether the summation of all cloud feedbacks results in a positive or negative value remains uncertain. The net cloud feedback is reported to be in the range of $-0.2\,\mathrm{W\,m^{-2}\,^{\circ}C^{-1}}$ to $2\,\mathrm{W\,m^{-2}\,^{\circ}C^{-1}}$ according to the fifth IPCC report from 2013 [126] and in the range of $-0.2\,\mathrm{W\,m^{-2}\,^{\circ}C^{-1}}$ to $0.8\,\mathrm{W\,m^{-2}\,^{\circ}C^{-1}}$ according to a more recent study from Zelinka et al. [146]. For reasons to be discussed later, the main source for this enormous spread in the net cloud feedback are large uncertainties in low-cloud feedbacks [e.g. 10, 15, 26, 81, 112, 146], and the fifth IPCC report [126] formulates this statement as follows: "Uncertainty in the sign and magnitude of the cloud feedback is due primarily to continuing uncertainty in the impact of warming on low clouds".

Reducing the uncertainty in cloud feedback is important for determining more accurately the equilibrium climate sensitivity (ECS), where the ECS is defined as the global mean surface temperature change that arises from a doubling of the atmospheric CO_2 concentration relative to its pre-industrial concentration after the climate system has reached a new equilibrium state (which takes thousands

Figure 1.1: Cloudscape picture over the southern Pacific Ocean, with stratocumulus clouds covering the southwestern region (NASA Photo ID: ISS040-E-006780). Semi-permanent marine stratocumulus sheets cover 40% to 60% of the Earth's surface in the subtropical eastern oceans [141].

of years). Since many impacts following anthropogenic warming scale to leading order with the global mean surface temperature, ECS has become one of the most important numbers quantifying how severe climate change will be [e.g. 60, 108]. Charney et al. [25] estimated in 1979 that the range of the ECS is 1.5°C to 4.5°C. It is remarkable and also unsettling that this range has not changed ever since. All observational and modeling efforts in the past decades have not succeeded in significantly reducing this large uncertainty of the ECS, and the fifth IPCC report from 2013 [126] still reports the same range of 1.5°C to 4.5°C for the ECS. This large uncertainty in the ECS demonstrates how challenging it is to predict how our climate system will respond to global warming. However, even though the magnitude of the ECS remains highly uncertain, enormous progress has been made in understanding the factors controlling the ECS and today, emerging evidence is obtained that—as suggested decades ago by Arakawa [4] and Charney et al. [25]—a substantial part of this large spread in the ECS originates from low-cloud feedbacks [e.g. 11, 81, 82, 105, 112, 125, 126, 147, 149].

The underlying reason for many of the obstacles associated with quantifying cloud feedbacks is the large scale separation in clouds. Clouds are composed of water and ice droplets that settle on aerosols, ranging from microns to millimeters. They are subject to turbulent and convective motions, with motions of scales ranging from millimeters to kilometers. They are organized on the meso- and synoptic-scale and interact with the global atmospheric circulation, with motions on scales ranging from tenth of kilometers to thousands of kilometers [cf. 104]. More specifically, two 'classes' of problems need to be addressed in order to

Troposphere: the lowest $6 - 18\,km$ of the Earth's atmosphere where temperature usually decreases with height and where weather conditions manifest themselves [127] .

reduce the large uncertainty in the ECS. On larger scales, we need to advance our understanding of how clouds interact with the global atmospheric circulation. Broadly speaking, this for example concerns the question of how convective aggregation and organization impact climate, as well as the question of how clouds couple to stormtracks [11, 13]. On smaller scales, which are the focus of this dissertation, we need to advance our understanding of how small-scale lower-*tropospheric* mixing affects the evolution of cloud systems. For all these reasons Bony et al. [13] conclude that: "Progress toward understanding the interplay between clouds, circulation and climate sensitivity is a primary metric of our ability to anticipate future climate."

Addressing this matter poses a great observational challenge, as briefly outlined in this paragraph, and a great numerical challenge, as discussed in the remainder of this thesis. On the micrometer scale, it for example remains unclear at which size the transition from growth by diffusion to that by coalescence takes place and for that reason the onset of precipitation in warm clouds remains puzzling [45, 47, and references therein]. This poses an observational challenge since it is difficult to measure droplets in the just mentioned transition size range, i.e., droplet with a diameter of $40\,\mu m$ to $80\,\mu m$. The newly developed Holographic Detector for Clouds (HOLODEC) is designed to address these and similar challenges [e.g. 8, 40, 41], and a recent paper by Glienke et al. [45] for example utilizes the HOLODEC to question the existence of the condensation-to-collision growth gap. On the meter and submeter scale, experimentally quantifying lower-tropospheric mixing rates remains a difficult task. This is in particular the case for stratocumulus clouds, where strong vertical gradients in humidity and temperature at the cloud-top require in-situ measurements with a high spatial and temporal resolution [e.g. 54, 56, 122, 123, 141]. On the global scale, investigating the relationship between clouds, aerosols and radiation remains challenging. To that aim the EarthCARE satellite will be launched in Autumn 2019. Broadly speaking, the objective of EarthCARE is to provide global profiles of clouds (i.e. atmospheric liquid water and ice) and aerosols combined with measurements of solar radiation reflected and thermal radiation emitted from the Earth's surface [50]. In addition, as elucidated in the previous paragraphs, it is a particularly important task to better understand the interplay between clouds and circulation. However, addressing this issue is also particularly challenging as it requires simultaneous measurements at various scales. The EUREC⁴A campaign (January to February 2020) will take a first step into this direction by quantifying for the first time how the amount of shallow cumulus clouds varies with changing large-scale conditions [12]. In summary, all these projects illustrate that investigating clouds remains a serious observational challenge. Having said this, we will focus on numerical models in the rest of this dissertation.

1.2   A HIERARCHY OF MODELS FOR STUDYING CLOUDS

Approximately 50% of the variance in the ECS is associated with the simulated strength of turbulent mixing between the lower and middle troposphere [112].

Better representing small-scale turbulent mixing processes in numerical models is therefore key for reducing the uncertainties associated with low-clouds feedbacks and the ECS [13]. The forthcoming discussion is supposed to illustrate the challenge of representing small-scale turbulent mixing processes in numerical models.

Representing clouds in general circulation models (GCMs) has been and remains to be a major challenge in climate science as already noted by Arakawa [4] and Charney et al. [25] in the 1980s. GCMs have a coarse grid resolution of approximately $20 - 200$ km, which allows running them for climatologically relevant time scales. For that reason, GCMs are regularly used for studying low-cloud feedbacks and for investigating the ECS. However, due to their relatively coarse resolution, they are unable to represent cloud processes in the necessary detail and therefore those sub-grid processes need to be parametrized, i.e., their effect on the model dynamics must be prescribed as a function of the resolved processes. However, there is a seemingly endless list of cloud processes that need to be parametrized, for example including microphysical processes, radiative effects, mesoscale organization, deep convection, shallow convection, and boundary-layer clouds. In particular, the latter two are challenging as they sensitively depend on the way small-scale turbulent-mixing processes are represented [e.g. 96, 104, 131]. Due to the variety and complexity of all these processes, Randall et al. [104] conclude that the cloud parametrizations problem is overwhelmingly complicated and very, very hard to "solve". This explains why the coupling between clouds, convection, and the large-scale circulation in general and small-scale lower-tropospheric mixing processes in particular is poorly represented in actual GCMs [e.g. 11, 29, 52, 95, and studies cited above]. This drawback of GCMs explains a substantial part of the large spread, which is observed in low-cloud feedbacks and ECS (see section 1.1).

Many of the problems associated with convective parametrizations in GCMs are alleviated in cloud resolving simulations (CRS), which are also referred to as storm-resolving or convective-permitting simulations. CRS are broadly speaking regional or global 'weather' models with a horizontal grid spacing of $1 - 5$ km. As indicated, the advantage of such high-resolution simulations is that significantly less processes need to be parametrized. For example, CRS are able to explicitly represent deep convection [e.g. 57, 58], mesoscale convective systems [6, 11, 16, 27, 52, 91, 140], and squall-lines [90, 130], where the latter motivates the term storm-resolving simulations. For all these reasons, CRS are able to qualitatively reproduce many features of the tropics observed during measurement campaigns, like the forms of convective organization and the forms of storm tracks [59]. This indicates that CRS can help to explain model biases observed at coarser resolutions, which suggests that GCMs can be evaluated against CRS [59]. This opens a new avenue for developing convection parametrizations. All this demonstrates that CRS provide an amazing variety of details and allow for utterly new insights into our climate system. However, due to their high resolution, they need to compromise on the simulation length and (or) the domain size. In particular, in the foreseeable future it is impractical to run global scale CRS on climate time

Atmospheric boundary layer: the lowest part of the troposphere which is directly affected by the surface and the diurnal cycle.

scales. Moreover, it is emphasized that even CRS need to parametrize shallow convection and *boundary-layer* turbulence, which results from the fact that the vertical resolution is not substantially increased in CRS compared to GCMs, i.e., the vertical grid spacing is on the order of 250 m in both models. To account for subgrid processes, CRS typically apply a shallow-convection scheme[1], a Reynolds averaged Navier-Stokes (RANS) turbulence model, or simply a Smagorinsky like turbulence model. In summary, all this indicates that CRS are a highly promising tool for a wide variety of questions, but nonetheless shallow convection and boundary-layer clouds are difficult to assess by means of cloud resolving simulations.

In large eddy simulations (LES) the vertical resolution is substantially increased compared to cloud resolving simulations (CRS), and therefore, LES allow for a more complete representation of shallow convection and boundary-layer clouds. Typically the vertical as well as the horizontal grid spacing is on the order of $5 - 200$ m. This high resolution limits the computationally affordable domain size, but in return renders the parametrizations of shallow convection unnecessary. Subgrid processes in LES are, therefore, typically only modeled by means of a Smagorinsky like turbulence model. As a consequence of this high resolution LES can accurately simulate small- to mesoscale variability in turbulence, clouds and precipitation, as for example demonstrated by Heinze et al. [49] who performed a LES study over the domain of Germany. This indicates that LES can be used for testing and developing cloud parametrizations for GCMs and CRS. LES studies with a vertical grid spacing of $5 - 40$ m are regularly used and have been proven useful for investigating various aspects of boundary-layer clouds [e.g. 31, 33, 38, 62, 79, 88, 107, 124, 144]. These studies include the important regime of stratocumulus clouds, where LES are for example employed to study the stratocumulus to cumulus transition. However, using LES for making quantitative predictions of stratocumulus regimes remains difficult since the dynamics of stratocumulus depends critically on cloud-top entrainment and hence on meter- and submeter-scale mixing processes (cf. section 1.3), which are inadequately represented in current LES subgrid-models [87]. In particular, *entrainment velocities* are typically overestimated by LES subgrid-models and therefore they need to be tuned to observational data [e.g. 87, 97, 98, 121, 124]; where the entrainment velocity $w_e = dz_i/dt$ is defined as time rate of change of some arbitrary reference height z_i marking the cloud-top [65]. This need for tuning is the main drawback of LES, since it strongly challenges our ability of using the same LES setup under different environmental conditions, and it is therefore unclear to which extend LES can properly sample the sensitivity of stratocumulus to changes in environmental conditions. Anyhow, it is often assumed that LES can do so and this assumption is referred to as LES hypothesis, namely: "LES accurately quantifies the sensitivity of stratocumulus to changes in environmental conditions, even though cloud-top entrainment is not properly represented in LES" [87]. An additional obstacle in

Entrainment velocity w_e: time rate of change of the cloud-top height, z_i, driven by diabatic processes.

---

1 Note that at such a high resolution parametrization assumptions from coarser resolutions break down, e.g., the assumption that each grid box contains a representative ensemble of cumulus clouds. Therefore, CRS need new shallow-convection schemes [32].

this regard is the need to obtain accurate observational reference data, which can be used for tuning the LES. Obtaining such reference data is, however, challenging since the cloud-top is typically characterized by strong vertical gradients in temperature and horizontal winds, which implies the need to sample the property of interest—like liquid water, humidity, passive tracers, and temperature—with a high temporal resolution [e.g. 44, 56, 122]. In sum, all this clearly demonstrates the relevance of LES but also indicates its limitations, especially for studying cloud-top entrainment and thus for investigating the dynamics of stratocumulus.

Direct numerical simulations (DNS) provide a research tool, which is in particular well suited for studying cloud-top entrainment, as the relevant meter- and submeter-scale mixing processes are explicitly resolved (cf. section 1.3). In DNS, the governing equations are solved without applying a subgrid model and hence DNS are free of all uncertainties associated with subgrid models, which contrasts LES where this is not the case. However, this implies that DNS need to explicitly resolve all length scales down to the *Kolmogorov scale*, which renders DNS computationally demanding. This limits the application of DNS to relatively short simulation times, small domains sizes, and simplified configurations. In addition, for DNS to be computationally affordable, the viscosity of air is typically enhanced by a factor of 1000 compared to its atmospheric value, which implies a typical Kolmogorov length and thus a grid spacing on the order of $10 - 100$ cm. (Note that in LES the effective viscosity is enhanced by a factor of 1000-10000 compared to its atmospheric value.) Since the viscosity is artificially enhanced, it is necessary to study the sensitivity of the DNS results to changes in the viscosity, where viscous effects are characterized by a Reynolds number. Fortunately, there is experimental evidence that some key boundary layer and cloud properties become relatively independent of the Reynolds number once the Reynolds number exceeds a critical value. This observation is referred to as Reynolds number similarity [36, 87]. Nowadays, as a consquence of an increase in computationally power, DNS reach high enough Reynolds numbers for this to be the case. In other words, in current DNS high enough Reynolds number are reached for properties to only depend weakly on the Reynolds number. This weak dependence on the Reynolds number supports the use of DNS to study some aspects of the stratocumulus-topped boundary layer (STBL). In addition, note that in DNS (like in GCM, CRS, and LES) radiative processes and microphysical processes are parametrized, as for example DNS often prescribes the effect of varying the cloud droplet number concentration. In sum, all this indicates that DNS are a valuable tool for studying cloud-top entrainment, which motivates the use of DNS in this dissertation.

In general, the preceding discussion shows that a hierarchy of models is needed to study the various aspects and scales of clouds, and combining these different approaches is key for advancing our understanding of the Earth's climate. So far, we have argued that quantifying low-cloud feedbacks remains a major challenge in climate science, and we have argued that one important reason for that is the poor representation of small-scale turbulent mixing processes in numerical

Kolmogorov scale: the smallest scale of a turbulent flow where turbulent kinetic energy is dissipated into heat.

models. However, we have not yet discussed why small-scale turbulent mixing processes are important for the dynamics of stratocumulus. This is done next.

1.3   THE IMPORTANCE OF SMALL-SCALE MIXING PROCESSES

Stratocumulus alone contribute 25% to the globally averaged low-cloud cover [141], which renders stratocumulus efficient in cooling the Earth's atmosphere (see section 1.3). Therefore, stratocumulus clouds are sometimes loosely referred to as "climate refrigerators" [19]. Stratocumulus clouds are most evident over the subtropical eastern oceans where the annual mean stratocumulus coverage exceeds 40% and can be as high as 60% (see Fig. 1.1). In these regions the downward directed branches of the Hadley/Walker circulation create a setting in which cloudy air is capped by a layer of warm *free-tropospheric* air (see Fig. 1.2), and as argued below, these are favorable conditions for stratocumulus [e.g. 118, 141]. However, understanding the dynamics of stratocumulus remains difficult and one major reason for that is the limited understanding of cloud-top entrainment as indicated by a number of numerical experiments [e.g. 18, 35, 53, 84, 89, 124, 129] and observational studies [e.g. 24, 37, 39, 54, 56, 76, 123, 136, 141]. One key reason, why understanding and quantifying cloud-top entrainment remains a challenge, is that turbulence in stratocumulus is generated to a large extent at the cloud-top by radiative and evaporative cooling, which distinguishes stratocumulus from other types of boundary layer clouds where this is not the case [17, 141]. As elucidated below, this implies that in stratocumulus, large-scale convective motions are generated in the cloud-top region by meter- and submeter-scale processes. Stratocumulus clouds, therefore, break with a paradigm often found in climate science, namely, that energy is introduced into the system on larger scales from where it is transferred down to the small dissipative scales (the Kolomogorov scale). However, in stratocumulus, small-scale processes can force large-scale motions, and this is the underlying reason for many of the obstacles associated with the numerical modeling of stratocumulus.

Radiative and evaporative cooling are important sources of turbulence in stratocumulus. Stratocumulus contain sufficient liquid water for being largely opaque to longwave radiation. Well within the cloud, upward and downward directed long wave radiation fluxes compensate each other and therefore the net radiative cooling within the cloud is zero. However, in the cloud-top region, the downward directed flux decays rapidly and hence the outgoing longwave radiative flux can efficiently cool the cloud-top region. For optically thick clouds this cooling is concentrated in a shallow layer in the cloud-top region with a thickness of approximately $10 - 20\,\mathrm{m}$, which already indicates the importance of small-scale processes. Longwave radiation typically cools the cloud-top at a rate of $5 - 10\,\mathrm{K\,h^{-1}}$ [84], thereby generating convective instabilities and promoting cloud-top entrainment. Due to the importance of radiative cooling for cloud-top entrainment radiative cooling is a key processes for stratocumulus [e.g. 9, 84, 101, 141]. Evaporative cooling rates can be comparable to radiative cooling rates as already suggested
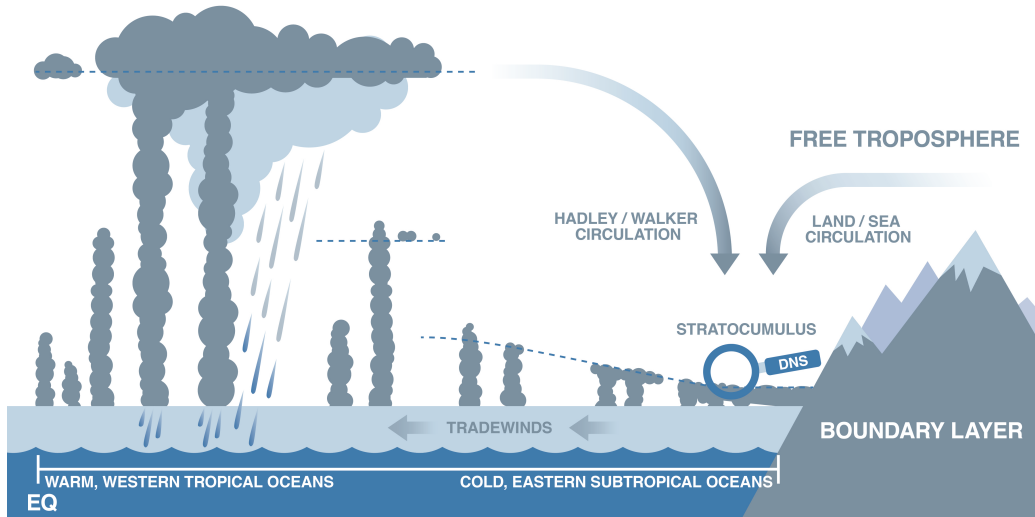
Free troposphere: the part of the troposphere located directly above the atmospheric boundary layer [127].

Figure 1.2: Stratocumulus clouds typically form over the upwelling subtropical oceans where the downward branches of the Hadely/Walker circulation create a strong thermal contrast between the underlying cloudy air and overlying free-tropospheric air. A zoom into the stratocumulus-topped boundary layer is presented in Fig. 1.3. Figure adapted from [118].

by the observation that evaporating all water in a fluid particle with $0.5\,\mathrm{g\,kg^{-1}}$ of liquid water cools the fluid by approximately $1\,\mathrm{K}$, which is comparable with cooling the cloud-top for approximately 10 min by longwave radiation [84]. Evaporative cooling results from mixing cloudy and environmental air on a molecular level, which implies that evaporative cooling peaks near the cloud boundary. In addition, this implies that evaporative cooling substantially depends on the rate at which environmental air is mixed—entrained—into the cloud. Depending on the environmental conditions, the cloud-dry-air mixtures can become negatively buoyant with respect to its environment and this phenomena is referred to as buoyancy reversal [e.g. 85, 94, 114, 117, 142]. Under buoyancy reversal conditions evaporative cooling creates convective instabilities, which enhances in-cloud turbulence, which in turn enhances the mixing of cloudy and environmental air (that is entrainment). However, enhanced entrainment strengthens evaporative cooling, which reinforces the convective instabilities. This self-enhancing feedback was conjectured to lead to a rapid desiccation of the cloud, thus triggering a break-up of the cloud [33, 65, 102]. However, subsequent laboratory experiments [113, 114], observational studies [e.g. 3, 94, 123], and numerical experiments [e.g. 63, 64, 68, 83, 114, 142, 143] have not observed such an instability, indicating that this feedback loop is relatively weak. In agreement with that, evaporative cooling rates are found to be weak, if evaporative cooling acts alone, i.e., if entrainment is not enhanced by other processes like radiative cooling or wind shear [71, 72, 83]. A related aspect is that the strength of radiative and evaporative cooling substantially depends on the environmental conditions, e.g., smaller jumps in total-water specific humidity are expected to increase the importance of radiative cooling compared to evaporative cooling [73]. All this indicates that the coupling
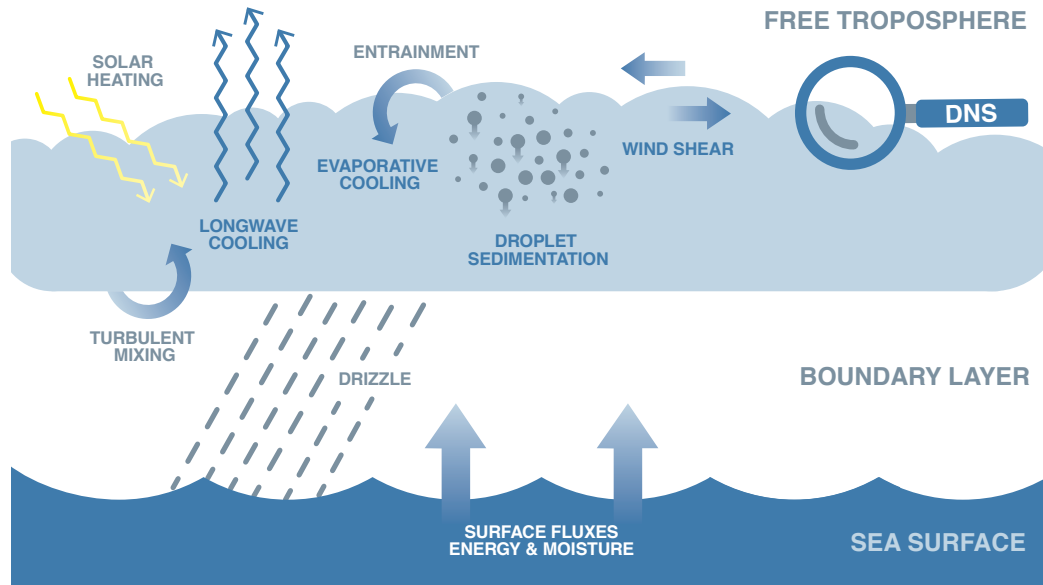
Figure 1.3: Schematic showing the most important processes occurring in a stratocumulus-topped boundary layer. Figure adapted from [141].

between the different cloud-top processes is crucial for the dynamics of stratocumulus. However, understanding this coupling is challenging since the involved processes depend critically on meter- and submeter-scales. It is this importance of small-scales mixing processes, which renders stratocumulus so difficult to understand and to quantify.

Even though radiative and evaporative cooling are important sources of turbulence in stratocumulus, a number of other processes can crucially alter the dynamics of a stratocumulus-topped boundary layer (STBL). As illustrated in Fig. 1.3, these processes for example include solar heating of the cloud-top, turbulent mixing at the cloud base, surface moisture and heat fluxes, drizzle, wind shear, and *microphysical* processes, like droplet sedimentation and finite-time evaporation. Further note that changes in the droplet size force the albedo and precipitation-efficiency to change. For a thorough discussion of all these different processes we refer the reader to review papers in references [69, 84, 118, 141]. Here, we solely focus on two of these processes, namely on cloud-top wind shear and on droplet sedimentation.

Cloud microphysics: could properties and processes resulting from the finite size of cloud droplets.

Vertical shear of the horizontal wind velocity can enhance cloud-top entrainment. Wind shear is typically imposed by synoptic-scale pressure gradients and is characterized by the cloud-top velocity jump Δu and the shear layer thickness h_S, which marks the thickness over which Δu varies. The cloud-top velocity jump is defined as $\Delta u = ||\mathbf{u}^d - \mathbf{u}^c||$, where $\mathbf{u}^d$ and $\mathbf{u}^c$ represent the mean velocity in the dry-free troposphere and in the cloud respectively[2], and typically values are

---

2 And in the performed DNS the reference frame is assumed to move with the mean velocity $(\mathbf{u}^d + \mathbf{u}^c)/2$ and is supposed to be aligned with $\mathbf{u}^d - \mathbf{u}^c$, see section 1.4.

reported to be on the order of $\Delta u \simeq 3 - 5\,\mathrm{m\,s}^{-1}$, even though extreme values of up to $\Delta u \simeq 10\,\mathrm{m\,s}^{-1}$ have been observed [20, 39, 56, 76, 93, 106]. If the shear layer is thin enough and if the cloud-top velocity jump is strong enough, wind shear enhances cloud-top entrainment by generating shear instabilities [Kelvin-Helmholtz instabilities and Holmboe instabilities; e.g. 23, 115]. That means that wind shear causes an overturning of the stably stratified fluid, which enhances the mixing of free-tropospheric and cloudy air and which causes a thickening of the shear layer. However, the kinetic energy associated with wind shear, $(\Delta u)^2$, can uplift air parcels only a certain distance against the stratification until all its kinetic energy is converted into potential energy. Once the shear layer reaches this critical thickness, wind shear is unable to overturn the stably stratified fluid anymore and shear generated turbulence decays [21, 100, 116]. For a strong enough shear, this critical thickness is comparable to the *entrainment interfacial layer* thickness h_{EIL}, where the entrainment interfacial layer (EIL) defines a stably stratified transition layer between the cloud and the free troposphere. The EIL contains most of the changes in temperature, humidity and cloud-top wind shear occurring between these two layers and is typically rather shallow with a typical thickness varying between a few meters and several tens of meters [e.g. 56, 62, 76, 86, 139]. All in all, the preceding discussion shows that wind shear alone is unable to permanently enhance mixing in the cloud-top of stratocumulus. However, in-cloud turbulent convection generated by radiative and evaporative cooling penetrates into the EIL, which locally thins the EIL and thus enables cloud-top wind shear to permanently enhance mixing of free-tropospheric and cloudy air and by that cloud-top entrainment [84]. Furthermore, it is important to note that mixing in a stratified shear layer is characterized by the Ozmidov scale, which is the length scale above which turbulence is affected by stable stratification and which is the order of just a few meters in the EIL [87, 109]. The presence of cloud-top wind shear thus further emphasizes the importance of meter- and submeter-scale mixing processes for cloud-top entrainment [e.g. 54, 56, 86, 109]. As further elucidated in section 1.4, it is this dependence on small-scale mixing processes, which makes wind-shear effects so difficult to quantify.

Entrainment interfacial layer (EIL): transition layer between cloudy and free-tropospheric air.

In stratocumulus, *droplet-sedimentation* effects are not only important for rain formation, but also for cloud-top entrainment and thus for non-drizzling stratocumulus, which contribute 60%-80% to the marine stratocumulus cloud cover [141] and which have typical droplet diameters in the range of $10 - 30\,\mu$m [2, 45, 47, 48, 56, 77, 135]. Changes in the droplet sedimentation strength can for example originate from an increase in the aerosol concentration. Increasing the aerosol concentration increases the droplet number concentration, which for a fixed amount of cloud liquid water reduces the droplet size and enhances the cloud reflectivity—this known as Twomey effect [133]. However, smaller droplets can also be uplifted more easily by in-cloud turbulent convection, which weakens droplet sedimentation and enhances cloud-top entrainment. More precisely, weakening droplet sedimentation enhances cloud-top entrainment by enhancing evaporative cooling and by weakening the upward directed sedimentation buoyancy flux that directly opposes entrainment [1, 2, 14, 51, 74]. In addition,

Droplet sedimentation: the gravitational settling of cloud droplets suspended in the cloud.

since the entrained free-tropospheric air is typically relatively warm and dry, the enhanced entrainment decreases the amount of liquid water within the cloud, thins the cloud, and decreases the albedo. This decrease in cloud reflectivity partly compensates the Twomey effect, i.e., the increase in cloud reflectivity associated with the initial increase in the aerosol concentration [1, 2, 14, 51]. However, while it is well known that the Twomey effect is climatologically significant, it remains unclear how important the discussed sedimentation-entrainment effect is for determining the albedo. As argued in section 1.4, the main reason therefor is that the importance of droplet sedimentation for cloud-top entrainment remains uncertain.

In summary, the preceding discussion indicates that wind-shear and droplet-sedimentation effects are important for the dynamics of stratocumulus on the one hand, but difficult to quantify on the other hand. This motivates the main research question of this dissertation, namely:

How do cloud-top wind shear and droplet sedimentation alter entrainment of a radiatively and evaporatively driven stratocumulus top?

1.4   WIND-SHEAR AND DROPLET-SEDIMENTATION EFFECTS

The first part of this section specifies the general research question posed in the previous section, while the second part addresses these questions by summarizing and discussing the results of the two papers, which are the basis of this dissertation [see 109, 110].

Specific research questions

Cloud-top wind shear can substantially enhance entrainment, can substantially thicken the EIL, and can substantially change the budget of turbulent kinetic energy (TKE), as indicated in section 1.3 and as shown by a number of observational studies [20, 24, 37, 39, 54, 56, 76, 106] and numerical studies [62, 86, 137, 139]. In particular, LES studies by Wang et al. [137] and Wang et al. [139] report a shear enhancement of the entrainment velocity w_e by $50\% - 200\%$ for cloud-top velocity jumps on the order of $\Delta u \simeq 5 - 10\,\mathrm{m\,s^{-1}}$. This demonstrates that shear effects on cloud-top entrainment can be strong. In addition, note that shear-enhanced entrainment is accompanied by a substantial increase in the EIL thickness and a substantial change in the TKE budget (see studies cited above). However, despite the importance of shear, it remains unclear at which minimal *First research* shear strength significant changes in all these quantities occur. As a first research *question* question we therefore ask: At which minimal shear strength does shear start to enhance entrainment?

Even though it is well known that strengthening droplet sedimentation weakens entrainment, quantifying droplet-sedimentation effects remains a challenge (see section 1.3). Previous LES studies indicate that the sedimentation weakening

of the entrainment velocity is rather weak, namely, sedimentation weakens the entrainment velocity by $\sim 5\% - 20\%$ compared to the case without sedimentation [1, 2, 14, 51], where the relatively large spread is partly due to different thermodynamic conditions. However, a recent DNS study by Lozar and Mellado [74] reports that the sedimentation weakening of the entrainment velocity is 2-3 times larger, which corresponds to a reduction of $\sim 40\%$. All this shows that the magnitude of sedimentation weakening of the entrainment velocity remains highly uncertain. Besides, it suggests that excessive mixing by turbulence models and numerical artifacts may have partially masked sedimentation effects on entrainment in former LES studies. It is noteworthy that, this strong sedimentation induced reduction of $\sim 40\%$ is comparable with the shear induced enhancement of the entrainment velocity observed in Schulz and Mellado [109] for the very same thermodynamic conditions. This suggests that wind shear and droplet sedimentation effect can be equally important for determining cloud-top entrainment, which calls into question the assumption that shear effects prevail over sedimentation effects. In sum, the last two paragraphs pose our second research question, namely, to what extent can wind-shear and droplet-sedimentation effects on cloud-top entrainment compensate each other?

Second research question

   The entrainment velocity w_e (defined in section 1.2) provides a useful framework for studying wind-shear and droplet-sedimentation effects on entrainment. One reason is that the entrainment velocity can be analytically decomposed into separate contributions, resulting from mixing, evaporative cooling, and radiative cooling. The entrainment velocity, therefore, allows for a thorough and mathematical stringent study of these different contributions. Another reason is that entrainment velocity parameterizations are needed in mixed-layer models — that are bulk models that model the mixed-layer of the atmospheric boundary layer in an integral sense. Mixed-layer models form the theoretical base for much of our understanding of STBLs and are in particular important for studying the response of STBLs to changes in meso- and synoptic-scale conditions [e.g. 17, 28, 65, 99, 103, 119, 132, 148]. Besides, mixed-layer models are a promising tool for representing boundary layer processes in GCMs [5, 34, 80, 128]. However, today's parametrizations of the entrainment velocity are highly uncertain [39, 67, 117, 134], which limits our ability of using mixed-layer models for making quantitative predictions of the STBL evolution as elucidated in section 1.5. Deriving more accurate entrainment velocity parametrizations is, however, a highly challenging task since the different processes involved in cloud-top entrainment are nonlinear, strongly coupled, and crucially dependent on small-scale processes [84]. This problem is particularly difficult for shear and sedimentation effects, as indicated in section 1.3 and as discussed in what follows. In addition, the separate contributions to the entrainment velocity, resulting from mixing, evaporative cooling, and radiative cooling, vary rapidly in the vertical direction. This indicates that the choice of the reference height z_i, where $w_e = dz_i/dt$ is calculated, might be important, even though typical choices of z_i differ only by a few meters. In agreement with that, previous studies indicate that entrainment velocity parametrizations critically depend on the definition of z_i [39, 43, 123]. This strong dependence on

the choice of the reference height z_i poses an additional challenge for understanding and quantifying wind-shear and droplet-sedimentation effects on cloud-top entrainment, and accordingly on entrainment velocity parameterizations.

A related point is that the analysis of cloud-top entrainment typically assumes a *quasi-steady state*, that is a state in which in-cloud and free tropospheric conditions vary slowly compared to cloud-top processes. This implies that in a quasi-steady state the atmospheric boundary layer deepens slowly compared to the large-eddy turnover time (as further elucidated in the last paragraph of this section). Nonetheless, unsteady states, where this is not the case, are regularly observed, e.g., during the transition from stratocumulus to cumulus. However, to the best of our knowledge, an explicit quantification of unsteady effects is missing. All this motivates a third set of research questions, namely: How do shear and sedimentation alter the separate contributions to the entrainment velocity, resulting from mixing, evaporative cooling, and radiative cooling? What is the effect of varying the reference height z_i? How can we quantify unsteady effects on the entrainment velocity?

Results

In order to answer these questions, direct numerical simulations of a stratocumulus cloud-top have been performed. In the performed simulations turbulence is generated by shear and convective instabilities, where the latter originate from radiative and evaporative cooling. Solar heating, drizzle, turbulent mixing at the cloud base, and surface fluxes are neglected (see Fig. 1.3). This simplified simulation set-up enables us to sufficiently decrease the grid spacing to explicitly resolve the relevant meter- and submeter-scale mixing processes, which are otherwise difficult to assess. The validity of these simplifications is supported by the finding that the obtained entrainment velocities as well as the strength of in-cloud turbulence is consistent with measurement campaigns, as elucidated further in the last paragraph of this section. Our simulation set-up mimics subtropical conditions, which are characterized by relatively large jumps in total-water specific humidity (i.e. $\Delta q_t = 7.5\,\mathrm{g\,kg^{-1}}$) and temperature (i.e. $\Delta T = 8.5\,\mathrm{K}$) at the stratocumulus top.

Moreover, a nondimensional formulation proves convenient to reduce the degrees of freedom in the parameter space that defines the problem, to generalize our results to different atmospheric conditions and to gain some a priori insight into the importance of the involved processes. To investigate wind-shear and droplet-sedimentation effects, we have systematically varied the shear number $Sh_0 = \Delta u / U_0$ and the sedimentation number $Sv_0 = u_{sed}/U_0$, where Δu is the cloud-top velocity jump (see section 1.3), u_{sed} a bulk sedimentation velocity, and U_0 a reference velocity scale based on radiative properties [cf. 110]. This illustrates that a single sedimentation number Sv_0 characterizes various combinations of u_{sed} and U_0, which is one of the advantages of using nondimensional numbers. The investigated shear numbers range from $Sh_0 = 0$ to $Sh_0 = 10$ and correspond to cloud-top velocity jumps ranging from $\Delta u \simeq 0\,\mathrm{m\,s^{-1}}$ to $\Delta u \simeq 3\,\mathrm{m\,s^{-1}}$, where $\Delta u \simeq 3\,\mathrm{m\,s^{-1}}$ represents typical atmospheric conditions as discussed in section 1.3. For each shear number, we have varied the sedimentation number in the range

from $Sv_0 = 0$ to $Sv_0 = 0.1$, which resembles the range of sedimentation fluxes studied in previous LES [1, 2, 14]. These sedimentation numbers translate into bulk sedimentation velocities ranging from $u_{\text{sed}} \simeq 0\,\text{mm}\,\text{s}^{-1}$ to $u_{\text{sed}} \simeq 30\,\text{mm}\,\text{s}^{-1}$, where the employed bulk microphysics scheme allows to change u_{sed} either by changing the mean or the standard deviation of the droplet size distribution (which is assumed to be log-normal). We finally note that the properties of interest typically vary by less than 20% when changing the Reynolds number by a factor of up to three. In particular, our simulations accurately represent changes of the entrainment velocity w_{e} with sedimentation and shear, i.e., the gradients $\partial w_{\text{e}}/\partial u_{\text{sed}}$ and $\partial w_{\text{e}}/\partial \Delta u$. This weak dependence on the Reynolds number supports the use of the performed DNS to study some aspects of the STBL (see section 1.2). In what follows, we summarize and discuss the most important results presented in Schulz and Mellado [109] and Schulz and Mellado [110].

The answer to the first question, concerning the minimal wind shear that enhances cloud-top entrainment, is based on the observation that the dynamics of the EIL is subject to two different forcings. On one hand, in-cloud turbulent convection—characterized by the in-cloud convective velocity scale w_*—penetrates into the stably stratified EIL and thereby transports TKE into the EIL. On the other hand, a sufficiently strong cloud-top wind shear—characterized by the cloud-top velocity jump Δu—creates Kelvin-Helmholtz instabilities, thus enhancing the mixing of free-tropospheric and cloudy air (that is entrainment). Therefore, in-cloud turbulent convection and cloud-top wind shear constitute two competing sources of TKE within the EIL. The in-cloud convective velocity scale w_* is found to be independent of the strength of the cloud-top velocity jump Δu (for compact clouds), which explains why the EIL dynamics is observed to transition from a 'convection dominated' regime towards a 'shear dominated' regime as shear intensifies. This transition is illustrated in Fig. 1.4, showing that the shear production term is zero for $\Delta u = 0\,\text{m}\,\text{s}^{-1}$, while for $\Delta u \simeq 3\,\text{m}\,\text{s}^{-1}$ the shear production term dominates over the turbulent transport term. Besides, note that for $\Delta u \simeq 3\,\text{m}\,\text{s}^{-1}$ shear is strong enough to create a region within the EIL where the turbulent transport term turns negative, indicating an export of TKE. Still it is unclear when shear-driven turbulence starts to dominate over convection-driven turbulence, and hence the challenge is to quantify and to predict the importance of those two processes for the EIL dynamics as function of large-scale properties. In Schulz and Mellado [109], we have derived scaling laws, which predict the strength of shear-driven and convectively-driven turbulence as function of free-tropospheric and in-cloud conditions, and by comparing these two scalings we show that wind-shear effects are only significant once Δu exceeds its critical velocity jump of $(\Delta u)_{\text{crit}} \simeq 4 - 5\,w_*$. At this point two remarks are needed: First, the range $4 - 5\,w_*$ is primarily associated with variations in the sedimentation strength, demonstrating that $(\Delta u)_{\text{crit}}$ depends only moderately on the sedimentation strength. Second, it is remarkable that $(\Delta u)_{\text{crit}}$ is independent of the inversion strength, showing that $(\Delta u)_{\text{crit}}$ depends only indirectly on the thermodynamic conditions via w_*. However, this indirect dependence of w_* on the thermodynamic conditions remains to be investigated as the presented work
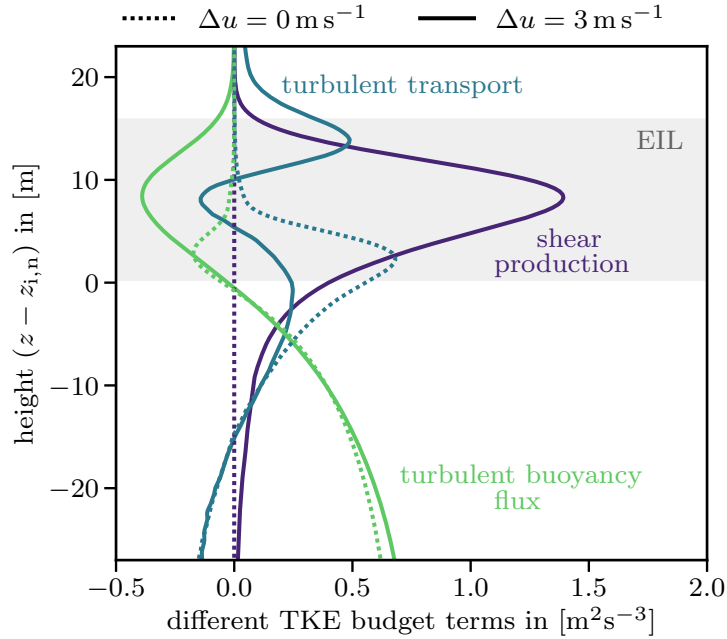
Figure 1.4: Vertical profiles of the different contributions of the turbulent kinetic energy (TKE) budget with respect to the height of zero mean buoyancy $z_{i,n}$. The gray region represents the thickness of the entrainment interfacial layer (EIL) for a strongly sheared cloud top with $\Delta u \simeq 3\,\mathrm{m\,s^{-1}}$ and $u_{\mathrm{sed}} \simeq 0\,\mathrm{mm\,s^{-1}}$, where the EIL is a transition layer separating the cloud below of the free troposphere above. The different terms of the TKE budget are defined in [109].

is limited to subtropical conditions. Typical values of w_* are reported to be in the range of $0.2 - 0.9\,\mathrm{m\,s^{-1}}$ [141], which implies $w_* \lesssim (\Delta u)_{\mathrm{crit}}$ and thus indicates that cloud-top shear generated by in-cloud turbulent convection is typically too weak to enhance cloud-top entrainment. The critical velocity jump is confirmed by Fig. 1.5, showing that only a strong shear with $\Delta u > (\Delta u)_{\mathrm{crit}}$ (that is $\Delta u \simeq 3\,\mathrm{m\,s^{-1}}$) significantly enhances the entrainment velocity. Shear effects for $\Delta u < (\Delta u)_{\mathrm{crit}}$ are negligible.

In addition, the TKE budget demonstrates a more general point, namely the importance of small-scale mixing processes. On one hand, Fig. 1.4 clearly shows how shallow the EIL is, with a typical thickness of just a few tens of meters or less. On the other hand, Fig. 1.4 indicates the complexity of the EIL, e.g., note the two peaks in the turbulent transport term. It is this shallowness combined with the complexity and importance of the EIL, which is one of the major reasons making stratocumulus so challenging to understand and to model.

In the previous paragraph we have argued that even a strong shear with $\Delta u > (\Delta u)_{\mathrm{crit}}$ does not necessarily alter in-cloud properties, e.g., in-cloud turbulence characterized by w_*. However, this statement is not expected to hold in general, as a sufficiently strong shear is expected to weaken in-cloud turbulence. This is the case because shear-enhanced entrainment of dry free-tropospheric air is expected to dry the cloud (i.e. to reduce the liquid-water specific humidity),

which weakens radiative cooling and in-cloud turbulence. Yet, it is unclear at which minimal cloud-top velocity jump this shear effects start to be significant, and an estimate of the corresponding depletion velocity jump $(\Delta u)_{\mathrm{dep}}$ is provided in Schulz and Mellado [109]. Broadly speaking, $(\Delta u)_{\mathrm{dep}}$ is based on the argument that depleting the cloud does not change the net radiative cooling as long as the extinction length—characterizing the depth over which the radiative flux divergence concentrates—remains sufficiently small compared to the cloud depth. However, shear induced depletion of the cloud decreases the cloud depth, while simultaneously increasing the extinction length. The latter is the case since the extinction length is inversely proportional to the liquid-water specific humidity, which implies that a shear induced depletion of the cloud (namely the associated decrease in liquid-water specific humidity) increases the extinction length. We therefore ask the question by how much can shear-enhanced entrainment reduce the liquid-water specific humidity for the extinction length to become comparable to the cloud depth. This line of argumentation results in a depletion velocity jump of $(\Delta u)_{\mathrm{dep}} = 3 - 10\,\mathrm{m\,s^{-1}}$ for a cloud thickness in the interval of $100 - 200\,\mathrm{m}$. We emphasize that the magnitude of the depletion velocity jump seems to be consistent with measurement campaigns as literature does not report the existence of compact clouds for $\Delta u > (\Delta u)_{\mathrm{dep}}$ [20, 39, 56, 76, 94, 139]. However, $(\Delta u)_{\mathrm{dep}}$ is partly in disagreement with previous LES studies, which report that in-cloud properties change for $\Delta u < (\Delta u)_{\mathrm{dep}}$ [62, 137, 139]. We speculate that this disagreement is at least partly caused by numerical artifacts (e.g. spurious mixing) associated with the subgrid models used in those large eddy simulations. Anyhow, further numerical and observational evidence is needed to validate $(\Delta u)_{\mathrm{dep}}$. In sum, we have answered the first research question by deriving two critical shear velocities, the first one is associated with shear-enhanced entrainment and the second one with shear induced depletion of the cloud.

Next, we address the second and third question posed in the beginning of this section. That means we ask whether droplet-sedimentation and wind-shear effects on entrainment can balance each other, and we ask how the separate contributions to w_{e} depend on the choice of the reference height z_{i} where they are calculated.

We find that the sedimentation reduction of the quasi-steady entrainment velocity $w_{\mathrm{e}} - w_{\mathrm{def}}$ is sufficiently strong to completely compensate the shear enhancement of the quasi-steady entrainment velocity $w_{\mathrm{e}} - w_{\mathrm{def}}$ (where the quasi-steady entrainment velocity quantifies the deepening of the STBL in a quasi-steady state). According to Fig. 1.5, a strong shear with $\Delta u \simeq 3\,\mathrm{m\,s^{-1}}$ and $u_{\mathrm{sed}} = 0\,\mathrm{mm\,s^{-1}}$ enhances $w_{\mathrm{e}} - w_{\mathrm{def}}$ by approximately 40%, while strong sedimentation with $u_{\mathrm{sed}} \simeq 30\,\mathrm{mm\,s^{-1}}$ and $\Delta u = 0\,\mathrm{m\,s^{-1}}$ weakens $w_{\mathrm{e}} - w_{\mathrm{def}}$ by approximately 40%. We further find that the sedimentation weakening of the quasi-steady entrainment velocity is approximately shear independent, while the shear enhancement of the quasi-steady entrainment velocity can moderately depend on sedimentation. That means imposing a strong sedimentation with $u_{\mathrm{sed}} \simeq 30\,\mathrm{mm\,s^{-1}}$ weakens $w_{\mathrm{e}} - w_{\mathrm{e}}^{\mathrm{def}}$ by approximately 40% irrespective of the imposed cloud-top velocity
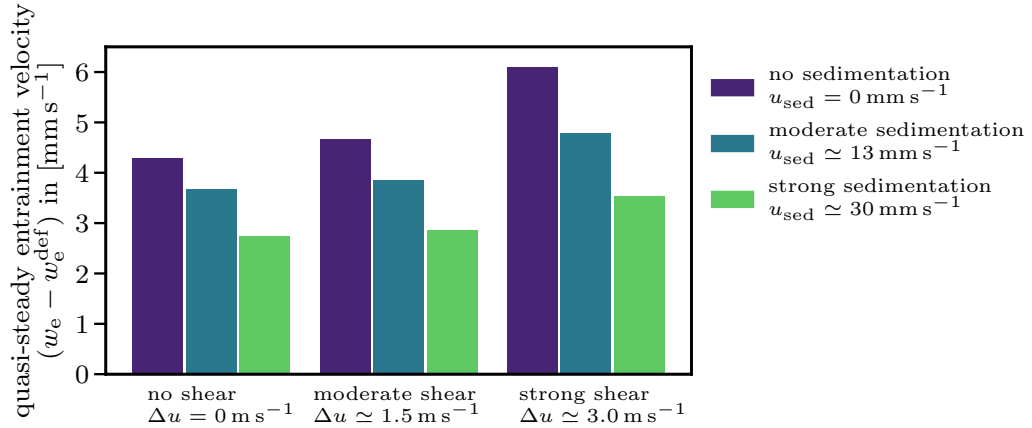
Figure 1.5: Quasi-steady entrainment velocity $w_e - w_{def}$ for different cloud-top velocity jumps Δu and different sedimentation velocities u_{sed}. Strong shear alone enhances $w_e - w_{def}$ by approximately 40% while imposing strong sedimentation alone weakens $w_e - w_{def}$ by approximately 40%. The deformation contribution w_{def} describes temporal changes in the shape of the mean buoyancy profile (see last paragraph of section 1.4 for details).

jump, while imposing a strong shear with $\Delta u \simeq 3\,\mathrm{m\,s^{-1}}$ enhances w_e by 40% for the moderate sedimentation case with $u_{sed} \simeq 13\,\mathrm{mm\,s^{-1}}$ and by 30% for the strong sedimentation case with $u_{sed} \simeq 30\,\mathrm{mm\,s^{-1}}$ (see Fig. 1.5). All this shows that, at least for subtropical conditions, droplet-sedimentation and wind-shear effects can be equally important for cloud-top entrainment. This indicates that the droplet size distribution (DSD) is important for controlling cloud lifetimes not only because of its role in rain formation but also because of its role in cloud-top entrainment. This emphasizes the need for accurate measurements of the DSD and indicates that numerical models of stratocumulus need to accurately represent variations of the DSD.

To explain these changes, wind-shear and droplet-sedimentation effects are analyzed by means of an integral analysis of the buoyancy equation, which allows us to analytically decompose the entrainment velocity $w_e = dz_i/dt$ into six different contributions, that is $w_e = w_e^{tur} + w_e^{sed} + w_e^{eva} + w_e^{rad} + w_e^{mol} + w_e^{def}$. We find that droplet-sedimentation and wind-shear mainly alter the turbulent buoyancy flux contribution w_e^{tur}, the sedimentation buoyancy flux contribution w_e^{sed}, and the evaporative cooling contribution w_e^{eva}. Changes in the radiative cooling contribution w_e^{rad}, in the molecular flux contribution w_e^{mol}, and in the deformation contribution w_e^{def} are relatively small [109, 110]. Nonetheless, changes in radiative cooling contribution w_e^{rad} are further discussed below. We observe that wind shear enhances w_e by enhancing the turbulent buoyancy flux contribution w_e^{tur}, while droplet sedimentation weakens w_e, firstly, by promoting a negative sedimentation buoyancy flux contribution w_e^{sed} [74] and, secondly, by weakening the turbulent buoyancy flux contribution w_e^{tur}. In addition, wind shear enhances w_e by amplifying mixing of cloudy and free-tropospheric air, which enhances the evaporative cooling contribution w_e^{eva}, while droplet sedimentation weakens w_e

by removing cloudy air from the EIL, which weakens the evaporative cooling contribution w_e^{eva} [1, 2, 14, 51, 74]. Due to these compensating mechanisms, wind-shear and droplet-sedimentation effects on the entrainment velocity w_e can completely balance each other.

The importance of these compensating mechanisms depends strongly on the choice of the reference height z_i, where w_e^{tur}, w_e^{sed}, and w_e^{eva} are calculated, even though different definitions of z_i typically differ only by a few meters (see Fig. 1.6). For example, for reference heights near to the lower end of the EIL ($z - z_{i,n} \simeq 0\,\text{m}$ in Fig. 1.6) the sedimentation weakening of w_e is dominated by changes in the evaporative cooling contribution w_e^{eva} and to lesser degree by changes in the sedimentation buoyancy flux contribution w_e^{sed}. (Note that even though w_e^{sed} is small, it is a 20% contribution to the sedimentation weakening of w_e for reference heights near to height of zero mean buoyancy $z_{i,n}$.) In contrast, for reference heights located within the middle of the EIL ($z - z_{i,n} \simeq 8\,\text{m}$ in Fig. 1.6), the sedimentation weakening is dominated by changes in the turbulent buoyancy flux contribution w_e^{tur} and to a lesser degree by changes in the evaporative cooling contribution w_e^{eva}. Likewise, Fig. 1.6 shows that the shear enhancement of w_e is dominated by changes in w_e^{tur} within the middle part of the EIL and by changes in w_e^{eva} within the lower part of the EIL. All this demonstrates the sensitivity of droplet-sedimentation and wind-shear effects on w_e to vertical variations of the reference height z_i.

We emphasize that the net radiative cooling remains commensurate with the net evaporative cooling for all sedimentation and shear numbers investigated, even though the radiative cooling contribution w_e^{rad} is small compared to w_e^{tur} and w_e^{eva} for reference heights located within the EIL. In this regard, we note that the radiative cooling contribution w_e^{rad} and the evaporative cooling contribution w_e^{eva} are defined as the cumulative cooling above the reference height z_i and not as the local cooling rates; and for reference heights below the EIL local radiative cooling rates exceed local evaporative cooling rates [109]. We further find that droplet-sedimentation and wind-shear effects on w_e^{rad} can partly compensate each other due to their opposing effect on the vertical transport of liquid water, namely, shear amplifies w_e^{rad} by enhancing the amount of liquid water within the EIL, while sedimentation does the opposite and weakens w_e^{rad} by removing liquid water from the EIL. This finding is expected to become more important under different thermodynamic conditions, e.g., a smaller jump in total-water specific humidity is expected to increase the importance of radiative compared to evaporative cooling [e.g. 72].

The preceding discussion indicates that entrainment velocity parameterization (as needed in mixed-layer models) should pay equal attention to droplet-sedimentation and to wind-shear effects. In addition, our results demonstrate that the separate contributions to w_e need to be estimated at the same reference height z_i, even though different definitions of z_i typically only differ by a few meters. Moreover, analyzing the separate contributions to w_e reveals that parameterizing w_e^{eva} has priority for reference heights located near to the lower end
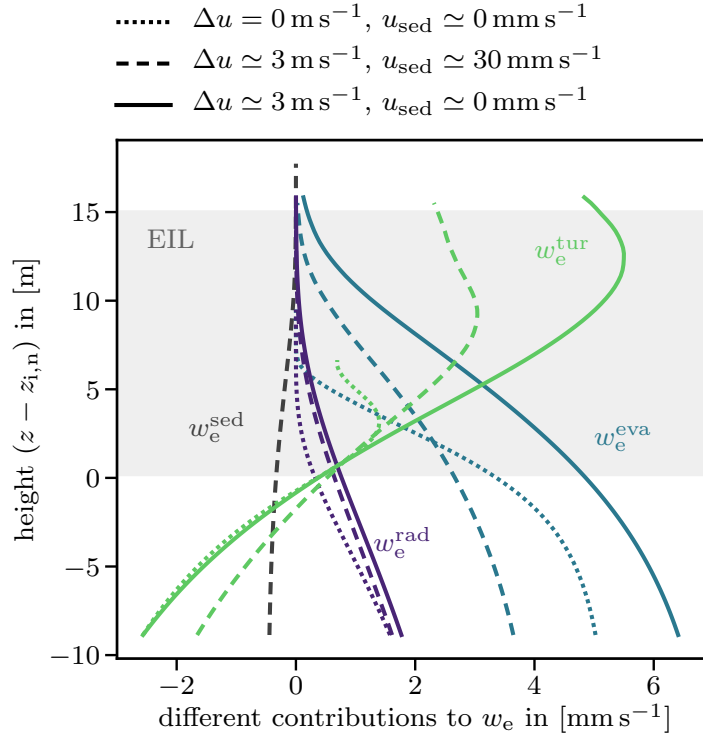
Figure 1.6: Vertical profiles of the different contributions to the entrainment velocity $w_\mathrm{e} = w_\mathrm{e}^\mathrm{tur} + w_\mathrm{e}^\mathrm{eva} + w_\mathrm{e}^\mathrm{rad} + w_\mathrm{e}^\mathrm{sed} + w_\mathrm{e}^\mathrm{mol} + w_\mathrm{e}^\mathrm{def}$ with respect to the height of zero mean buoyancy $z_\mathrm{i,n}$. Different line styles indicate different combinations of the cloud-top velocity jump Δu and the sedimentation velocity u_sed. The gray region represents the thickness of the entrainment interfacial layer (EIL) for a strongly sheared cloud top with $\Delta u \simeq 3\,\mathrm{m\,s^{-1}}$ and $u_\mathrm{sed} \simeq 30\,\mathrm{mm\,s^{-1}}$.

of the EIL ($z - z_\mathrm{i,n} \simeq 0\,\mathrm{m}$ in Fig. 1.6), while parameterizing $w_\mathrm{e}^\mathrm{eva}$ and $w_\mathrm{e}^\mathrm{tur}$ has priority for reference heights located within the middle of the EIL ($z - z_\mathrm{i,n} \simeq 8\,\mathrm{m}$ in Fig. 1.6). Our results further indicate that, at least for the subtropical conditions considered here, parameterizing the radiative cooling contribution $w_\mathrm{e}^\mathrm{rad}$ and the sedimentation flux contribution $w_\mathrm{e}^\mathrm{sed}$ has no priority. However, this statement should not be interpreted as radiative cooling being unimportant, as for example the evaporative cooling contribution $w_\mathrm{e}^\mathrm{eva}$ scales with the strength of radiative cooling [e.g. 72]. In summary, all this demonstrates the importance of the detailed vertical structure of the EIL for deriving entrainment velocity parametrizations.

In a quasi-steady state in-cloud and free-tropospheric conditions vary slowly compared to cloud-top processes. In other words, in a quasi-steady state the shape of the mean buoyancy profile changes slowly compared to the deepening of the stratocumulus-topped boundary layer (STBL), which implies that the deformation contribution $w_\mathrm{e}^\mathrm{def}$—characterizing how fast the shape of the mean buoyancy profile changes—is small compared to the sum $w_\mathrm{e}^\mathrm{tur} + w_\mathrm{e}^\mathrm{sed} + w_\mathrm{e}^\mathrm{eva} + w_\mathrm{e}^\mathrm{rad} + w_\mathrm{e}^\mathrm{mol}$. However, in an unsteady state this is not the case and the STBL deepens on time scales comparable to the large-eddy turnover time, implying that temporal changes in the shape of the mean buoyancy profile are non-negligible. As argued

in Schulz and Mellado [109], the magnitude of the entrainment velocity depends on the choice of the reference height z_i in an unsteady state, indicating that in unsteady states the deepening of the STBL is not well described by means of one single reference height z_i. This might for example be the case during cloud formation and during transients, e.g., the transient from stratocumulus to shallow cumulus. In contrast, in a quasi-steady state, the magnitude of w_e is approximately independent of the choice of the reference height z_i and only the partitioning between the separate contributions to w_e depends on the choice of z_i. For that reason the quasi-steady entrainment velocity $w_e - w_e^{\mathrm{def}} = w_e^{\mathrm{tur}} + w_e^{\mathrm{sed}} + w_e^{\mathrm{eva}} + w_e^{\mathrm{rad}} + w_e^{\mathrm{mol}}$ is presented in Fig. 1.5. The quasi-steady entrainment velocity in Fig. 1.5 is on the order of $3 - 6\,\mathrm{mm\,s^{-1}}$, which is commensurate with field measurements reporting entrainment velocities in the range of $4 - 5\,\mathrm{mm\,s^{-1}}$ [39, 123]. This good agreement shows, that DNS are well suited for studying cloud-top entrainment, despite the low-to-moderate Reynolds numbers and despite the simplified configurations (cf. section 1.2).

1.5 OUTLOOK

Of course there are open questions left. In general the presented results demonstrate that entrainment is to a substantial part an interfacial layer process. Yet, it is known that changes in large-scale environmental conditions can substantially alter cloud-top entrainment in stratocumulus. This concerns for example the question of how variations in the surface heat and moisture fluxes affect cloud-top entrainment and thus the temporal evolution of the STBL. Likewise, it remains uncertain how changes in the thermodynamic properties of the inversion affect cloud-top entrainment. For instance, it is expected that smaller jumps in total-water humidity will increase the importance of radiative cooling compared to evaporative cooling. All this shows that it remains unclear how changes in large-scale environmental conditions affect the various cloud-top processes (e.g. wind shear or evaporative cooling) and more holistic studies of the STBL are needed to address this question.

However, neither DNS or LES alone seem to be suited to address this question. On one hand, DNS are in particular well suited for studying small-scale mixing processes. Moreover, DNS have the advantage that they reproduce many of the experimentally observed properties of the STBL without being tuned to do so. This is for example the case for the entrainment velocity w_e, as demonstrated in section 1.4, and this is the case for the vertical profiles of the second- and third-order moment of the vertical velocity fluctuations as demonstrated by Mellado et al. [87]. However, DNS are computationally demanding and therefore they are not suited for studying the response of the STBL to changes in large-scale conditions (cf. section 1.2). On the other hand, LES are faster and thus allow for a more holistic study of the STBL, however, they suffer from an inadequate representation of small-scale mixing processes, which for example implies that their entrainment velocities need to be tuned to realistic values (cf. section 1.2). For all these reasons Mellado et al. [87] argued that combining DNS and LES is a

promising path for advancing our understanding of stratocumulus. For instance, LES could be used to study the sensitivity of the entrainment velocity to changes in environmental conditions, while parallel performed DNS could be used to verify a subset of these LES studies by providing accurate reference data. In this way DNS could complement field measurements. More generally, such an experiment could be used to verify or to disprove the LES hypothesis, namely: "LES accurately quantifies the sensitivity of stratocumulus to changes in environmental conditions, even though cloud-top entrainment is not properly represented in LES" [87].

In addition, this dissertation highlights the sensitivity of cloud-top entrainment to changes in the droplet size distribution (DSD). However, important aspects regarding the temporal evolution of the DSD remain unclear. Lagrangian studies of the DSD have for example often considered homogenous isotropic turbulence and we need to understand how small-scale inhomogeneities—like stable stratification—affect the DSD. At these scales DNS seem to be the appropriate tool [87]. However, at the same time we need to understand how variations of thermodynamic fields, e.g., through growth history effects, affect the DSD [46, 70, 87, 92] and these scales are more appropriately studied by means of LES. For these and similar reasons Mellado et al. [87] argued that combining DNS and LES is a promising tool for studying the temporal evolution of the DSD [87]. In summary, the preceding two paragraphs indicate that stratocumulus pose a challenge, which needs to be addressed with combined forces of DNS and LES.

Finite-time phase changes are believed to be among the most important microphysical processes for non-precipitating stratocumulus [84]. However, the presented results are based on a phase-equilibrium assumption (infinitely fast thermodynamics), which poses the question if and how our results change if finite condensation and evaporation rates are considered. Typically cloud droplets need a few tens of seconds to adjust to local changes in relative humidity and thus assuming phase equilibrium is inappropriate for length scales smaller than a few meters as eddies on these length scales break up before achieving thermodynamic equilibrium [42, 78, 111]. However, it could be argued that it is the average time an air parcels spends in the EIL (the resident time), which determines if a cloud droplet gets evaporated or not, and since the resident time is typically a few minutes [61, 70, 75, 120] finite-time evaporation effects might be weak for mean quantities. Anyhow, there are two main ways by which finite-time evaporation changes cloud-top entrainment. First, evaporative-cooling rates decrease as the phase relaxation time increases [51, 71, 138]. Second, the evaporation time scale allows to differentiate between homogenous and inhomogenous mixing. If the mixing time scale for homogenization of the entrained air is much shorter than the evaporation time scale, mixing is homogenous and all droplet collectively shrink. In contrast, if the evaporation time scale is much smaller than the mixing time scale needed for homogenization of the entrained air, mixing is inhomogenous and single droplets get evaporated while the remaining droplets do not change size [7, 51, 55]. Therefore, the DSD evolves differently depending on the mixing assumption. Observations indicate that mixing in stratocumulus is

predominantly inhomogenous [51, and references therein], which suggests that at least the mixing-assumption effect might be small for the performed DNS (as the performed DNS assume inhomogenous mixing). However, it remains unclear how important changes in the evaporative-cooling rate are. In sum, all this indicates that finite-time evaporation effects need to be better quantified and understood.

In the long term the presented results aim to improve entrainment velocity parametrizations as needed in mixed-layer models. In section 1.4 we argued that much of our understanding of STBL is based on mixed-layer models, but we also argued that it remains difficult to use mixed-layer models for making quantitative predictions of the STBL evolution due to substantial uncertainties in current entrainment velocity parametrizations [39, 67, 117, 134]. This is remarkable since the mixed-layer framework, and accordingly entrainment velocity parametrizations, have been introduced more than 40 years ago by Lilly [65]. One promising approach to derive more accurate entrainment velocity parametrizations is based on an integral analysis of the buoyancy equation, which allows to analytically decompose the entrainment velocity w_e into separate contributions, e.g., resulting from mixing, sedimentation, evaporation, and radiation, and one finds $w_e = w_e^{tur} + w_e^{sed} + w_e^{eva} + w_e^{rad} + w_e^{mol} + w_e^{def}$ according to section 1.4. The challenge is hence to scale these separate contributions as function of in-cloud and free-tropospheric conditions, that is for example as function of wind shear, droplet sedimentation, surface heat and moisture fluxes, and the inversion strength. All these processes are coupled, strongly nonlinear, and depend critically on the choice of the reference height z_i where $w_e = dz_i/dt$ is calculated, even though different definitions of z_i only differ by a few meters (cf. section 1.4). All these factors illustrate the challenge of deriving entrainment velocity parametrizations. For a discussion of current entrainment velocity parametrizations we refer the reader to [66, 67, 72–74, 117, 123, and references therein]. Here, we only note that to the best of our knowledge none of the current entrainment velocity parametrizations (for a STBL) considers wind-shear effects, even though wind-shear effects are known to be important. Likewise, droplet-sedimentation effects are important but typically not considered [except in 17, 74]. We emphasize that the presented results aid parameterization development of this kind as argued in section 1.4. Once a shear dependent entrainment velocity parameterization is available, one could for example extend the work by Bretherton and Wyant [17] and study shear effects on the stratocumulus to cumulus transition by means of a mixed-layer model. In general, a more accurate entrainment velocity parameterization will empower mixed-layer models to assess more accurately how low clouds change under a warming climate [e.g. 22, 30]. In summary, all this illustrates that more accurate entrainment velocity parametrizations are necessary to better understand the role of stratocumulus under a warming climate.

BIBLIOGRAPHY

[1] Andrew S Ackerman et al. "The impact of humidity above stratiform clouds on indirect aerosol climate forcing." In: *Nature* 432.7020 (2004), p. 1014.

[2] Andrew S Ackerman et al. "Large-eddy simulations of a drizzling, stratocumulus-topped marine boundary layer." In: *Monthly Weather Review* 137.3 (2009), pp. 1083–1110.

[3] Bruce A Albrecht, Richard S Penc, and Wayne H Schubert. "An observational study of cloud-topped mixed layers." In: *Journal of the atmospheric sciences* 42.8 (1985), pp. 800–822.

[4] A Arakawa. "Modelling clouds and cloud processes for use in climate models." In: *WMO The Phys. Basis of Climate and Climate Modelling p 183-197(SEE N 76-19675 10-47)* (1975).

[5] Akio Arakawa and Wayne Howard Schubert. "Interaction of a cumulus cloud ensemble with the large-scale environment, Part I." In: *Journal of the Atmospheric Sciences* 31.3 (1974), pp. 674–701.

[6] Nathan P Arnold and David A Randall. "Global-scale convective aggregation: Implications for the Madden-Julian Oscillation." In: *Journal of Advances in Modeling Earth Systems* 7.4 (2015), pp. 1499–1518.

[7] MB Baker and J Latham. "The evolution of droplet spectra and the rate of production of embryonic raindrops in small cumulus clouds." In: *Journal of the Atmospheric Sciences* 36.8 (1979), pp. 1612–1615.

[8] Matthew J Beals et al. "Holographic measurements of inhomogeneous cloud mixing at the centimeter scale." In: *Science* 350.6256 (2015), pp. 87–90.

[9] Craig F Bohren and Eugene E Clothiaux. *Fundamentals of atmospheric radiation: an introduction with 400 problems.* John Wiley & Sons, 2006.

[10] Sandrine Bony and Jean-Louis Dufresne. "Marine boundary layer clouds at the heart of tropical cloud feedback uncertainties in climate models." In: *Geophysical Research Letters* 32.20 (2005).

[11] Sandrine Bony et al. "Clouds, circulation and climate sensitivity." In: *Nature Geoscience* 8.4 (2015), p. 261.

[12] Sandrine Bony et al. "EUREC4A: a field campaign to elucidate the couplings between clouds, convection and circulation." In: *Surveys in Geophysics* 38.6 (2017), pp. 1529–1568.

[13] Sandrine Bony, Bjorn Stevens, and David Carlson. "Understanding clouds to anticipate future climate." In: *WMO Bulletin* 66 (2017), pp. 8–11.

[14] CS Bretherton, Peter N Blossey, and Junya Uchida. "Cloud droplet sedimentation, entrainment efficiency, and subtropical stratocumulus albedo." In: *Geophysical research letters* 34.3 (2007).

[15]   Christopher S Bretherton. "Insights into low-latitude cloud feedbacks from high-resolution models." In: *Phil. Trans. R. Soc. A* 373.2054 (2015), p. 20140415.

[16]   Christopher S Bretherton and Marat F Khairoutdinov. "Convective self-aggregation feedbacks in near-global cloud-resolving simulations of an aquaplanet." In: *Journal of Advances in Modeling Earth Systems* 7.4 (2015), pp. 1765–1787.

[17]   Christopher S Bretherton and Matthew C Wyant. "Moisture transport, lower-tropospheric stability, and decoupling of cloud-topped boundary layers." In: *Journal of the atmospheric sciences* 54.1 (1997), pp. 148–167.

[18]   Christopher S Bretherton et al. "An intercomparison of radiatively driven entrainment and turbulence in a smoke cloud, as simulated by different numerical models." In: *Quarterly Journal of the Royal Meteorological Society* 125.554 (1999), pp. 391–423.

[19]   Christopher S Bretherton et al. "The EPIC 2001 stratocumulus study." In: *Bulletin of the American Meteorological Society* 85.7 (2004), pp. 967–978.

[20]   RA Brost, JC Wyngaard, and DH Lenschow. "Marine stratocumulus layers. Part II: Turbulence budgets." In: *Journal of the Atmospheric Sciences* 39.4 (1982), pp. 818–836.

[21]   Kyle A Brucker and Sutanu Sarkar. "Evolution of an initially turbulent stratified shear layer." In: *Physics of Fluids (1994-present)* 19.10 (2007), p. 105105.

[22]   Peter M Caldwell, Yunyan Zhang, and Stephen A Klein. "CMIP3 subtropical stratocumulus cloud feedback interpreted through a mixed-layer model." In: *Journal of Climate* 26.5 (2013), pp. 1607–1625.

[23]   Jeffrey Richard Carpenter, GA Lawrence, and William D Smyth. "Evolution and mixing of asymmetric Holmboe instabilities." In: *Journal of Fluid Mechanics* 582 (2007), pp. 103–132.

[24]   SJ Caughey, BA Crease, and WT Roach. "A field study of nocturnal stratocumulus II Turbulence structure and entrainment." In: *Quarterly Journal of the Royal Meteorological Society* 108.455 (1982), pp. 125–144.

[25]   Jule G Charney et al. *Carbon dioxide and climate: a scientific assessment*. National Academy of Sciences, Washington, DC, 1979.

[26]   Amy C Clement, Robert Burgman, and Joel R Norris. "Observational and model evidence for positive low-level cloud feedback." In: *Science* 325.5939 (2009), pp. 460–464.

[27]   David Coppin and Sandrine Bony. "Physical mechanisms controlling the initiation of convective self-aggregation in a General Circulation Model." In: *Journal of Advances in Modeling Earth Systems* 7.4 (2015), pp. 2060–2078.

[28]   S Dal Gesso et al. "A mixed-layer model perspective on stratocumulus steady states in a perturbed climate." In: *Quarterly Journal of the Royal Meteorological Society* 140.684 (2014), pp. 2119–2131.

[29]   Chimene L Daleu et al. "Intercomparison of methods of coupling between convection and large-scale circulation: 1. Comparison over uniform surface conditions." In: *Journal of advances in modeling earth systems* 7.4 (2015), pp. 1576–1601.

[30]   Stephan R De Roode et al. "A mixed-layer model study of the stratocumulus response to changes in large-scale conditions." In: *Journal of Advances in Modeling Earth Systems* 6.4 (2014), pp. 1256–1270.

[31]   Stephan R De Roode et al. "Large-eddy simulations of EUCLIPSE–GASS Lagrangian stratocumulus-to-cumulus transitions: Mean state, turbulence, and decoupling." In: *Journal of the Atmospheric Sciences* 73.6 (2016), pp. 2485–2508.

[32]   Wim C De Rooy et al. "Entrainment and detrainment in cumulus convection: An overview." In: *Quarterly Journal of the Royal Meteorological Society* 139.670 (2013), pp. 1–19.

[33]   JW Deardorff. "Cloud top entrainment instability." In: *Journal of the Atmospheric Sciences* 37.1 (1980), pp. 131–147.

[34]   James W Deardorff. "Parameterization of the planetary boundary layer for use in general circulation models." In: *Monthly Weather Review* 100.2 (1972), pp. 93–106.

[35]   James W Deardorff. "Stratocumulus-capped mixed layers derived from a three-dimensional model." In: *Boundary-Layer Meteorology* 18.4 (1980), pp. 495–527.

[36]   Paul E Dimotakis. "Turbulent mixing." In: *Annu. Rev. Fluid Mech.* 37 (2005), pp. 329–356.

[37]   AGM Driedonks and PG Duynkerke. "Current problems in the stratocumulus-topped atmospheric boundary layer." In: *Boundary-Layer Meteorology* 46.3 (1989), pp. 275–303.

[38]   JJ Dussen et al. "The GASS/EUCLIPSE model intercomparison of the stratocumulus transition as observed during ASTEX: LES results." In: *Journal of Advances in Modeling Earth Systems* 5.3 (2013), pp. 483–499.

[39]   Ian Faloona et al. "Observations of entrainment in eastern Pacific marine stratocumulus using three conserved scalars." In: *Journal of the atmospheric sciences* 62.9 (2005), pp. 3268–3285.

[40]   Jacob P Fugal and Raymond A Shaw. "Cloud particle size distributions measured with an airborne digital in-line holographic instrument." In: *Atmospheric Measurement Techniques* 2.1 (2009), pp. 259–271.

[41]   Jacob P Fugal et al. "Airborne digital holographic system for cloud particle measurements." In: *Applied optics* 43.32 (2004), pp. 5987–5995.

[42]   H Gerber et al. "Spectral density of cloud liquid water content at high frequencies." In: *Journal of the atmospheric sciences* 58.5 (2001), pp. 497–503.

[43]   H Gerber, Szymon P Malinowski, and Haflidi Jonsson. "Evaporative and radiative cooling in POST Stratocumulus." In: *Journal of the Atmospheric Sciences* 73.10 (2016), pp. 3877–3884.

[44] Hermann Gerber et al. "Entrainment rates and microphysics in POST stratocumulus." In: *Journal of Geophysical Research: Atmospheres* 118.21 (2013), pp. 12–094.

[45] S Glienke et al. "Cloud droplets to drizzle: Contribution of transition drops to microphysical and optical properties of marine stratocumulus clouds." In: *Geophysical Research Letters* 44.15 (2017), pp. 8002–8010.

[46] Wojciech W Grabowski and Gustavo C Abade. "Broadening of cloud droplet spectra through eddy hopping: Turbulent adiabatic parcel simulations." In: *Journal of the Atmospheric Sciences* 74.5 (2017), pp. 1485–1493.

[47] Daniel P Grosvenor et al. "Remote sensing of droplet number concentration in warm clouds: A review of the current state of knowledge and perspectives." In: *Reviews of Geophysics* (2018).

[48] Krzysztof E Haman et al. "Small scale mixing processes at the top of a marine stratocumulus—A case study." In: *Quarterly Journal of the Royal Meteorological Society* 133.622 (2007), pp. 213–226.

[49] R Heinze et al. *Large-eddy simulations over Germany using ICON: a comprehensive evaluation, QJ Roy. Meteorol. Soc., 143, 69–100.* 2017.

[50] Arnaud Hélière et al. "The EarthCARE mission: mission concept and lidar instrument pre-development." In: *2007 IEEE International Geoscience and Remote Sensing Symposium*. IEEE. 2007, pp. 4975–4978.

[51] Adrian A Hill, Graham Feingold, and Hongli Jiang. "The influence of entrainment and mixing assumption on aerosol–cloud interactions in marine stratocumulus." In: *Journal of the Atmospheric Sciences* 66.5 (2009), pp. 1450–1464.

[52] Cathy Hohenegger and Bjorn Stevens. "Coupled radiative convective equilibrium simulations with explicit and parameterized convection." In: *Journal of Advances in Modeling Earth Systems* 8.3 (2016), pp. 1468–1482.

[53] Marcin J Kurowski, Szymon P Malinowski, and Wojciech W Grabowski. "A numerical investigation of entrainment and transport within a stratocumulus-topped boundary layer." In: *Quarterly Journal of the Royal Meteorological Society* 135.638 (2009), pp. 77–92.

[54] Imai Jen-La Plante et al. "Physics of Stratocumulus Top (POST): turbulence characteristics." In: *Atmospheric Chemistry and Physics* 16.15 (2016), pp. 9711–9725.

[55] JB Jensen et al. "Turbulent mixing, spectral evolution and dynamics in a warm cumulus cloud." In: *Journal of the atmospheric sciences* 42.2 (1985), pp. 173–192.

[56] J Katzwinkel, H Siebert, and RA Shaw. "Observation of a self-limiting, shear-induced turbulent inversion layer above marine stratocumulus." In: *Boundary-layer meteorology* 145.1 (2012), pp. 131–143.

[57] Marat F Khairoutdinov et al. "Large-eddy simulation of maritime deep tropical convection." In: *Journal of Advances in Modeling Earth Systems* 1.4 (2009).

[58] Marat Khairoutdinov and David Randall. "High-resolution simulation of shallow-to-deep convection transition over land." In: *Journal of the atmospheric sciences* 63.12 (2006), pp. 3421–3436.

[59] Daniel Klocke et al. "Rediscovery of the doldrums in storm-resolving simulations over the tropical Atlantic." In: *Nature Geoscience* 10.12 (2017), p. 891.

[60] Reto Knutti, Maria AA Rugenstein, and Gabriele C Hegerl. "Beyond equilibrium climate sensitivity." In: *Nature Geoscience* 10.10 (2017), p. 727.

[61] Yefim L Kogan. "Large-eddy simulation of air parcels in stratocumulus clouds: Time scales and spatial variability." In: *Journal of the atmospheric sciences* 63.3 (2006), pp. 952–967.

[62] Marta K Kopec, Szymon P Malinowski, and Zbigniew P Piotrowski. "Effects of wind shear and radiative cooling on the stratocumulus-topped boundary layer." In: *Quarterly Journal of the Royal Meteorological Society* 142.701 (2016), pp. 3222–3233.

[63] Steven K Krueger. "Linear eddy modeling of entrainment and mixing in stratus clouds." In: *Journal of the atmospheric sciences* 50.18 (1993), pp. 3078–3090.

[64] Hung-Chi Kuo and Wayne H Schubert. "Stability of cloud-topped boundary layers." In: *Quarterly Journal of the Royal Meteorological Society* 114.482 (1988), pp. 887–916.

[65] Douglas K Lilly. "Models of cloud-topped mixed layers under a strong inversion." In: *Quart. J. Roy. Meteor. Soc* 94.401 (1968), pp. 292–309.

[66] Douglas K Lilly. "Entrainment into mixed layers. Part II: A new closure." In: *Journal of the atmospheric sciences* 59.23 (2002), pp. 3353–3361.

[67] Douglas K Lilly and Bjorn Stevens. "Validation of a mixed-layer closure. I: theoretical tests." In: *Quarterly Journal of the Royal Meteorological Society* 134.630 (2008), pp. 47–55.

[68] AP Lock and MK MacVean. "The generation of turbulence and entrainment by buoyancy reversal." In: *Quarterly Journal of the Royal Meteorological Society* 125.555 (1999), pp. 1017–1038.

[69] Ulrike Lohmann and Johann Feichter. "Global indirect aerosol effects: a review." In: *Atmospheric Chemistry and Physics* 5.3 (2005), pp. 715–737.

[70] Alberto de Lozar and Lukas Muessle. "Long-resident droplets at the stratocumulus top." In: *Atmospheric Chemistry and Physics* 16.10 (2016), pp. 6563–6576.

[71] Alberto de Lozar and Juan Pedro Mellado. "Cloud droplets in a bulk formulation and its application to buoyancy reversal instability, QJ Roy." In: *Meteor. Soc* 140 (2014), pp. 1493–1504.

[72] Alberto de Lozar and Juan Pedro Mellado. "Evaporative cooling amplification of the entrainment velocity in radiatively driven stratocumulus." In: *Geophysical Research Letters* 42.17 (2015), pp. 7223–7229.

[73]   Alberto de Lozar and Juan Pedro Mellado. "Mixing driven by radiative and evaporative cooling at the stratocumulus top." In: *Journal of the Atmospheric Sciences* 72.12 (2015), pp. 4681–4700.

[74]   Alberto de Lozar and Juan Pedro Mellado. "Reduction of the entrainment velocity by cloud droplet sedimentation in stratocumulus." In: *Journal of the Atmospheric Sciences* 74.3 (2017), pp. 751–765.

[75]   L Magaritz et al. "Investigation of droplet size distributions and drizzle formation using a new trajectory ensemble model. Part II: Lucky parcels." In: *Journal of the Atmospheric Sciences* 66.4 (2009), pp. 781–805.

[76]   SP Malinowski et al. "Physics of Stratocumulus Top (POST): turbulent mixing across capping inversion." In: *Atmospheric Chemistry and Physics* 13.24 (2013), pp. 12171–12186.

[77]   GM Martin, DW Johnson, and An Spice. "The measurement and parameterization of effective radius of droplets in warm stratocumulus clouds." In: *Journal of the Atmospheric Sciences* 51.13 (1994), pp. 1823–1842.

[78]   Ilia Mazin. "The effect of condensation and evaporation on turbulence in clouds." In: *Atmos. Res* 51 (1999), pp. 171–174.

[79]   Jeremy McGibbon and CS Bretherton. "Skill of ship-following large-eddy simulations in reproducing MAGIC observations across the northeast Pacific stratocumulus to cumulus transition region." In: *Journal of Advances in Modeling Earth Systems* 9.2 (2017), pp. 810–831.

[80]   Brian Medeiros, Alex Hall, and Bjorn Stevens. "What controls the mean depth of the PBL?" In: *Journal of climate* 18.16 (2005), pp. 3157–3172.

[81]   Brian Medeiros et al. "Aquaplanets, climate sensitivity, and low clouds." In: *Journal of Climate* 21.19 (2008), pp. 4974–4991.

[82]   Brian Medeiros, Bjorn Stevens, and Sandrine Bony. "Using aquaplanets to understand the robust responses of comprehensive climate models to forcing." In: *Climate dynamics* 44.7-8 (2015), pp. 1957–1977.

[83]   Juan Pedro Mellado. "The evaporatively driven cloud-top mixing layer." In: *Journal of Fluid Mechanics* 660 (2010), pp. 5–36.

[84]   Juan Pedro Mellado. "Cloud-Top Entrainment in Stratocumulus Clouds." In: *Annual Review of Fluid Mechanics* 49 (2017), pp. 145–169.

[85]   Juan Pedro Mellado et al. "Buoyancy reversal in cloud-top mixing layers." In: *Quarterly Journal of the Royal Meteorological Society* 135.641 (2009), pp. 963–978.

[86]   Juan Pedro Mellado, Bjorn Stevens, and Heiko Schmidt. "Wind shear and buoyancy reversal at the top of stratocumulus." In: *Journal of the Atmospheric Sciences* 71.3 (2014), pp. 1040–1057.

[87]   Juan-Pedro Mellado et al. "DNS and LES for simulating stratocumulus: Better together." In: *Journal of Advances in Modeling Earth Systems* (2018).

[88]   Chin-Hoh Moeng. "Large-eddy simulation of a stratus-topped boundary layer. Part I: Structure and budgets." In: *Journal of the atmospheric sciences* 43.23 (1986), pp. 2886–2900.

[89] Chin-Hoh Moeng, Shaohua Shen, and David A Randall. "Physical processes within the nocturnal stratus-topped boundary layer." In: *Journal of the atmospheric sciences* 49.24 (1992), pp. 2384–2401.

[90] Mitchell W Moncrieff and Changhai Liu. "Representing convective organization in prediction models by a hybrid strategy." In: *Journal of the atmospheric sciences* 63.12 (2006), pp. 3404–3420.

[91] Caroline Muller and Sandrine Bony. "What favors convective aggregation and why?" In: *Geophysical Research Letters* 42.13 (2015), pp. 5626–5634.

[92] Ann Kristin Naumann and Axel Seifert. "Recirculation and growth of raindrops in simulated shallow cumulus." In: *Journal of Advances in Modeling Earth Systems* 8.2 (2016), pp. 520–537.

[93] S Nicholls and J Leighton. "An observational study of the structure of stratiform cloud sheets: Part I. Structure." In: *Quarterly Journal of the Royal Meteorological Society* 112.472 (1986), pp. 431–460.

[94] S Nicholls and JD Turton. "An observational study of the structure of stratiform cloud sheets: Part II. Entrainment." In: *Quarterly Journal of the Royal Meteorological Society* 112.472 (1986), pp. 461–480.

[95] Ji Nie, Daniel A Shaevitz, and Adam H Sobel. "Forcings and feedbacks on convection in the 2010 Pakistan flood: Modeling extreme precipitation with interactive large-scale ascent." In: *Journal of Advances in Modeling Earth Systems* 8.3 (2016), pp. 1055–1072.

[96] Thor Erik Nordeng. "Extended versions of the convective parametrization scheme at ECMWF and their impact on the mean and transient activity of the model in the tropics." In: *Research Department Technical Memorandum* 206 (1994), pp. 1–41.

[97] JG Pedersen et al. "Anisotropy of observed and simulated turbulence in marine stratocumulus." In: *Journal of Advances in Modeling Earth Systems* 10.2 (2018), pp. 500–515.

[98] Jesper G Pedersen, Szymon P Malinowski, and Wojciech W Grabowski. "Resolution and domain-size sensitivity in implicit large-eddy simulation of the stratocumulus-topped boundary layer." In: *Journal of Advances in Modeling Earth Systems* 8.2 (2016), pp. 885–903.

[99] JL Pelly and SE Belcher. "A mixed-layer model of the well-mixed stratocumulus-topped boundary layer." In: *Boundary-layer meteorology* 100.1 (2001), pp. 171–187.

[100] WR Peltier and CP Caulfield. "Mixing efficiency in stratified shear flows." In: *Annual review of fluid mechanics* 35.1 (2003), pp. 135–167.

[101] Grant William Petty. *A first course in atmospheric radiation*. Sundog Pub, 2006.

[102] David A Randall. "Conditional instability of the first kind upside-down." In: *Journal of the Atmospheric Sciences* 37.1 (1980), pp. 125–130.

[103]   David A Randall and Max J Suarez. "On the dynamics of stratocumulus formation and dissipation." In: *Journal of the atmospheric sciences* 41.20 (1984), pp. 3052–3057.

[104]   David Randall et al. "Breaking the cloud parameterization deadlock." In: *Bulletin of the American Meteorological Society* 84.11 (2003), pp. 1547–1564.

[105]   Malte Rieck, Louise Nuijens, and Bjorn Stevens. "Marine boundary layer cloud feedbacks in a constant relative humidity atmosphere." In: *Journal of the Atmospheric Sciences* 69.8 (2012), pp. 2538–2550.

[106]   Stephan R de Roode and Qing Wang. "Do stratocumulus clouds detrain? FIRE I data revisited." In: *Boundary-layer meteorology* 122.2 (2007), pp. 479–491.

[107]   Irina Sandu and Bjorn Stevens. "On the factors modulating the stratocumulus to cumulus transitions." In: *Journal of the Atmospheric Sciences* 68.9 (2011), pp. 1865–1881.

[108]   Tapio Schneider et al. "Climate goals and computing the future of clouds." In: *Nature Climate Change* 7.1 (2017), p. 3.

[109]   Bernhard Schulz and Juan Pedro Mellado. "Wind Shear Effects on Radiatively and Evaporatively Driven Stratocumulus Tops." In: *Journal of the Atmospheric Sciences* 75.9 (2018), pp. 3245–3263. DOI: 10.1175/JAS-D-18-0027.1.

[110]   Bernhard Schulz and Juan Pedro Mellado. "Competing Effects of Droplet Sedimentation and Wind Shear on Entrainment in Stratocumulus." In: *Journal of Advances in Modeling Earth Systems* 11 (2019). DOI: 10.1029/2019MS001617.

[111]   Raymond A Shaw. "Particle-turbulence interactions in atmospheric clouds." In: *Annual Review of Fluid Mechanics* 35.1 (2003), pp. 183–227.

[112]   Steven C Sherwood, Sandrine Bony, and Jean-Louis Dufresne. "Spread in model climate sensitivity traced to atmospheric convective mixing." In: *Nature* 505.7481 (2014), p. 37.

[113]   Shenqyang S Shy and Robert E Breidenthal. "Laboratory experiments on the cloud-top entrainment instability." In: *Journal of Fluid Mechanics* 214 (1990), pp. 1–15.

[114]   Steven T Siems and Christopher S Bretherton. "A Numerical Investigation of Cloud-Top Entrainment Instability and Related Experiments." In: *Quarterly Journal of the Royal Meteorological Society* 118.507 (1992), pp. 787–818.

[115]   WD Smyth, JR Carpenter, and GA Lawrence. "Mixing in symmetric Holmboe waves." In: *Journal of physical oceanography* 37.6 (2007), pp. 1566–1583.

[116]   William D Smyth and James N Moum. "Length scales of turbulence in stably stratified mixing layers." In: *Physics of Fluids (1994-present)* 12.6 (2000), pp. 1327–1342.

[117]   Bjorn Stevens. "Entrainment in stratocumulus-topped mixed layers." In: *Quarterly Journal of the Royal Meteorological Society* 128.586 (2002), pp. 2663–2690.

[118]   Bjorn Stevens. "Atmospheric moist convection." In: *Annu. Rev. Earth Planet. Sci.* 33 (2005), pp. 605–643.

[119]   Bjorn Stevens. "Bulk boundary-layer concepts for simplified models of tropical dynamics." In: *Theoretical and Computational Fluid Dynamics* 20.5-6 (2006), pp. 279–304.

[120]   Bjorn Stevens et al. "Elements of the microphysical structure of numerically simulated nonprecipitating stratocumulus." In: *Journal of the atmospheric sciences* 53.7 (1996), pp. 980–1006.

[121]   Bjorn Stevens, Chin-Hoh Moeng, and Peter P Sullivan. "Large-eddy simulations of radiatively driven convection: Sensitivities to the representation of small scales." In: *Journal of the atmospheric sciences* 56.23 (1999), pp. 3963–3984.

[122]   Bjorn Stevens et al. "Dynamics and chemistry of marine stratocumulus—DYCOMS-II." In: *Bulletin of the American Meteorological Society* 84.5 (2003), pp. 579–594.

[123]   Bjorn Stevens et al. "On entrainment rates in nocturnal marine stratocumulus." In: *Quarterly Journal of the Royal Meteorological Society* 129.595 (2003), pp. 3469–3493.

[124]   Bjorn Stevens et al. "Evaluation of large-eddy simulations via observations of nocturnal marine stratocumulus." In: *Monthly weather review* 133.6 (2005), pp. 1443–1462.

[125]   Bjorn Stevens et al. "Prospects for narrowing bounds on Earth's equilibrium climate sensitivity." In: *Earth's Future* 4.11 (2016), pp. 512–522.

[126]   Thomas Stocker. *Climate change 2013: the physical science basis: Working Group I contribution to the Fifth assessment report of the Intergovernmental Panel on Climate Change*. Cambridge University Press, 2014.

[127]   Roland B Stull. *An introduction to boundary layer meteorology*. Vol. 13. Springer Science & Business Media, 2012.

[128]   Max J Suarez, Akio Arakawa, and David A Randall. "The parameterization of the planetary boundary layer in the UCLA general circulation model: Formulation and results." In: *Monthly weather review* 111.11 (1983), pp. 2224–2243.

[129]   Peter P Sullivan et al. "Structure of the entrainment zone capping the convective atmospheric boundary layer." In: *Journal of the atmospheric sciences* 55.19 (1998), pp. 3042–3064.

[130]   Christopher M Taylor, Phil P Harris, and Douglas J Parker. "Impact of soil moisture on the development of a Sahelian mesoscale convective system: A case-study from the AMMA special observing period." In: *Quarterly Journal of the Royal Meteorological Society* 136.S1 (2010), pp. 456–470.

[131]   M Tiedtke. "Representation of clouds in large-scale models." In: *Monthly Weather Review* 121.11 (1993), pp. 3040–3061.

[132]   JD Turton and S Nicholls. "A study of the diurnal variation of stratocumulus using a multiple mixed layer model." In: *Quarterly Journal of the Royal Meteorological Society* 113.477 (1987), pp. 969–1009.

[133]   S Twomey. "Pollution and the planetary albedo." In: *Atmospheric Environment (1967)* 8.12 (1974), pp. 1251–1256.

[134]   J Uchida, CS Bretherton, and PN Blossey. "The sensitivity of stratocumulus-capped mixed layers to cloud droplet concentration: do LES and mixed-layer models agree?" In: *Atmospheric Chemistry and Physics* 10.9 (2010), pp. 4097–4109.

[135]   MC VanZanten et al. "Observations of drizzle in nocturnal marine stratocumulus." In: *Journal of the atmospheric sciences* 62.1 (2005), pp. 88–106.

[136]   Margreet C Vanzanten. "Radiative and evaporative cooling in the entrainment zone of stratocumulus–the role of longwave radiative cooling above cloud top." In: *Boundary-layer meteorology* 102.2 (2002), pp. 253–280.

[137]   S Wang, X Zheng, and Q Jiang. "Strongly sheared stratocumulus convection: an observationally based large-eddy simulation study." In: *Atmospheric Chemistry and Physics* 12.11 (2012), pp. 5223–5235.

[138]   Shouping Wang, Qing Wang, and Graham Feingold. "Turbulence, condensation, and liquid water transport in numerically simulated nonprecipitating stratocumulus clouds." In: *Journal of the atmospheric sciences* 60.2 (2003), pp. 262–278.

[139]   Shouping Wang, Jean-Christophe Golaz, and Qing Wang. "Effect of intense wind shear across the inversion on stratocumulus clouds." In: *Geophysical Research Letters* 35.15 (2008).

[140]   Allison A Wing and Kerry A Emanuel. "Physical mechanisms controlling self-aggregation of convection in idealized numerical modeling simulations." In: *Journal of Advances in Modeling Earth Systems* 6.1 (2014), pp. 59–74.

[141]   Robert Wood. "Stratocumulus clouds." In: *Monthly Weather Review* 140.8 (2012), pp. 2373–2423.

[142]   Scott Wunsch. "Stochastic simulations of buoyancy-reversal experiments." In: *Physics of Fluids* 15.6 (2003), pp. 1442–1456.

[143]   Takanobu Yamaguchi and David A Randall. "Large-eddy simulation of evaporatively driven entrainment in cloud-topped mixed layers." In: *Journal of the Atmospheric Sciences* 65.5 (2008), pp. 1481–1504.

[144]   Takanobu Yamaguchi and David A Randall. "Cooling of entrained parcels in a large-eddy simulation." In: *Journal of the Atmospheric Sciences* 69.3 (2012), pp. 1118–1136.

[145]   Mark D Zelinka, Chen Zhou, and Stephen A Klein. "Insights from a refined decomposition of cloud feedbacks." In: *Geophysical Research Letters* 43.17 (2016), pp. 9259–9269.

[146]   Mark D Zelinka et al. "Clearing clouds of uncertainty." In: *Nature Climate Change* 7.10 (2017), p. 674.

[147]   Minghua Zhang et al. "CGILS: Results from the first phase of an international project to understand the physical mechanisms of low cloud feedbacks in single column models." In: *Journal of Advances in Modeling Earth Systems* 5.4 (2013), pp. 826–842.

[148]   Yunyan Zhang et al. "Low-cloud fraction, lower-tropospheric stability, and large-scale divergence." In: *Journal of Climate* 22.18 (2009), pp. 4827–4844.

[149]   Ming Zhao. "An investigation of the connections among convection, clouds, and climate sensitivity in a global climate model." In: *Journal of Climate* 27.5 (2014), pp. 1845–1862.

2

WIND SHEAR EFFECTS ON RADIATIVELY AND EVAPORATIVELY DRIVEN STRATOCUMULUS TOPS

Bernhard Schulz (B.S.) and Juan Pedro Mellado (JP.M.) contributed to the paper as follows: JP.M. provided the original idea to this work and supervised the findings of this work. B.S planned and carried out the numerical simulations. B.S analyzed the data and developed the theoretical formalism that lead to the presented results. In particular, B.S derived the two critical shear velocities and performed the analysis of the entrainment rate equation. JP.M provided guidance during this process. B.S took the lead in writing the manuscript, while JP.M. provided critical feedback on the manuscript and helped to finalize this publication.

Wind-Shear Effects on Radiatively and Evaporatively Driven Stratocumulus Tops

BERNHARD SCHULZ AND JUAN PEDRO MELLADO

Max Planck Institute for Meteorology, Bundesstr. 53, 20146 Hamburg, Germany

Abstract

Direct numerical simulations resolving meter and sub-meter scales in the cloud-top region of stratocumulus are used to investigate the interactions between a mean vertical wind shear and in-cloud turbulence driven by evaporative and radiative cooling. There are three major results. First, a critical velocity jump $(\Delta u)_{\text{crit}}$ exists above which shear significantly broadens the entrainment interfacial layer (EIL), enhances cloud-top cooling, and increases the mean entrainment velocity—shear effects are negligible when the velocity jump is below $(\Delta u)_{\text{crit}}$. Second, a depletion velocity jump $(\Delta u)_{\text{dep}}$ exists above which shear-enhanced mixing reduces cloud-top radiative cooling, weakening thereby the large convective motions—shear effects remain localized within the EIL when the velocity jump is below $(\Delta u)_{\text{dep}}$. The critical velocity jump and depletion velocity jump are provided as a function of in-cloud and free tropospheric conditions and one finds $(\Delta u)_{\text{crit}} \simeq 1\,\text{m}\,\text{s}^{-1} - 4\,\text{m}\,\text{s}^{-1}$ and $(\Delta u)_{\text{dep}} \simeq 3\,\text{m}\,\text{s}^{-1} - 10\,\text{m}\,\text{s}^{-1}$ for typical subtropical conditions. Third, the individual contributions to the mean entrainment velocity from mixing, radiative cooling and evaporative cooling strongly depend on the choice of the reference height where the entrainment velocity is calculated. This result implies that the individual contributions to the mean entrainment velocity should be estimated at a comparable height while deriving entrainment-rate parametrizations. A strong shear alters substantially the magnitude and the height where these individual contributions reach their maxima, which further demonstrates the importance of shear on the dynamics of stratocumulus clouds.

1 INTRODUCTION

Wind shear in the cloud-top region can significantly alter the temporal evolution of the stratocumulus-topped boundary layer (STBL), as shown by a number of observational studies (Brost, Wyngaard, and Lenschow, 1982; Caughey, Crease, and Roach, 1982; Driedonks and Duynkerke, 1989; Faloona et al., 2005; Roode and Wang, 2007; Katzwinkel, Siebert, and Shaw, 2012; Malinowski et al., 2013; Jen-La Plante et al., 2016) and some numerical experiments (Wang, Golaz, and Wang, 2008; Wang, Zheng, and Jiang, 2012; Kopec, Malinowski, and Piotrowski, 2016). However, the aspect of meter and submeter scale mixing processes has obtained less attention, even though former studies have shown that these small-scale processes are crucial for the dynamics of the cloud in general and for shear effects in particular (Katzwinkel, Siebert, and Shaw, 2012; Malinowski et al., 2013; Mellado, 2017). Here, direct numerical simulations (DNS) are employed to explicitly resolve these small-scale processes. For a cloud top solely driven by evaporative cooling and shear, shear effects are found to enhance mixing mainly within a shallow layer (Mellado, Stevens, and Schmidt, 2014). The thickness of this layer is typically a few tens of meters or less, confirming the importance of small scale processes. However, radiative cooling has been neglected in the former study, which motivates us to investigate how

a vertical wind shear alters the dynamics of a radiatively and evaporatively driven stratocumulus cloud-top.

The first goal is to identify when shear effects become relevant. Shear can enhance the entrainment of tropospheric air (cf. studies cited above), can thicken the entrainment interfacial layer (EIL; Wang, Golaz, and Wang, 2008; Katzwinkel, Siebert, and Shaw, 2012; Jen-La Plante et al., 2016), and can change the budget of turbulent kinetic energy (TKE; Caughey, Crease, and Roach, 1982; Kopec, Malinowski, and Piotrowski, 2016; Jen-La Plante et al., 2016). Nonetheless, it remains unclear at which minimal shear strength significant changes in these quantities occur. We answer this question by deriving a critical velocity jump, below which shear effects are negligible, and a depletion velocity jump, below which shear effects remain localized within the cloud-top region and in-cloud turbulence remains unaffected.

The second goal is to quantify shear effects on the mean entrainment velocity. The magnitude of radiative and evaporative cooling drastically varies with height within a few meters, which renders shear broadening of the EIL, despite being small ($\sim 10\,\mathrm{m}$), a crucial process for understanding shear effects. Especially with respect to the mean entrainment velocity w_e—here defined as the time-rate-of-change of a reference height marking the inversion atop the cloud (Lilly, 1968)—, resolving these small-scale processes is critical, as different definitions of the reference height differ only by a few meter. Previous measurements and numerical studies (e.g. Stevens et al., 2003; Faloona et al., 2005; Gerber, Malinowski, and Jonsson, 2016) indicate that these small height differences might be crucial for entrainment velocity parameterizations. This motivates us to investigate how w_e depends on the choice of the reference height.

A related observation is that most local analyses of cloud-top entrainment assume a quasi-steady state, i.e., a state in which the in-cloud and free tropospheric conditions change slowly compared to the cloud-top processes. Nonetheless, it is known that this is not always the case (e.g., during transients) and at least for a dry atmospheric boundary layer unsteady effects are reported to affect the entrainment velocity substantially (Sullivan et al., 1998). For such an unsteady state, the shape of the mean profiles changes significantly in time and therefore different reference heights can evolve differently in time, which implies that the magnitude of w_e depends on the choice of the reference height. Still, an explicit quantification of unsteady effects is missing to the best of our knowledge. Here, we provide a first attempt to quantify unsteady effects by analyzing the corresponding term in the entrainment-rate equation.

The paper is structured as follows. Section 2 introduces the cloud-top mixing layer (CTML), defines the simulation set-up, and reviews some of the fundamental concepts and quantities needed for the analysis. Section 3 investigates how shear affects the vertical structure of the cloud top, while Section 4 investigates when shear effects start to become significant. Section 5 discusses shear effects on the entrainment velocity. Results are summarized and discussed in Section 6.

2 THE CLOUD-TOP MIXING LAYER

The cloud-top mixing layer (CTML) mimics the upper part of the STBL and consists of a region of warm and dry air, representing the free troposphere, and a region of moist, relatively cold air, representing the cloud below (cf. Fig. 1). The formulation of the CTML is identical to the one used in Lozar and Mellado (2015), where a CTML solely driven by evaporative and radiative cooling has been investigated by means of DNS. Here, we extend this work by imposing a vertical wind shear. For conciseness, the detailed formulation is presented in Appendix A, and this section only includes the description of the parameters and variables needed for the discussion of the results.
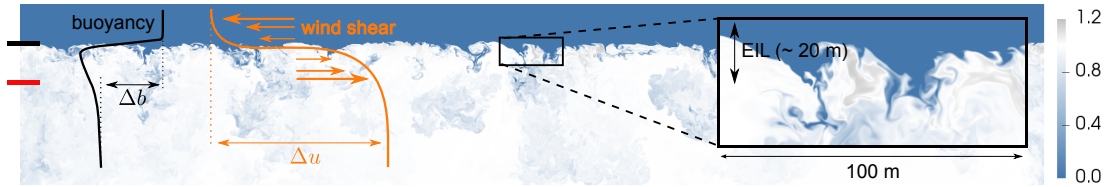
Figure 1: Vertical cross-section of the cloud-top region showing the liquid-water specific humidity field q_ℓ normalized by its in-cloud value q_ℓ^c for $S = 10$ and $Re_o = 400$ at $z_*/\lambda \simeq 16$. A sketch of the mean buoyancy profile $\langle b \rangle$ is shown in black, a sketch of mean velocity profile $\langle u \rangle$ in orange, the black horizontal line indicates the height of minimum buoyancy flux $z_{i,f}$, the red horizontal line the height of maximum buoyancy flux within the cloud (cf. Fig. 4b), and the vertical extend of the entrainment interfacial layer (EIL) is indicated in the inset (cf. Section 2.2.2). The cloud holes are associated with unsaturated air parcels from the free troposphere, which are swept deep into the cloud (Gerber et al., 2005; Gerber, Malinowski, and Jonsson, 2016).

2.1 Description of the simulations

2.1.1 Simulation parameters

Once the system has become sufficiently independent of the initial conditions, flow properties only depend on the height z, the convective length scale z_* characterizing the large-scale turbulent motions in the cloud (cf. Section 2.2.1), and six nondimensional parameters $\{Re_o, Ri_o, D, \chi_{sat}, \beta, S\}$. The reference Reynolds number, $Re_o = \lambda U_o/\nu$, and the reference Richardson number, $Ri_o = \lambda \Delta b/U_o^2$, are based on two radiative reference scales, namely, the extinction length λ and the reference buoyancy flux $B_o = R_o g/(\rho^c c_p^c T^c)$. R_o is the reference longwave radiative cooling at the cloud top [cf. Eq. (36)], ρ^c is the density of cloudy air, c_p^c is the specific heat capacity of cloudy air, T^c the temperature of cloudy air, ν is the kinematic viscosity, and the subscript o indicates reference values. Based on the former two parameters we can define a reference velocity and a reference buoyancy scale as

$$U_o = (B_o \lambda)^{1/3} \quad \text{and} \quad b_o = (B_o^2/\lambda)^{1/3}, \tag{1}$$

respectively. The buoyancy reversal parameter, $D = -b_{sat}/\Delta b$, compares the buoyancy at saturation conditions b_{sat} with the buoyancy jump across the inversion $\Delta b = b^d - b^c$, where the superscript d indicates dry conditions and the superscript c indicates cloudy conditions. Buoyancy reversal instabilities are associated with $D > 0$ (Randall, 1980; Deardorff, 1980a). The parameter χ_{sat} indicates the mixture fraction at saturation conditions, while β describes how enthalpy changes translate into buoyancy changes. The last two parameters are explained in more detail in Appendix A.

To characterize shear effects, we introduce a shear number S as

$$S = \Delta u / U_o, \tag{2}$$

where $\Delta u = ||\mathbf{u}^d - \mathbf{u}^c||$ specifies a constant vertical velocity jump across the cloud top. The vectors $\mathbf{u}^d$ and $\mathbf{u}^c$ represent the mean velocity in the dry free troposphere and in the cloud, respectively. Since we can always choose a reference frame which moves with the mean velocity $(\mathbf{u}^d + \mathbf{u}^c)/2$ and which is aligned with $\mathbf{u}^d - \mathbf{u}^c$, the parameter S is sufficient to characterize shear effects in the CTML.

2.1.2 Simulation set-up

In this work, we fix all parameters according to the first research flight (RF01) of the DYCOMS-II campaign (Stevens et al., 2003, 2005, see Table 1), and we vary the shear

Table 1: List of fixed reference parameters for RF01 of the DYCOMS-II campaign. In addition we set $\chi_{sat} = 0.09$, $\beta = 0.53$, $D = 0.031$, $T^c = 283.75$ K (cf. Section 2.1.1). The reference buoyancy flux $B_1 = \beta B_0$ accounts for condensational warming effects (cf. Section 5).

U_0	0.3 m s^{-1}	reference velocity scale
λ	15 m	extinction length
Δb	0.25 m s^{-2}	jump in buoyancy
B_0	1.9×10^{-3} m² s^{-3}	reference buoyancy flux
B_1	1.0×10^{-3} m² s^{-3}	condensation corrected reference buoyancy flux
q_ℓ^c	0.5 g kg^{-1}	cloud liquid-water specific humidity
Δq_t	-7.5 g kg^{-1}	jump in total-water specific humidity
ΔT	8.5 K	jump in temperature
Ri_0	40.2	reference Richardson number

number by varying the initial velocity jump Δu (see Table 2). Since we consider RF01 of DYCOMS-II as reference, our simulation set-up resembles subtropical clouds, which are characterized by relatively large jumps in total-water specific humidity Δq_t and temperature ΔT across the inversion. We match all parameters of the RF01 of the DYCOMS-II campaign except the Reynolds number, and therefore we need to study the dependence of our results on the Reynolds number. This dependence is discussed in Appendix B. For the Reynolds numbers reached in our simulations, the properties relevant for the discussion in this paper show only a weak dependence on the Reynolds number. This tendency towards Reynolds number similarity, which is a general characteristic of turbulent flows (Dimotakis, 2005; Mellado et al., 2018), partly justifies the extrapolation of our results to atmospheric conditions.

The grid spacing is uniform and isotropic in the region of the computational domain where the turbulent flow develops. The ratio between the grid spacing and the Kolmogorov length η is approximately 1.5, which is sufficient for the statistical properties of interest to depend less than 5% on the grid spacing, which is comparable to or less than the statistical uncertainty of the properties considered in this work (Mellado, 2010; Mellado, Stevens, and Schmidt, 2014). For the conditions of RF01 of DYCOMS-II, the corresponding grid spacings vary between 16 cm and 32 cm, depending on Re_0 (see Table 2). For the compact schemes used in these simulations, about 4 points per wavelength provide 99% accuracy in the transfer function of the derivative operator, which implies that we reach submeter scale resolution is these studies. [For comparison, second-order central schemes need about 8 points per wavelength to reach 90% accuracy, which is the motivation to employ compact schemes despite being computationally more demanding (Lele, 1992).] The size of the computational domain in the horizontal direction is $54\lambda = 810$ m, except for the low Reynolds number cases with $S = 0$ and $S = 10$ where we doubled the domain size to improve statistical convergence. In the vertical direction, we stretch the grid spacing to separate the boundaries of the computational domain while reducing the computational costs (Mellado, 2010; Mellado, Stevens, and Schmidt, 2014). The resulting vertical domain size is approximately 600 m for the cases $L_x / \lambda = 108$, and approximately 300 m − 400 m for all other cases. Further simulations details are given in Lozar and Mellado (2015), and details about the numerical algorithm can be found in Mellado and Ansorge (2012).

Table 2: Simulation details: $S = \Delta u / U_0$ defines the shear number, $Re_0 = (\lambda U_0)/\nu$ defines the reference Reynolds number, L_x is the vertical domain size, λ is the extinction length [cf. Eq. (36)], Δu is the cloud-top velocity jump [cf. Section 2.1.1], h_S is the thickness of the critical shear layer [cf. Eq. (7)], η is the Kolmogorov scale, w_* is the convective velocity scale [cf. Eq (4)], z_* is the the convective length scale [cf. Eq. (3)], h_{EIL} is the thickness of the EIL [cf. Eq. (5)], δ is the penetration depth [cf. Eq. (6)], δ_C is the convective the penetration depth [cf. Eq. (17)], $Ri_* = z_* \Delta b / w_*^2$ is the convective Richardson number, and $Ri_S = h_{EIL}/(3 h_S) = h_{EIL} \Delta b / (\Delta u)^2$ is the shear Richardson number. All time dependent variables [column 7-14] are evaluated at the final value of z_*/λ stated in the table.

S	Re_0	Grid	L_x/λ	Δu m s^{-1}	h_S m	η cm	w_* m s^{-1}	z_* m	h_{EIL} m	δ m	δ_C m	Ri_*	Ri_S
0	400	$5120^2 \times 1792$	108	0	0.0	21	0.70	250	9.5	6.3	4.9	128	–
2	400	$2560^2 \times 1408$	54	0.6	0.5	21	0.65	190	9.5	7.0	4.7	112	6.6
5	400	$2560^2 \times 1408$	54	1.5	3.1	21	0.65	200	9.8	6.3	7.1	119	1.1
10	400	$5120^2 \times 1792$	108	3.1	12.4	21	0.71	240	16.5	17.1	16.3	120	0.4
0	1200	$5120^2 \times 2048$	54	0.0	0.0	10	0.56	130	4.9	3.8	3.2	106	–
2	1200	$5120^2 \times 2048$	54	0.6	0.5	10	0.54	120	4.9	3.8	3.4	101	3.4
6	800	$5120^2 \times 2048$	54	1.8	4.5	13	0.54	120	7.1	6.3	7.0	99	0.5
10	800	$5120^2 \times 2048$	54	3.1	12.4	13	0.56	130	11.4	11.7	14.4	100	0.3

2.2 Description of the vertical structure

2.2.1 In-cloud convective scalings

The prevalence of free convection in the cloud suggests to introduce a convective length scale z_* to characterize the depth of the convective region and the size of the large-scale motions in the cloud. According to Deardorff (1980b) and following Mellado, Stevens, and Schmidt (2014), we define z_* as

$$z_* = B_{\max}^{-1} \int_{z_{-\infty}}^{z_\infty} \mathcal{H}(B) dz , \qquad (3)$$

where $\mathcal{H}$ denotes the Heaviside function, $B = \langle w'b' \rangle$ is the turbulent buoyancy flux, $B_{\max}$ is the maximum of B within the cloud, angle brackets $\langle \cdot \rangle$ indicate a horizontal average, and an apostrophe indicates the turbulent fluctuation field. The Heaviside function ensures that only the positive part of the turbulent buoyancy flux profile, which generates turbulence, is retained. We will show in Fig. 9 that the height of zero buoyancy flux $z_{i,o}$ is located near the height of zero mean buoyancy $z_{i,n}$, and thus z_* is mainly associated with a negatively buoyant region.

A measure of the intensity of the in-cloud turbulence is provided by the convective velocity scale (Deardorff, 1970)

$$w_* = (B_{\max} z_*)^{1/3} , \qquad (4)$$

and indeed the maximum of the turbulent kinetic energy (TKE) within the cloud, $e_{\max}$, follows the scaling law $2 e_{\max}/w_*^2 \simeq 1$ for $z_*/\lambda > 10$ (not shown). Note that our definition of w_* is smaller by a factor of $2.5^{1/3} \simeq 1.4$ compared to previous work that considers the whole STBL (Deardorff, 1980b; Wood, 2012). The reason is that the buoyancy flux in the CTML set-up does not have the linear vertical variation characteristic of the subcloud layer in the STBL, which justifies the factor 2.5.

Due to a continuous cloud-top cooling, the turbulent buoyancy flux increases with time and hence z_* increases with time. We can use this relationship between time and
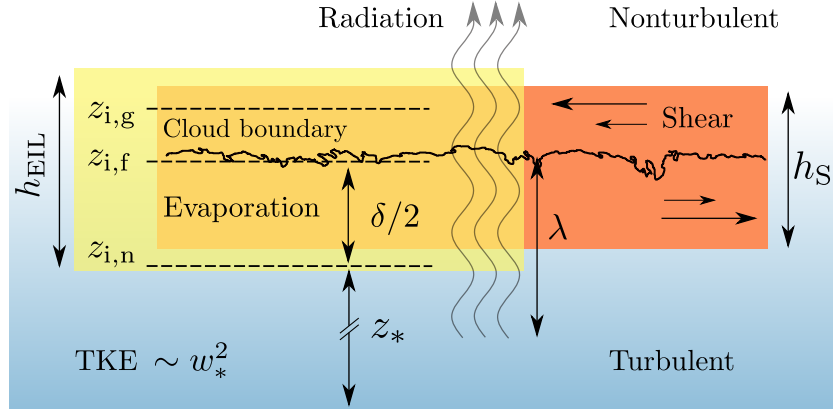
Figure 2: Sketch of the CTML. Red indicates the critical shear layer and yellow indicates the EIL, which are of comparable thickness for the case $S = 10$ sketched here. The cloud top is cooled by radiation over a length scale λ, in-cloud turbulence is characterized by a convective length scale z_* and a convective velocity scale w_*. The horizontal dashed lines indicate, respectively, the height of zero mean buoyancy $z_{i,n}$, the height of minimum turbulent buoyancy flux $z_{i,f}$, and the height of the maximum gradient of the mean buoyancy $z_{i,g}$ (cf. Section 5), while the jagged black line indicates the cloud boundary. In-cloud turbulent motions penetrate into the stably stratified cloud top and thereby set a penetration depth δ.

z_* to express the evolution of the system in terms of the nondimensional variable z_*/λ. Introducing this variable has the advantage that z_*/λ represents the scale separation between the integral scale of the in-cloud turbulence and the scale at which the radiative forcing is introduced. In addition, z_*/λ represents the intensity of the in-cloud turbulence, according to Eq. (4). We reach $z_*/\lambda \simeq 16$ in our simulations, which is within the range of $z_*/\lambda \simeq 3 - 80$ reported in Deardorff (1981). To improve statistical convergence, the results are averaged in time over a period of $z_*/\lambda = 1$, which corresponds to approximately $5 - 7$ eddy turnover times $t_* = z_*/w_*$.

2.2.2 *The entrainment interfacial layer*

In general terms, the EIL refers to the layer where the entrainment of dry and warm tropospheric air takes place, and thus represents a transition layer between the cloud and the free troposphere. Therefore, the EIL is characterized by strong vertical variations of temperature, specific humidity, mean vertical velocity, and buoyancy. We hence define the EIL thickness as

$$h_{\text{EIL}} = z_{0.9\Delta b} - z_{i,n} \,, \tag{5}$$

where $z_{i,n}$ is the height of zero mean buoyancy, and $z_{0.9\Delta b}$ denotes the height where the mean buoyancy $\langle b \rangle$ has increased by 90% of Δb. According to this definition, the EIL is stably stratified, contains the cloud-boundary, and the turbulent/non-turbulent interface (see Fig. 2).

For weak enough shear, the EIL dynamics is determined by the in-cloud turbulent motions penetrating into the free troposphere. This processes is characterized by the penetration depth, here defined as

$$\delta = 2(z_{i,f} - z_{i,n}) \,, \tag{6}$$

where $z_{i,f}$ denotes the height of minimum mean buoyancy flux. Previous work on shear-free conditions has shown that the thickness associated with the evaporative cooling caused by diffusion, h_{diff}, is comparable to h_{EIL} for low-to-moderate Reynolds numbers

(Mellado, 2010; Lozar and Mellado, 2015). For the sheared configurations considered in this study this is also the case and we find $h_{\mathrm{diff}}/h_{\mathrm{EIL}} = 0.5 - 1.0$, which indicates that h_{diff} needs to be retained in the scaling law of h_{EIL}. Figure 3 demonstrates that h_{EIL} is scaled by $\delta + h_{\mathrm{diff}}$.

For strong enough shear, however, locally generated turbulence enhances mixing, which can thicken the EIL substantially. This shear effect can be characterized by the reference length (Mellado, Stevens, and Schmidt, 2014)

$$ h_{\mathrm{S}} = \frac{(\Delta u)^2}{3\Delta b} , \tag{7} $$

which is henceforth referred to as critical shear layer thickness, where the subscript S indicates 'shear'. The factor $1/3$ in h_{S} is well established ($\pm 15\%$) from laboratory and numerical experiments of stably stratified shear layers (Smyth and Moum, 2000; Brucker and Sarkar, 2007) and from observations and numerical experiments of cloud-free sheared convective boundary layers (Mahrt and Lenschow, 1976; Fedorovich and Conzemius, 2008), and can be associated with a critical value of the shear Richardson number $Ri_{\mathrm{S}} = h_{\mathrm{EIL}}\Delta b/(\Delta u)^2$. A strong shear can broaden the EIL sufficiently for the EIL thickness, h_{EIL}, to be well approximated by the critical shear layer thickness, h_{S}. This is shown in Fig. 3 for the case $S = 10$, where we still need to add the diffusion correction h_{diff} to account for the low-Reynolds-number effect, as we did in δ.

The physical interpretation of the critical shear layer thickness h_{S} is rationalized as follows. Given a stably stratified shear layer characterized by a buoyancy jump Δb and a velocity jump Δu, if the initial shear layer is thin enough, Kelvin-Helmholtz instabilities will cause an overturning of the stably stratified fluid and a thickening of the shear layer. As the shear layer thickens, overturning the fluid becomes more difficult because the vertical displacement increases whereas the available kinetic energy, proportional to $(\Delta u)^2$, remains constant. Once the shear layer has grown to its critical thickness h_{S}, the available kinetic energy is insufficient to overturn the fluid and turbulence decays.

We emphasize that h_{S} is an average quantity and there is a range of smaller motions in the EIL that locally can have a gradient Richardson number below $1/3$ (J Kurowski, P Malinowski, and W Grabowski, 2009; Malinowski et al., 2013). In particular, in-cloud turbulent motions penetrate into the stably stratified EIL, which locally thins the inversion and creates further shear instabilities that increase the shear layer thickness towards its critical value h_{S}. In absence of this thinning process, shear-generated turbulence would decay once the EIL reaches the critical thickness h_{S}. This dynamical equilibrium between penetrating thermals and shear instability permanently maintains mixing within the cloud-top region, despite the mean Richardson number being near the critical value for stability (Mahrt and Lenschow, 1976; Fedorovich and Conzemius, 2008; Howland, Taylor, and Caulfield, 2018).

In this study, we consider shear-free conditions as reference case and increase the cloud-top velocity jump to study weak shear conditions with $\Delta u = 1.5\,\mathrm{m\,s^{-1}}$ and $h_{\mathrm{S}} \ll h_{\mathrm{EIL}}$, and strong shear conditions with $\Delta u = 3.1\,\mathrm{m\,s^{-1}}$ and $h_{\mathrm{EIL}} \simeq h_{\mathrm{S}}$. Note that even for strong shear conditions the penetration depth of in-cloud turbulence, δ, is still comparable with h_{EIL} (see Table 2 and Fig. 3). The limit of very strong shear where $h_{\mathrm{EIL}} \simeq h_{\mathrm{S}}$ is much larger than the penetration depth of in-cloud motions, considered in Mellado, Stevens, and Schmidt (2014) for the solely evaporatively driven case, is not investigated here.

Finally, we note that our definition of the EIL, Eq. (5), follows the definition by Caughey, Crease, and Roach (1982) as the layer containing most of the temperature jump (buoyancy in our case). This definition approximately coincides with the region of negative buoyancy flux, which is often referred to as entrainment zone in cloud-free boundary layers (e.g. Fedorovich and Conzemius, 2008). This similarity proved convenient to use results from the study of shear effects in cloud-free conditions, in
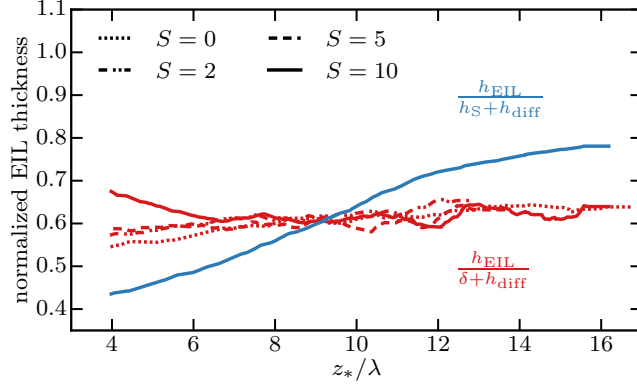
Figure 3: Time evolution of the EIL thickness h_{EIL} normalized by $\delta + h_{diff}$ (red) and $h_S + h_{diff}$ (blue), respectively, for cases $Re_0 = 400$. The penetration depth δ is defined in Eq. (6) and the critical shear layer thickness h_S in Eq. (7). The diffusive thickness h_{diff} is discussed in Section 4.1.

particular, the relevance of the critical shear layer and its thickness h_S. However, this definition of EIL differs from the one proposed by Malinowski et al. (2013), especially in the definition of the lower boundary of the EIL, which has to be taken into account when comparing results. In Malinowski et al. (2013), the lower boundary of the EIL is defined as the height where the square of the horizontal wind shear reaches 90% of its maximum value. In our definition of the EIL, this height roughly coincides with the height of minimum turbulent buoyancy flux $z_{i,f}$, which is approximately located in the center of the EIL (cf. Fig. 4).

3   VERTICAL EXTEND OF WIND-SHEAR EFFECTS

This section studies what is the vertical extent of wind-shear effects. The first part of the analysis is based on the TKE evolution equation, which is given by

$$\frac{\partial e}{\partial t} = -\frac{\partial T}{\partial z} + P + B - \varepsilon \, , \tag{8}$$

where $e = \langle u_i' u_i' \rangle /2$ is the turbulent kinetic energy, $T = \langle w' u_i' u_i' /2 + p' w' - u_i' \tau_{iz}' \rangle$ the vertical turbulent flux, $P = -\langle u' w' \rangle \partial_z \langle u \rangle$ the shear-production rate, $B = \langle w' b' \rangle$ the turbulent buoyancy flux, $\varepsilon = \langle \tau_{i,j}' u_{i,j}' \rangle$ the viscous dissipation term, and $\tau_{ij}' = \nu (\partial_j u_i' + \partial_i u_j')$ the fluctuating part of the viscous stress tensor.

Based on the TKE budget in the EIL, we can distinguish between two limiting regimes (cf. Fig. 4a). For $S = 0$, the shear-production term is zero and the turbulent transport term $-\partial_z T$ is the only source of TKE in the EIL, where part of the TKE is dissipated and part is used to entrain warm and dry air from above, as indicated by the negative turbulent buoyancy flux. For $S = 10$, the shear production term is the dominating source of TKE in the EIL, where part of the TKE is dissipated, part is redistributed by the transport term, and part is used to enhance the entrainment of tropospheric air. These observations are in general agreement with previous work (e.g. Kopec, Malinowski, and Piotrowski, 2016; Jen-La Plante et al., 2016). In addition it is noteworthy that for $S = 10$ the input of TKE is strong enough to generate an area within the EIL where the transport term turns negative, indicating an export of TKE. By increasing the shear strength, we hence change the ratio between the turbulent-transport term and the shear-production term, and the system transitions from a transport dominated regime within the EIL to a shear dominated regime.

In contrast, within the cloud region below the EIL, the TKE and the terms in its evolution equation remain approximately the same for different shear numbers (cf.
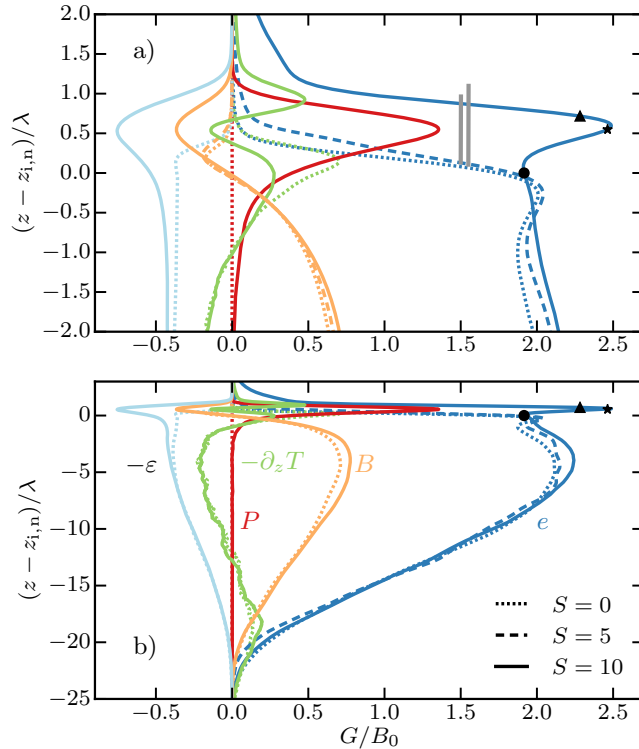
Figure 4: a) Vertical profile of TKE budget terms at $z_*/\lambda \simeq 13$ for $Re_0 = 400$ (a) in the EIL, and (b) in the complete cloud. Different colors indicate different terms G of the TKE budget [cf. Eq. (8)]. The triangle indicates the height of maximum gradient of the mean buoyancy profile $z_{i,g}$, the star the height of minimum buoyancy flux $z_{i,f}$, and the circle the height of zero buoyancy $z_{i,n}$. The (left) short gray vertical line indicates the critical shear layer with a thickness h_S, while the (right) long vertical line indicates the penetration depth with a thickness δ (cf. Table 2, $S = 10$).

Fig. 4b). This independence of in-cloud properties to the strength of cloud-top wind shear is further demonstrated in Fig. 5, where the temporal evolution of the maximum TKE within the cloud is approximately independent of S, whereas the maximum within the EIL increases by about 60% when increasing the shear strength from $S = 0$ to $S = 10$. Hence, wind-shear effects remain localized within the EIL.

Although shear effects remain localized within the EIL for all investigated cloud-top velocity jumps, shear can affect large-scale properties if Δu is large enough for the critical shear layer thickness h_S to become comparable to the cloud thickness H. In this condition, shear-enhanced mixing depletes the cloud sufficiently to reduce the net radiative cooling, thus weakening turbulence and favoring a decoupling of the STBL (Wang, Golaz, and Wang, 2008; Wang, Zheng, and Jiang, 2012; Kopec, Malinowski, and Piotrowski, 2016). In what follows, we estimate the depletion velocity jump $(\Delta u)_{\text{dep}}$ at which this shear effect occurs.

The radiative flux difference between cloud top and cloud base is $R_0(1 - \alpha)$, where

$$\alpha = \exp[-H/(2\lambda)] . \tag{9}$$

This expression follows from Eq. (36) and the assumption of an adiabatic liquid lapse-rate in the cloud. If the radiative extinction length, λ, is much smaller than the cloud thickness, H, then $\alpha \ll 1$ and the radiative flux difference between the cloud interior and the free troposphere is R_0. How much can shear reduce the liquid-water specific humidity q_ℓ in the cloud-top region for this radiative flux difference to remain approximately R_0?

Let us consider that shear enhanced mixing causes the evaporation of a cloud layer of thickness d at the top, reducing the cloud thickness from the initial value H to $H - d$ (cf.
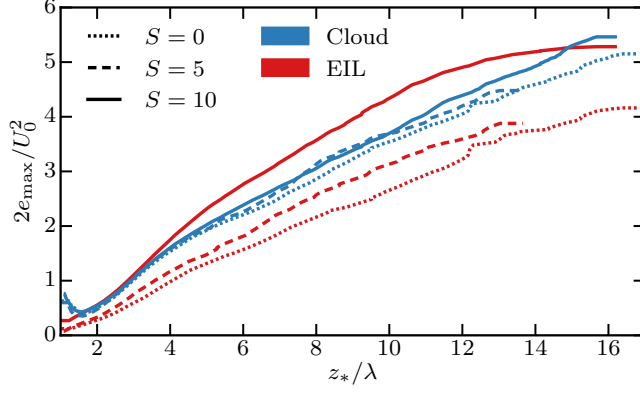
Figure 5: Temporal evolution of the normalized maximum TKE within the cloud (blue) and within the EIL (red) for $Re_0 = 400$.

Fig. 6). This process reduces the maximum liquid-water specific humidity at the cloud top from the initial value $q_{\ell,o}$ to $q_{\ell,o}(H - d)/H$, if an adiabatic liquid lapse-rate is assumed. This reduction increases the radiative extinction length from λ to $\lambda H/(H - d)$ because the radiative extinction length is inversely proportional to the maximum liquid-water specific humidity (Larson, Kotenberg, and Wood, 2007; Wood, 2012; Mellado, 2017). For this new, partially depleted cloud, the radiative flux difference between cloud top and cloud base is $R_0(1 - \alpha_{\text{dep}})$, where

$$\alpha_{\text{dep}} = \exp\left[-(H - d)^2/(2\lambda H)\right] . \tag{10}$$

Since $\alpha_{\text{dep}} < \alpha$, the depleted cloud has a smaller radiative flux difference between the cloud interior and the free troposphere. However, as long as $\alpha_{\text{dep}} \ll 1$, the radiative difference remains approximately R_0 and the radiative forcing of the boundary-layer turbulence remains approximately the same.

In order to relate d to the velocity jump Δu, we assume that d is proportional to the thickness of the critical shear layer h_S. As a first approximation, we assume that the critical shear layer is centered at the height of minimum turbulent buoyancy flux $z_{i,f}$ and mixes and evaporates a cloud layer of a thickness $d \simeq h_S/2$. Substituting this relation into Eq. (10) and solving for h_S yields

$$h_{S,\text{dep}} = 2\left[H - \sqrt{2\lambda H \ln(\alpha_{\text{dep}}^{-1})}\right] \tag{11}$$

as an estimate for the critical shear layer thickness that is necessary to obtain a reduction α_{dep} of the radiative flux difference between the cloud top and the cloud base. The corresponding depletion velocity jump follows from Eq. (7) and is given by

$$(\Delta u)_{\text{dep}} \simeq (3\Delta b h_{S,\text{dep}})^{1/2} . \tag{12}$$

Therefore, only a strong wind shear with $\Delta u > (\Delta u)_{\text{dep}}$ can deplete the cloud sufficiently to change the net radiative cooling. Equation (12) shows that $(\Delta u)_{\text{dep}}$ increases with increasing inversion strength, i.e., when the buoyancy jump Δb increases. This dependence seems reasonable since increasing the inversion strength hinders entrainment. Equation (12) further shows that $(\Delta u)_{\text{dep}}$ increases with the cloud thickness. This result seems also reasonable, increasing the cloud thickness implies that cloud-top depletion needs to extend over a thicker layer to change the net radiative cooling of the cloud. Last, we note that the proportionality $d \simeq h_S/2$ used in the derivation of Eq. (12) may depend on the thermodynamic conditions. It is for example expected that moistening the free troposphere increases $(\Delta u)_{\text{dep}}$ by weakening evaporation. Hence, further assessment
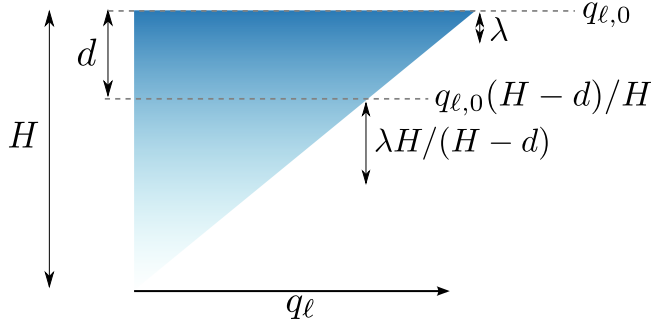
Figure 6: The liquid-water specific humidity q_ℓ varies linearly with height over the cloud thickness H, shear depletes a layer of thickness d, and radiation is associated with a length scale λ.

of the dependence of $(\Delta u)_{\text{dep}}$ on the thermodynamic conditions is necessary. However, as discuss in the following paragraph, Eq. (12) provides a leading-order estimate for the effect of shear broadening on the radiative-cooling forcing that is consistent with observations.

For the case RF01 of the DYCOMS-II field campaign, we find $(\Delta u)_{\text{dep}} \simeq 10\,\text{m}\,\text{s}^{-1}$, where we used $H = 200\,\text{m}$, $\lambda = 15\,\text{m}$, $\Delta b = 0.25\,\text{m}\,\text{s}^{-2}$, and an arbitrary threshold of $\alpha_{\text{dep}} = 0.05$, i.e., a 5% reduction of the net radiative flux difference across the cloud-top region compared to the no shear case. This result is consistent with field measurements reporting a compact cloud layer and a strong radiative forcing in that case, since the velocity jump across the cloud top is only $\simeq 1\,\text{m}\,\text{s}^{-1}$. We can generalize this result and consider an interval of cloud thickness between 100 m and 200 m, which yields an interval of depletion velocity jump $(\Delta u)_{\text{dep}} \simeq 3\,\text{m}\,\text{s}^{-1} - 10\,\text{m}\,\text{s}^{-1}$. This range seems consistent with measurements from different field campaigns, which report velocity jumps up to $4\,\text{m}\,\text{s}^{-1} - 10\,\text{m}\,\text{s}^{-1}$ for compact clouds, but not much higher (Brost, Wyngaard, and Lenschow, 1982; Nicholls and Leighton, 1986; Faloona et al., 2005; Roode and Wang, 2007; Katzwinkel, Siebert, and Shaw, 2012; Malinowski et al., 2013). However, the range of $(\Delta u)_{\text{dep}}$ is partly in disagreement with previous numerical experiments (Wang, Golaz, and Wang, 2008; Wang, Zheng, and Jiang, 2012; Kopec, Malinowski, and Piotrowski, 2016), where cloud-top depletion and decoupling of initially well mixed STBLs is observed for smaller velocity jumps. This disagreement might be partly caused by the excessive mixing associated with the subgrid models used in those large-eddy simulations. Other numerical artifacts like numerical diffusion and effects of the grid-box aspect ratio could further contribute to this disagreement (Stevens, Moeng, and Sullivan, 1999; Pedersen, Malinowski, and Grabowski, 2016; Pedersen et al., 2018).

4 STRONG AND WEAK SHEAR REGIMES

The previous section (e.g. Fig. 4) indicates that shear effects become relevant for shear numbers larger than $S \simeq 5 - 10$, which indicates a transition between the weak shear regime and the strong shear regime described in Section. 2.2.2.2. This section rationalizes this behavior in terms of two length scales and provides an analytic expression for the critical velocity jump $(\Delta u)_{\text{crit}}$ beyond which shear effects in the EIL are significant.

4.1 *The penetration depth*

Considerations of kinetic and potential energy within the EIL allow us to derive a scaling law for the penetration depth δ, defined by Eq. (6), as follows. To a first approximation air parcels with a kinetic energy E_{kin} can penetrate a distance δ into the EIL until all their kinetic energy is converted into a potential energy E_{pot}. As a first approximation, the
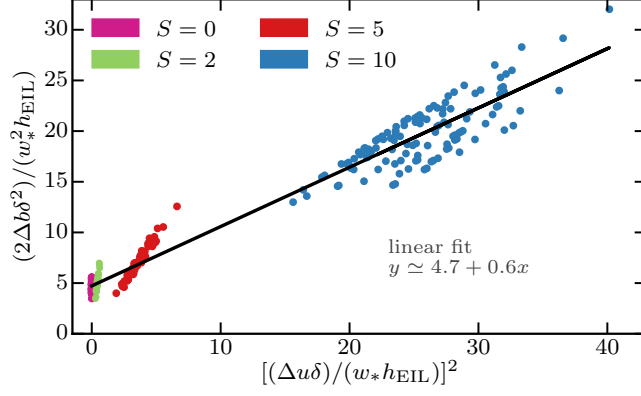
Figure 7: Linear fit of Eq. (15), where $h_{EIL} = z_{0.9\Delta b} - z_{i,n}$ is the EIL thickness, and $\delta = 2(z_{i,f} - z_{i,n})$ is the penetration depth (cf. Section 2.2.2). Data for the fit is limited to the regime $z_*/\lambda > 10$ and $Re_0 = 400$.

kinetic energy of an air parcel within the EIL is estimated by the sum of a kinetic energy associated with in-cloud convective motions—characterized by w_*—and a kinetic energy associated with the shear production in the EIL—characterized by Δu. Hence, we write

$$E_{kin} \simeq \frac{1}{2}\left[\alpha_1 w_*^2 + \alpha_2 \left(\frac{\Delta u \delta}{h_{EIL}}\right)^2\right] , \qquad (13)$$

where the ratio $\Delta u / h_{EIL}$ represents the gradient of the horizontal mean velocity within the EIL. Likewise, the potential energy at a height δ within the EIL is given by

$$E_{pot} \simeq \delta \frac{\Delta b \delta}{h_{EIL}} , \qquad (14)$$

where the ratio $\Delta b / h_{EIL}$ characterizes the gradient of the mean buoyancy profile within the EIL. The height that parcels can penetrate into the EIL is hence implicitly given by the energy balance $E_{kin} \simeq E_{pot}$, which allows us to write

$$\frac{2\Delta b \delta^2}{w_*^2 h_{EIL}} \simeq \alpha_1 + \alpha_2 \left(\frac{\Delta u \delta}{w_* h_{EIL}}\right)^2 . \qquad (15)$$

A similar equation is analyzed in Haman (2009) for shear-free conditions. Figure 7 supports this linear relationship, and a linear regression to the data provides the parameters $\alpha_1 \simeq 5.0$ and $\alpha_2 \simeq 0.6$.

In summary, Eq. (15) yields the following expression for the penetration depth δ:

$$\delta \simeq \left(\frac{\alpha_1 w_*^2 h_{EIL}}{2\Delta b - \alpha_2 (\Delta u)^2 h_{EIL}^{-1}}\right)^{1/2} . \qquad (16)$$

Two simplified expressions of Eq. (16) are obtained by introducing different scalings for h_{EIL}. For a weak enough shear, in-cloud turbulence dominates mixing in the EIL, and we can estimate $h_{EIL} \simeq \delta$ for large enough Reynolds numbers, as discussed in Section 2.2.2. In this case, Eq. (16) simplifies to

$$\delta_C = \alpha_1 \frac{w_*^2}{2\Delta b} + \alpha_2 \frac{(\Delta u)^2}{2\Delta b} , \qquad (17)$$

where the subscript C refers to 'convection'.

For a strong enough shear, we can alternatively apply the scaling $h_{EIL} \simeq h_S$, as explained in Section 2.2.2. In this case, Eq. (16) simplifies to

$$\delta_S = \sqrt{\frac{\alpha_1}{3(2 - 3\alpha_2)}} \frac{\Delta u w_*}{\Delta b} , \qquad (18)$$
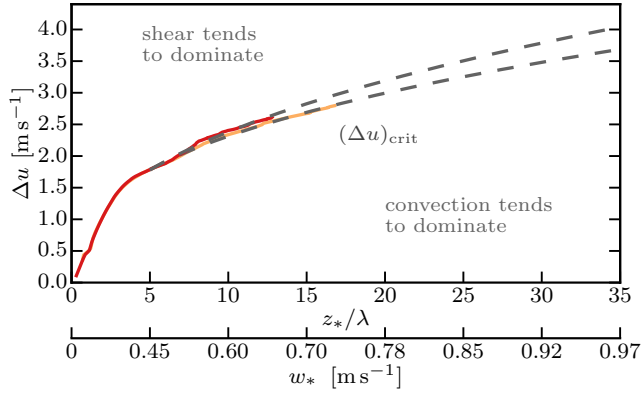
Figure 8: Critical velocity jump $(\Delta u)_{\text{crit}}$ as function of the convective length scale z_*/λ. The second horizontal axis expresses this variable in terms of the convective velocity scale w_* by means of Eq. (4) for RF01 of DYCOMS-II. The red and orange line indicate simulation results for $S = 10$ (red) and $S = 0$ (orange) respectively, for cases $Re_0 = 400$. The dashed gray is an extrapolation of w_* using an exponential fit to w_* as a function of z_*/λ. Lines of $(\Delta u)_{\text{crit}}$ for different shear numbers are close to each other, once more showing that w_* is approximately independent of S. The three blue stars indicate the velocity jumps associated with $S = 2$, $S = 5$, and $S = 10$ respectively (cf. Table 2).

where the subscript S refers to 'shear'. This scaling is consistent with the definition of the penetration depth by Eq. (A1) in Mellado, Stevens, and Schmidt (2014), which is obtained in the limit of a very strong shear, i.e., $h_{\text{EIL}} \gg \delta$. We find $\delta_S/\delta_C \simeq 1.5$ for $S = 10$, which is reasonable since h_{EIL} is equally well scaled by $\delta + h_{\text{diff}}$ and $h_S + h_{\text{diff}}$ for $S = 10$ (cf. Section 2.2.2). We hence conclude that convection and shear are comparably important for $S = 10$.

4.2 *The critical velocity jump*

Shear effects are negligible for $S \leq 5$ and in-cloud turbulent convection penetrating into the EIL dominates the EIL dynamics (cf. Section 3). In this regime, the EIL thickness h_{EIL} is well characterized by the penetration depth δ, namely, $h_{\text{EIL}} \simeq 0.6\delta$ when we extrapolate the result in Fig. 3 to high Reynolds numbers. As shear intensifies, shear and convection become similarly important for $S = 10$, which corresponds to the condition $h_{\text{EIL}} \simeq 0.8h_S$ according to Fig. 3. Therefore, it seems reasonable to define a critical penetration depth δ_{crit} by the condition

$$h_S = \alpha_3 \delta_{\text{crit}} , \tag{19}$$

with $\alpha_3 \simeq 0.6/0.8 \simeq 0.7$. Substituting h_S by Eq. (7) and $\delta_{\text{crit}} \simeq \delta_C$ by Eq. (17) into Eq. (19) yields the following expression for the critical velocity jump

$$(\Delta u)_{\text{crit}} \simeq \sqrt{\frac{3\alpha_1}{2\alpha_3^{-1} - 3\alpha_2}} w_* . \tag{20}$$

Shear effects become relevant for shear velocities larger than this critical value, which allows us to distinguish a continuous transition across three regimes as we increase the velocity jump: For $\Delta u \ll (\Delta u)_{\text{crit}}$ convection dominates and shear effects are negligible, for $\Delta u \simeq (\Delta u)_{\text{crit}}$ convection and shear are equally important, and for $\Delta u \gg (\Delta u)_{\text{crit}}$ shear dominates. According to Fig. 3 and Fig. 7, respectively, we set $\alpha_1 \simeq 5.0$, $\alpha_2 \simeq 0.6$, and $\alpha_3 \simeq 0.7$, which finally results in

$$(\Delta u)_{\text{crit}} \simeq 4w_* . \tag{21}$$

13

Typical values of $(\Delta u)_{\text{crit}}$ are given in Fig. 8, where the range of $w_* \simeq 0.2\,\text{m\,s}^{-1} - 0.9\,\text{m\,s}^{-1}$ is chosen according to Wood (2012). Figure 8 shows that only the case $S = 10$ exceeds the critical velocity jump, which is consistent with the observation that the shear Richardson number Ri_S is significantly smaller than unity for this case (cf. Table 2).

It is remarkable that, according to Eq. (21), $(\Delta u)_{\text{crit}}$ is independent of the inversion strength as measured by the buoyancy jump Δb. The reason is that h_S and δ are both inversely proportional to Δb, which shows that effects of Δb cancel each other to leading order. Still, the convective velocity scale w_* can depend on the thermodynamic parameters $\{D, \chi, \beta\}$, where the dependence on D introduces implicitly a dependence on Δb; these potential effects need to be further investigated. The dependence of Eq. (21) on the Reynolds number also needs to be further assessed. However, the coefficients α_1 and α_2 change by less than 30% and 15%, respectively, when increasing the Reynolds number up to a factor of 3. This implies that $(\Delta u)_{\text{crit}}$ changes by 10% or less, which provides certain support to extrapolate our results to atmospheric conditions.

5 WIND-SHEAR EFFECTS ON THE ENTRAINMENT VELOCITY

Following Lilly (1968), we define the mean entrainment velocity as

$$w_{\text{e}} = \frac{\mathrm{d}z_{\text{i}}}{\mathrm{d}t} - \langle w \rangle_{z_{\text{i}}} \, , \tag{22}$$

where $z_{\text{i}}(t)$ is a reference height marking the cloud-top region, and $\langle w \rangle_{z_{\text{i}}}$ is a mean vertical velocity at z_{i}. Mixed-layer models of the STBL use the same definition of mean entrainment velocity (e.g. Stevens, 2002; De Roode et al., 2014a), and hence our results can be easily interpreted in such a mixed-layer framework. Henceforth, a subscript z_{i} indicates that the corresponding quantity is evaluated at z_{i}. Common choices of reference heights are the height of maximum gradient of the mean buoyancy, $z_{\text{i,g}}$, which sits on top of the height of minimum turbulent buoyancy flux, $z_{\text{i,f}}$, which sits on top of the height of zero mean buoyancy, $z_{\text{i,n}}$, which sits on top of the height of zero turbulent buoyancy flux, $z_{\text{i,o}}$. Fig. 9 shows that for RF01 of DYCOMS-II those different heights are only separated by a few meters. Alternative reference heights have also been proposed, e.g., by Malinowski et al. (2013). Hence, in this section, we study how the entrainment velocity depends on an arbitrary definition of a reference height $z_{\text{i}}(t)$ and how wind shear affects this dependence.

To analyze the dependence of w_{e} on wind shear and on the choice of the reference height z_{i}, we use the entrainment-rate equation (Mellado, 2017; Mellado et al., 2018). The starting point for deriving the entrainment-rate equation is the buoyancy evolution equation,

$$D_t b = \kappa_T \nabla^2 b - s^{\text{rad}} - s^{\text{eva}} \, , \tag{23}$$

where s^{rad} and s^{eva} denote the radiative and evaporative source terms, respectively (cf. Appendix A). Integrating Eq. (23) from an arbitrary height $z = z_{\text{i}}$ upwards yields the entrainment-rate equation

$$w_{\text{e}} = w_{\text{e}}^{\text{mix}} + w_{\text{e}}^{\text{rad}} + w_{\text{e}}^{\text{eva}} + w_{\text{e}}^{\text{def}} \, , \tag{24}$$

where $w_{\text{e}}^{\text{mix}} = w_{\text{e}}^{\text{tur}} + w_{\text{e}}^{\text{mol}}$ and

$$w_{\text{e}}^{\text{tur}}(b^{\text{d}} - \langle b \rangle_{z_{\text{i}}}) = - \langle w'b' \rangle_{z_{\text{i}}} \, , \tag{25}$$

$$w_{\text{e}}^{\text{mol}}(b^{\text{d}} - \langle b \rangle_{z_{\text{i}}}) = \kappa_T \partial_z \langle b \rangle_{z_{\text{i}}} \, , \tag{26}$$

$$w_{\text{e}}^{\text{rad}}(b^{\text{d}} - \langle b \rangle_{z_{\text{i}}}) = \beta g (c_p^{\text{c}} T^{\text{c}})^{-1}(R_0 - \langle R \rangle_{z_{\text{i}}}) \, , \tag{27}$$

$$w_{\text{e}}^{\text{eva}}(b^{\text{d}} - \langle b \rangle_{z_{\text{i}}}) = E_0 - \langle E \rangle_{z_{\text{i}}} \, , \tag{28}$$

$$w_{\text{e}}^{\text{def}}(b^{\text{d}} - \langle b \rangle_{z_{\text{i}}}) = -\frac{\mathrm{d}}{\mathrm{d}t} \int_{z_{\text{i}}}^{z_{\infty}} (b^{\text{d}} - \langle b \rangle (z)) \mathrm{d}z \, . \tag{29}$$
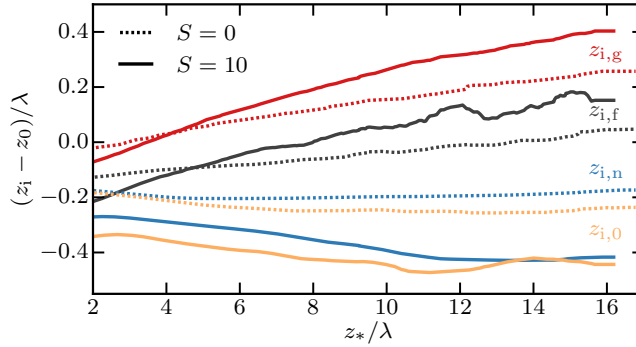
Figure 9: Temporal evolution of different reference heights for $Re_0 = 400$. The height of the maximum slope of the mean buoyancy profile $z_{i,g}$ is shown in red, the height of the minimum of the mean buoyancy flux $z_{i,f}$ in black, the height of zero mean buoyancy $z_{i,n}$ in blue, and the height of zero buoyancy flux $z_{i,0}$ in orange. The reference height z_0 corresponds to $z_{i,g}$ at time zero.

The radiative-cooling contribution w_e^{rad} is set by the difference between the net radiative flux above the cloud, R_0, and the net radiative flux evaluated at z_i, $\langle R \rangle_{z_i}$. Equivalently, the evaporative cooling contribution w_e^{eva} is set by the difference between the integrated evaporative cooling of the cloud, $E_0 = \langle E \rangle_{z_\infty}$, and the integrated evaporative cooling at z_i, $\langle E \rangle_{z_i}$, which is given by

$$\langle E \rangle_{z_i} = \int_{z_{-\infty}}^{z_i} \langle s^{eva} \rangle \, dz \ . \tag{30}$$

Finally, w_e^{def} quantifies deformation effects of the mean buoyancy profile $\langle b \rangle$, i.e., how temporal changes in the shape of the mean buoyancy profile affect w_e.

Figure 10 shows that the radiative and evaporative cooling rate strongly vary with height. Radiative cooling peaks at $\simeq 5\,\mathrm{K\,h^{-1}}$ slightly below $z_{i,n}$—outside the EIL—and decays within a few tens of meters inside the cloud. This behavior is consistent with the vertical profiles of radiative cooling reported in previous work (Stevens et al., 2003; Yamaguchi and Randall, 2012; Gerber et al., 2014). In contrast, evaporative cooling peaks near $z_{i,f}$—within the EIL—and decays more rapidly. This behavior qualitatively agrees with previous work (e.g., Yamaguchi and Randall, 2012; Wood, 2012; Gerber, Malinowski, and Jonsson, 2016). However, the assumption of phase equilibrium (saturation adjustment) often used in numerical simulations might overemphasize this narrow shape of the evaporative cooling profiles, but whether this effect is significant remains to be investigated. Either way, a quantitative comparison with previous work is difficult because, to the best of our knowledge, previous LES studies and measurement campaigns have not provided the profile of evaporative cooling for DYCOMS-II like conditions. Nonetheless, we can gain confidence in our results by noting that the total evaporative cooling, E_0, is related analytically to the mean entrainment velocity according to $E_0 = (D/\chi_{sat} + 1)w_e\Delta b$ (Lozar and Mellado, 2015; Mellado, 2017). This relationship implies that evaporative cooling rates are directly proportional to entrainment rates (for a given set of thermodynamic parameters) and correctly simulating the mean entrainment velocity w_e therefore ensures realistic values of total evaporative cooling E_0. For the investigated case RF01 of the DYCOMS-II campaign we obtain a quasi-steady entrainment velocity of $w_e^{tur} + w_e^{rad} + w_e^{eva} \simeq 4.5\,\mathrm{mm\,s^{-1}}$ for the no shear case, which is commensurate with the range of $w_e \simeq 3.9\,\mathrm{mm\,s^{-1}} - 4.7\,\mathrm{mm\,s^{-1}}$ reported in Stevens et al. (2003) and Faloona et al. (2005).

As a consequence of the rapid variation with height of cloud-top properties, the different contributions to w_e vary strongly with height in the EIL and hence Eq. (24) depends strongly on the choice of the reference height z_i. The contributions w_e^{eva} and
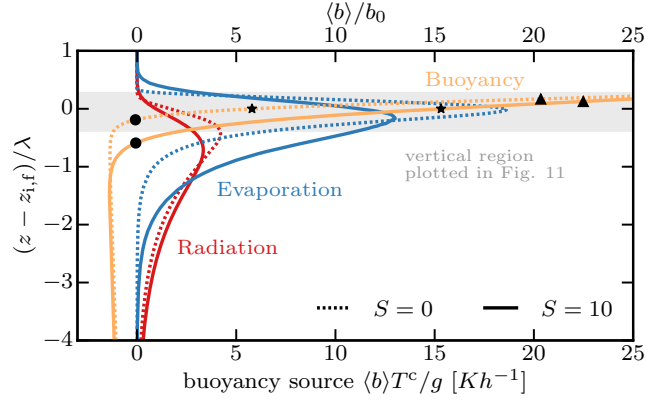
Figure 10: Vertical profiles of the radiative-cooling and evaporative-cooling source terms, as defined in Eq. (41) and (42), at $z_*/\lambda \simeq 15$ for $Re_0 = 400$. The normalized mean buoyancy profile $\langle b \rangle / b_0$ is added as reference. The different symbols correspond to different reference heights: The circle to $z_{i,n}$, the star to $z_{i,f}$, and the triangle to $z_{i,g}$ (cf. Fig. 9).

w_e^{rad} represent the cumulative effect of evaporative and radiative cooling and increase monotonically from zero when z_i is far above the cloud to the maximum values $B_1/\Delta b$ and $E_0/\Delta b$ when z_i is deep within the cloud. In contrast, the mixing contribution w_e^{mix} is evaluated locally at z_i and has a maximum value near $z_{i,f}$. In the remainder of this section, we investigate how shear affects these vertical dependencies, focusing on a region of about 10 m around the EIL. To this aim, we compare the different contributions to the mean entrainment velocity for $S = 0$ and $S = 10$ in Fig. 11; those two cases are chosen since shear effects on the mean entrainment velocity are observed to be negligible for $S \lesssim 5$. The contour plots in Fig. 11 show the variation with height in the vertical axis and with the integral scale of the in-cloud turbulence in the horizontal axis. Entrainment velocities are normalized by the reference value $W_{ref} = B_1/\Delta b \simeq 4\,\mathrm{mm\,s^{-1}}$, where we have used the corrected buoyancy flux $B_1 = \beta B_0$ to account for the fact that, due to condensational warming, only a fraction β of the enthalpy changes induced by radiative cooling translates into buoyancy changes (cf. Appendix A).

5.1 Radiative cooling effects

The direct contribution of radiative cooling, w_e^{rad}, is determined by the cumulative radiative cooling above z_i (or, equivalently, the flux difference between z_i and the free troposphere) and thus by the amount of liquid water above z_i. For a fixed stratification Δb and a fixed velocity jump Δu, cloudy air penetrates deeper into the EIL as in-cloud turbulence intensifies, as discussed in Section 4, which explains the increase of w_e^{rad} with increasing z_*/λ observed in Fig. 11a. In addition, shear broadening brings more cloudy air into the EIL, implying that shear enhances w_e^{rad}. For a strong shear with $\Delta u > (\Delta u)_{crit}$, this enhancement can be large in relative terms, as inferred from Fig. 11b; we obtain for example an enhancement of 100% to 140% with respect to $(w_e^{rad})_{S=0}$ at the height of zero mean buoyancy $z_{i,n}$. The enhancement of radiative cooling in the EIL is accompanied by a weakening of radiative cooling within the cloud (cf. Fig. 10), since the cloud liquid-water specific humidity and thus the net radiative flux difference across the cloud-top region are held constant in our experiments. In-cloud turbulence intensity, however, stays approximately constant since the shear induced weakening of radiative cooling is compensated by a shear induced enhancement of evaporative cooling (cf. section 5.3).

The magnitude of w_e^{rad} and the effect of shear on it depend on the choice of the reference height z_i. The radiative contribution w_e^{rad} contributes $1\% - 3\%$ to the sum
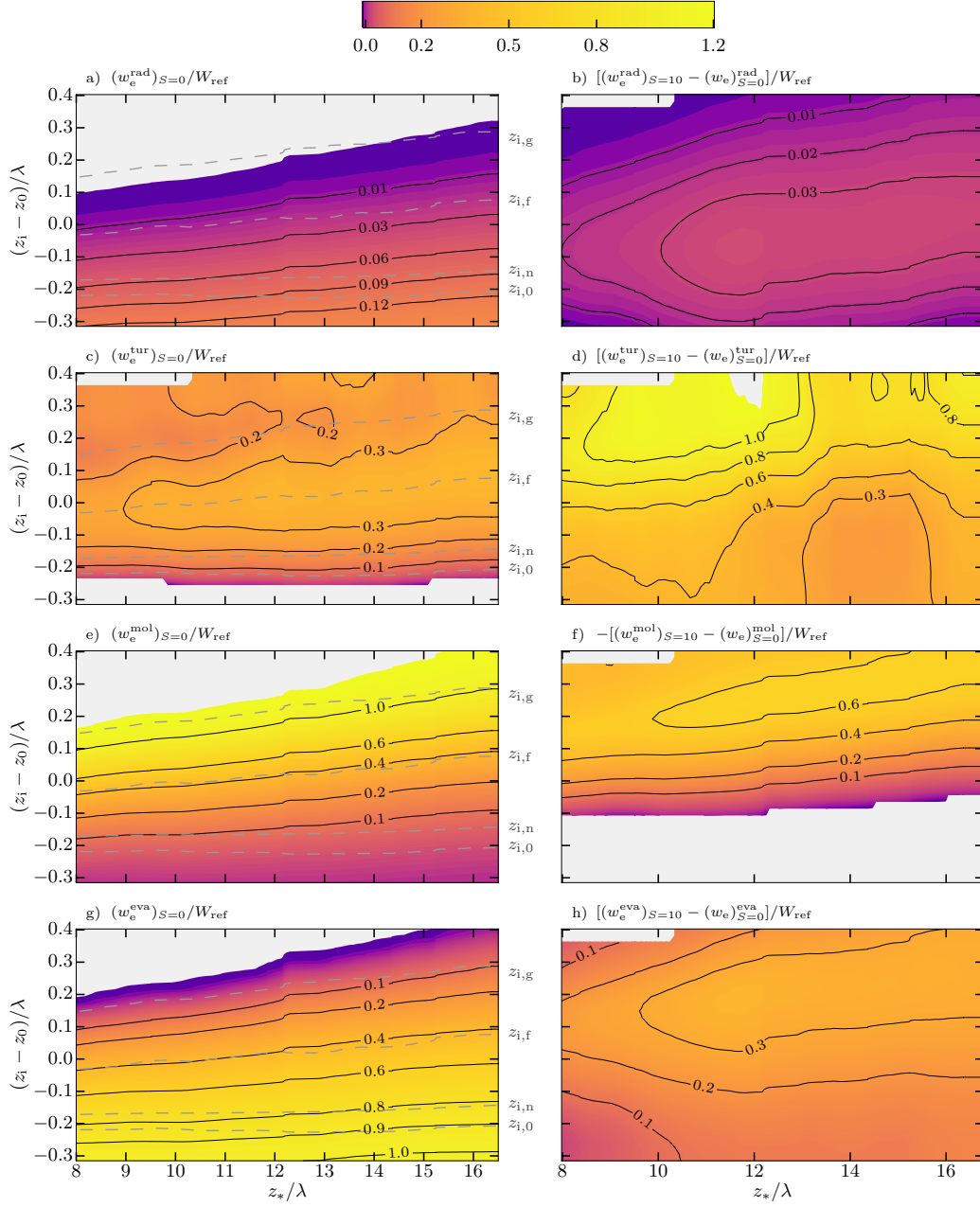
Figure 11: Contour plots showing the different normalized contributions of w_e as defined in Eq. (24). The left column indicates contributions for $S = 0$ and the right column indicates the shear enhancement for $S = 10$, for cases $Re_0 = 400$. The pair a) + b) shows the radiative cooling contribution, the pair c) + d) the turbulent flux contribution, the pair e) + f) the molecular flux contributions, and the pair g) + h) the evaporative cooling contribution. The thin black lines indicate contour lines, while the dashed gray lines indicate the temporal evolution of different reference heights with respect to the reference height z_0 (cf. Fig. 9). For clarity, negative values and values that satisfy the condition $|B| < 0.90|B|_{z_{i,f}}$ are indicated in gray, where the last condition is set to avoid small denominators in Eq. (24). Note that a logarithmic color scale is used.

$w_e^{tur} + w_e^{rad} + w_e^{eva}$ (depending on S and z_*/λ), at the height of minimum buoyancy flux $z_{i,f}$, whereas this contribution increases to 8% − 15% for the height of zero mean buoyancy $z_{i,n}$. This increase is reasonable since more liquid water accumulates above a reference height as the reference height moves downward and $z_{i,n} < z_{i,f}$ (cf. Fig. 9). Nonetheless, since most of the liquid water and thus most of the radiative flux difference across the cloud-top region are located below $z_{i,n}$, the contribution of w_e^{rad} to the mean entrainment velocity is small when w_e is evaluated above $z_{i,n}$. Hence, at least for DYCOMS-II like conditions, the parametrization of shear effects on w_e^{rad} is not a priority, as long as Δu is less than the depletion velocity jump necessary to thin the cloud enough to change the net radiative flux difference across the cloud-top region (cf. Section 3).

5.2 *The mixing contribution*

The mixing contribution to w_e consists of a turbulent part and a molecular part. As observed in Fig. 11c,d, the turbulent part of the mixing contribution, w_e^{tur}, and the effect of shear on it, depend significantly on the choice of the reference height, since the turbulent buoyancy flux varies substantially in the EIL (cf. Fig. 4). By definition, the magnitude of w_e^{tur} reaches a maximum near $z_{i,f}$, and w_e^{tur} contributes 40% − 60% to the sum $w_e^{tur} + w_e^{rad} + w_e^{eva}$ at this height. For reference heights below $z_{i,f}$, the magnitude of w_e^{tur} decreases and so does its relative contribution to the sum $w_e^{tur} + w_e^{rad} + w_e^{eva}$. In contrast, the relative contribution of w_e^{tur} increases above $z_{i,f}$ (e.g. 60% − 80% for $z_{i,g}$) since w_e^{rad} and w_e^{eva} decay more rapidly than w_e^{tur} in this region. Regarding shear effects, we observe that a strong shear with $\Delta u > (\Delta u)_{crit}$ significantly increases the magnitude of the negative buoyancy flux and therefore also w_e^{tur}; for example, shear increases w_e^{tur} by 35% to 45% with respect to $(w_e^{tur})_{S=0}$ at $z_{i,f}$ and by approximately 200% at $z_{i,g}$. All these observations indicate that w_e^{tur} tends to dominate sum $w_e^{tur} + w_e^{rad} + w_e^{eva}$ for reference heights located around $z_{i,f}$ and above it, and finding a shear-dependent parameterization of w_e^{tur} is key to understand shear effects on the evolution of stratocumulus clouds.

The molecular part of the mixing contribution, w_e^{mol}, can become larger than the turbulent part at the top of the EIL, since the turbulent fluctuations decay faster than the mean buoyancy gradient in that stably stratified region. In numerical simulations, however, the molecular contribution is artificially exaggerated and we need to understand this contribution to interpret the numerical results, even if w_e^{mol} is irrelevant under atmospheric conditions. For the Reynolds numbers achieved in our simulations, the molecular part is comparable to the turbulent part at $z_{i,f}$, where the turbulent part is maximum, for $S = 0$ (cf. Fig. 11e). However, a strong shear substantially decreases the magnitude of w_e^{mol} in most of the EIL (cf. Fig. 11f), whereas the magnitude of w_e^{tur} is substantially increased. This result indicates that, despite the moderate Reynolds numbers achieved in our simulations, the strong effect of shear on w_e^{tur} and thereby on w_e is appropriately represented.

5.3 *Evaporative cooling effects*

The magnitude of w_e^{eva} depends strongly on the choice of the reference height z_i, since evaporative cooling varies strongly within a few meters in the cloud-top region (cf. Figs. 10 and 11g). The evaporative contribution w_e^{eva} reaches its maximum for reference heights located near $z_{i,n}$, as more mixing of environmental and cloudy air accumulates above such reference heights; w_e^{eva} contributes for example 80% − 90% to the sum $w_e^{tur} + w_e^{rad} + w_e^{eva}$ at $z_{i,n}$, while contributing only 20% − 40% at $z_{i,g}$. This implies that w_e^{eva} is the dominant contribution to the entrainment velocity w_e for reference heights located near $z_{i,n}$, in contrast to the mixing contribution, which dominates for reference heights located above $z_{i,f}$.
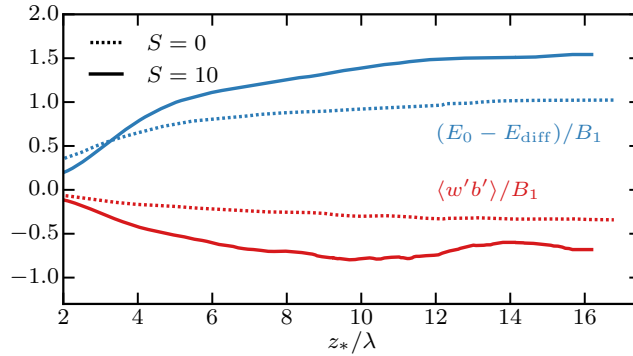
Figure 12: Temporal evolution of the total evaporative cooling term E_0/B_1 and the turbulent buoyancy flux $\langle w'b' \rangle /B_1$ evaluated at $z_{i,f}$ for the cases $Re_0 = 400$. The diffusive correction E_{diff} to E_0 is discussed in the Appendix B.

The importance of evaporative cooling is confirmed by Fig. 12, which shows that the total evaporative cooling E_0 is comparable to the reference buoyancy flux B_1 associated with radiative cooling. As already mentioned before, we note that E_0—as well as w_e^{eva}—are cumulative effects of evaporative cooling, as it appears in Eq. (24), and not the local evaporative-cooling rate $\langle s^{eva} \rangle$ at a given reference height z_i. Locally inside of the cloud, radiative cooling can be larger than evaporative cooling, as shown in Fig. 10. The reason is that evaporative cooling is concentrated within the EIL; for example, for the subtropical conditions considered in this study, the evaporative cooling above $z_{i,n}$ contributes 60% of E_0. Anyhow, total evaporative cooling is expected to decrease if the free troposphere is moistened and if the inversions strength is weakened, as for example observed during the POST campaign (Malinowski et al., 2013). The relative importance of evaporative cooling and radiative cooling is therefore expected to depend on the thermodynamic conditions, and needs further assessment.

A strong shear with $\Delta u > (\Delta u)_{crit}$ enhances w_e^{eva} by increasing the mixing of tropospheric and cloudy air, as shown in Fig. 11h; for example, there is an increase by $30\% - 50\%$ with respect to $(w_e^{eva})_{S=0}$ at $z_{i,n}$. In terms of the total evaporative cooling, $E_0 - E_{diff}$ increases by approximately 50%, as indicated in Fig. 12. [The maximum rate of evaporative cooling $\langle s^{eva} \rangle$ decreases with increasing shear, but this decrease is over-compensated by a broadening of the evaporative cooling profile (cf. Fig. 10).] Shear, therefore, enhances the total amount of evaporative cooling E_0, which is in contrast to the net radiative flux difference R_0 (and hence B_1) being constant. The shear enhancement of evaporative cooling within the cloud below the EIL is about 15% and compensates for the decrease of radiative cooling noted before in Section 5.1. This explains why in-cloud turbulence remains approximately independent of the wind shear. All these observations stress the importance of evaporative cooling and shear effects on it.

Despite this substantial shear enhancement of evaporative cooling, however, we do not observe a cloud-top entrainment instability, understood as a runaway instability that leads to a rapid desiccation of the cloud. This concept is based on the positive feedback that exists between evaporative cooling and entrainment, since evaporative cooling enhances in-cloud turbulence, which in turn enhances entrainment and hence evaporation (Deardorff, 1980b; Randall, 1980). However, this feedback seems to be small because the ratio E_0/B_1 tends towards a constant value for $z_*/\lambda > 12$, as shown in Fig. 12.

5.4 *Deformation effects*

The deformation term w_e^{def} arises from temporal changes in the shape of the mean buoyancy profile and allows us to distinguish between a quasi-steady and an unsteady

state. For a quasi-steady state, w_e^{def} is negligibly small compared to the sum w_e^{tur} + w_e^{rad} + w_e^{eva}, which implies that the shape of the mean buoyancy profile changes slowly compared to the deepening of the STBL. Hence, for a quasi-steady state, the magnitude of w_e depends only weakly on z_i, even though the different contributions to w_e in Eq. (24) strongly vary with z_i. In contrast, in an unsteady state, the deformation term is not negligible, and the shape of the mean buoyancy profile changes on time scales comparable to the turnover time of the large-scale turbulent motions in the STBL. Therefore, different choices of reference height can yield substantially different entrainment velocities.

In our simulations the deformation term w_e^{def} is comparable to the sum $w_e^{tur} + w_e^{rad}$ + w_e^{eva} at $z_{i,n}$, signaling a unsteady state. Deformation effects are indicated in Fig. 11a by the misalignment between contour lines of w_e^{rad} and the time evolution of the different reference heights (dashed lines), which is more pronounced for reference heights located near $z_{i,n}$. This misalignment indicates that, in an unsteady state, the partitioning between the individual contributions of w_e changes significantly as function of z_*/λ and not only as function of height.

Shear weakens the EIL stratification and hence makes the cloud top more susceptible to deformations, since these deformations are created by in-cloud turbulent motions penetrating into the stably stratified EIL (cf. Section 4). Consistently, a strong shear with $\Delta u > (\Delta u)_{crit}$ is observed to increase w_e^{def}, which explains why in Fig. 9 $z_{i,n}$ and $z_{i,o}$ decrease more rapidly for $S = 10$ compared to $S = 0$. Shear effects on the deformation term are therefore important in unsteady regimes.

6 summary and conclusions

Interactions of a mean vertical wind shear and turbulent convection driven by radiative and evaporative cooling of the stratocumulus cloud-top have been studied by means of direct numerical simulations. We have focused on DYCOMS-II like conditions, i.e., subtropical stratocumulus with strong variations of specific humidity and static energy across the cloud top.

Shear effects are only found to be significant if the cloud-top velocity jump Δu exceeds the critical velocity jump $(\Delta u)_{crit} \simeq 4w_*$, where w_* is the convective velocity scale characterizing in-cloud turbulence. For typical values of w_* in the range $0.2\,\mathrm{m\,s^{-1}}$ – $0.9\,\mathrm{m\,s^{-1}}$ (Wood, 2012), one finds $(\Delta u)_{crit} \simeq 1\,\mathrm{m\,s^{-1}} - 4\,\mathrm{m\,s^{-1}}$. For $\Delta u > (\Delta u)_{crit}$ shear enhances the entrainment of tropospheric air substantially. However, for $\Delta u < (\Delta u)_{crit}$ shear effects are negligible and in-cloud turbulence penetrating into the stably stratified entrainment interfacial layer (EIL) dominates the EIL dynamics. This threshold suggests that cloud-top shear associated with large-scale convective motions of the atmospheric boundary layer is unable to enhance cloud-top cooling significantly, since such a shear is typically characterized by velocity jumps commensurate with the convective velocity scale, w_*, and $w_* < (\Delta u)_{crit}$.

Even for a strong wind shear with $\Delta u > (\Delta u)_{crit}$, shear effects are found to remain localized within the EIL, i.e., shear does not affect the in-cloud turbulence intensity. Shear only depletes the cloud, reduces the net radiative cooling, and weakens in-cloud turbulence if wind shear thickens the EIL substantially compared to the cloud thickness. An analytic expression for the corresponding depletion velocity jump $(\Delta u)_{dep}$ is provided and $(\Delta u)_{dep} \simeq 3\,\mathrm{m\,s^{-1}} - 10\,\mathrm{m\,s^{-1}}$ is found for a cloud thickness in the interval $100\,\mathrm{m}$ – $200\,\mathrm{m}$. The range of $(\Delta u)_{dep}$ is consistent with measurement campaigns but is partly in disagreement with with previous LES studies, where a depletion of the cloud is observed for shear velocities with $\Delta u < (\Delta u)_{dep}$. This difference is hypothesized to result from the spurious mixing associated with subgrid models and numerical artifacts.

Although cloud-layer properties (e.g., w_*) remain similar for all shear velocities investigated, a strong shear with $\Delta u > (\Delta u)_{crit}$ enhances the entrainment velocity w_e significantly. This enhancement has been studied by means of an integral analysis of

the buoyancy equation, which provides an analytic decomposition of the entrainment velocity $w_e = dz_i/dt$ into four contributions: The radiative and evaporative cooling contributions w_e^{rad} and w_e^{eva} appear as the cumulative radiative and evaporative cooling above the reference height z_i and not as the local cooling rates at this height. In contrast, the mixing contribution w_e^{mix}, which consists of the sum of a turbulent buoyancy flux and a molecular flux, is locally evaluated at the height z_i. The deformation contribution w_e^{def} describes changes in the shape of the mean buoyancy profile, which are generated by changes in the in- cloud turbulent convection penetrating into the EIL.

The turbulent buoyancy flux contribution w_e^{tur} maximizes near to the height of minimum turbulent buoyancy flux $z_{i,f}$, which renders w_e^{tur} a significant contribution to w_e at this height. As the reference height z_i moves downward toward the height of zero mean buoyancy $z_{i,n}$, the direct contributions from radiation and evaporation w_e^{rad} and w_e^{eva} monotonically increase, since more liquid water accumulates above z_i and more mixing of tropospheric and cloudy air occurs above z_i. We find that w_e^{eva} can significantly exceed w_e^{mix} and w_e^{rad} near $z_{i,n}$, even though total evaporative cooling E_o remains comparable to total radiative cooling R_o (and hence to the reference buoyancy flux B_1) for all cloud-top velocity jumps investigated, namely, $E_o/B_1 \simeq 1.0 - 1.5$. Therefore, at least for DYCOMS-II like conditions the entrainment velocity w_e might be well approximated by w_e^{eva} near $z_{i,n}$ but not so near $z_{i,f}$, where the sum $w_e^{tur} + w_e^{eva}$ needs to be considered. This demonstrates that the partitioning of w_e strongly depends on the choice of the reference height z_i, even though the magnitude of w_e does not in a quasi-steady state, and even though different definitions of the reference height z_i only differ by a few meters. Entrainment-rate parameterizations should consistently reflect this dependence when estimating the different contributions to w_e as needed in mixed-layer models.

A strong shear with $\Delta u > (\Delta u)_{crit}$ enhances w_e^{rad}, w_e^{eva} and w_e^{mix} significantly, indicating that shear effects should be considered in entrainment-rate parameterizations. For example, a strong shear with $\Delta u \simeq 3 \, m \, s^{-1}$ enhances the sum $w_e^{tur} + w_e^{rad} + w_e^{eva}$ by $60\% - 100\%$ compared to the shear-free case at $z_{i,f}$. This enhancement remains finite, however, and we do not observe a cloud-top entrainment instability whereby enhanced evaporative cooling leads to more in-cloud turbulence which in turn promotes more evaporative cooling.

In unsteady cases, the deformation contribution w_e^{def} is nonzero and the magnitude of w_e (and not only the various contributions to it) depends on the choice of the reference height. We find that w_e^{def} decreases as the reference height z_i moves upwards in the direction of $z_{i,g}$, and w_e^{def} increases slightly for strong-shear conditions, i.e., $\Delta u > (\Delta u)_{crit}$. In general, deformations effects are argued to be important when the height of the atmospheric boundary layer varies significantly on time scales comparable to the large-eddy turnover time. Hence deformations are expected to matter during cloud formation processes and during transients, such as during the transition from stratocumulus to shallow cumulus. Within those regimes the deepening of the atmospheric boundary layer might not be well described by one single reference height.

We finally note that performing a conditional analysis of the cloud-top region might provide further insights into the entrainment processes, complementing the conventional analysis based on mean quantities described in this paper. For example, it has been observed that that entrainment operates differently in updraft and downdraft regions (Gerber et al., 2005), and incorporating that knowledge into mean quantities might help to further understand and parametrize the entrainment rates. We note, however, that both a conventional analysis based on mean quantities and a conditional analysis based on the distance to the cloud boundary are complementary with each other since the former can be mathematically related to the latter, and results should therefore be complementary with each other.

A   LINEARIZED FORMULATION

The formulation of the CTML is based on the conservation of the specific humidity q_t and specific enthalpy h. These variables as well as the liquid-water specific humidity q_ℓ can be expressed in terms of three non-dimensional variables χ, ψ and ℓ:

$$q_t = q_t^{\text{c}} + (q_t^{\text{d}} - q_t^{\text{c}})\chi \ , \tag{31}$$

$$h = h^{\text{c}} + (h^{\text{d}} - h^{\text{c}})\chi + c_p^{\text{c}} T^{\text{c}} \psi \ , \tag{32}$$

$$q_\ell = q_\ell^{\text{c}} \ell \ , \tag{33}$$

where the superscripts c and d refer to cloudy and dry air, respectively. The mixing fraction, χ, defines the hypothetical process of adiabatically mixing two air parcels in the mass fraction $(1 - \chi)/\chi$ (Albrecht, Penc, and Schubert, 1985; Nicholls and Leighton, 1986; Bretherton, 1987). The variable ψ describes diabatic deviations introduced by radiative effects (Moeng, Lenschow, and Randall, 1995; Shao et al., 1997; Vanzanten, 2002; Yamaguchi and Randall, 2012), c_p^{c} is the specific heat capacity of cloudy air, and T^{c} is the temperature of cloudy air. The evolution equations for χ and ψ are (Mellado et al., 2010; Lozar and Mellado, 2015; Mellado, 2017)

$$\partial \chi / \partial t + \mathbf{u} \cdot \nabla \chi = \kappa_T \nabla^2 \chi \ , \tag{34}$$

$$\partial \psi / \partial t + \mathbf{u} \cdot \nabla \psi = \kappa_T \nabla^2 \psi - \nabla \cdot \mathbf{R} \ , \tag{35}$$

where κ_T is the thermal diffusivity and microphysical effects are neglected. Here $\mathbf{u}$ is a velocity vector and $\mathbf{R} = R\mathbf{k}$ is the one-dimensional longwave radiative forcing based on Larson, Kotenberg, and Wood (2007), with $\mathbf{k}$ being a unit vector pointing in the vertical direction. The net longwave radiative flux $R = R(z)$ can be well approximated by

$$R = R_{\text{o}} \exp\left[-\lambda^{-1} \int_z^{z_{\text{top}}} q_\ell / q_\ell^{\text{c}} dz'\right] \ , \tag{36}$$

where R_{o} is the net radiative flux cooling the cloud-top region, and λ is the extinction length.

Moreover, we apply the Boussinesq approximation to the Navier-Stokes equation

$$\partial \mathbf{u} / \partial t + \mathbf{u} \cdot \nabla \mathbf{u} = -\nabla p + \nu \nabla^2 \mathbf{u} + b\mathbf{k} \ , \tag{37}$$

where ν refers to kinematic viscosity and b to buoyancy $b = g(\rho - \rho^{\text{c}})/\rho^{\text{c}}$ with ρ being density. We assume that the Prandtl number is equal to one, i.e., $Pr = \nu/\kappa_T = 1$. To complete this set of equations we still need an expression for the normalized liquid water ℓ and the buoyancy b. We can write analytic expressions for these variables when assuming phase equilibrium (infinitely fast thermodynamics) and linearizing the caloric

and thermal equation of state. Under these assumptions, ℓ and b can be diagnosed from the prognostic variables according to

$$\ell = f(\xi) = \epsilon \ln[\exp(\xi/\epsilon) + 1] \,, \tag{38}$$

$$\frac{b}{\Delta b} = \chi \left(\frac{1+D}{1-\chi_{\text{sat}}} \right) + \frac{\psi}{\psi_{\text{b}}} + (\ell - 1) \left(\frac{D + \chi_{\text{sat}}}{1 - \chi_{\text{sat}}} \right) \,, \tag{39}$$

as discussed in Bretherton (1987), Pauluis, Schumacher, et al. (2010), and Lozar and Mellado (2015). Here, ψ_{b} and ξ are given by $\psi_{\text{b}} = (c_p^c T^c \Delta b)/g$ and $\xi = 1 - \chi/\chi_{\text{sat}} - \psi/\psi_{\text{sat}}$, respectively, and the condition $\xi = 0$ defines the saturation surface, which can be used to define the cloud boundary. The parameters ψ_{b} and ψ_{sat} characterize how variations in enthalpy translate into changes of buoyancy and liquid water, respectively. The function f tends to a piecewise linear function in the limit $\epsilon \to 0$, but has a finite second order derivative of order $1/\epsilon$, which is convenient for the numerical calculations. For our simulations we apply $\epsilon = 1/16$ since the obtained results become independent of ϵ for $\epsilon \le 1/16$ as shown in Mellado et al. (2009). The parameter $D = -b_{\text{sat}}/\Delta b$ is the ratio between the buoyancy of a just saturated (no liquid) cloud-dry air mixture, b_{sat}, and the cloud-top buoyancy jump, $\Delta b = b^d - b^c$. Such a mixture occurs at the mixing ratio $\chi = \chi_{\text{sat}}$, where χ_{sat} is the saturation mixing ratio. The parameters D and χ_{sat} fully describe evaporative cooling in the mixing line formulation (Siems and Bretherton, 1992; Mellado et al., 2009) where radiation is absent ($\psi \to 0$); buoyancy reversal instability occurs for $D > 0$. Note that the applied simplifications introduce only a small error of around 3% in the buoyancy (Lozar and Mellado, 2015).

In addition, we can derive a diagnostic equation for the temporal evolution of the buoyancy field, given by

$$D_t b = \kappa_T \nabla^2 b - s^{\text{rad}} - s^{\text{eva}} \,, \tag{40}$$

where the radiative and evaporative source term as (Lozar and Mellado, 2015)

$$s^{\text{rad}} = \left[1 - \frac{\beta^\ell q_\ell^c}{\psi_{\text{sat}}} \right] \frac{g \nabla \cdot \mathbf{R}}{c_p^c T^c} \,, \tag{41}$$

$$s^{\text{eva}} = g \beta^\ell q_\ell^c \left[\frac{-(\partial_t q_\ell)_{\text{pha}}}{q_\ell^c} + \frac{d_\xi f \nabla \cdot \mathbf{R}}{\psi_{\text{sat}} c_p^c T^c} \right] \,. \tag{42}$$

The parameter ψ_{sat} quantifies radiative effects at saturation conditions and β^ℓ specifies phase change effects of the buoyancy. Due to condensational warming only a part β of the enthalpy changes, induced by radiative cooling, translates into buoyancy changes, where β is given by $\beta = (1 - \beta^\ell q_\ell^c \psi_{\text{sat}}^{-1}) \simeq 0.53$. Condensational warming is also the origin of the second summand in Eq. (42) and motivates to introduce a corrected reference buoyancy flux as $B_1 = (1 - \beta^\ell q_\ell^c \psi_{\text{sat}}^{-1}) R_0 g (c_p^c T^c)^{-1} = \beta B_0$.

B   REYNOLDS NUMBER EFFECTS

The viscosity of the air consider in the DNS is about $0.01\,\text{m s}^{-2}$. This is about 2 orders of magnitude smaller than the effective viscosity considered in previous large-eddy simulations, where typical grid spacings of $2.5\,\text{m}$ and typical velocities of $1\,\text{m s}^{-1}$ imply a numerical diffusivity of about $2.5\,\text{m s}^{-2}$. However, the viscosity in the DNS is still a factor of 1000 larger than the atmospheric value, and we need to assess the effect of changing the Reynolds number on the properties discussed in this study. We find that increasing the Reynolds number by a factor of up to three changes most of the properties by less than 20% (cf. Fig. 13). Hence, the low-to-moderate Reynolds numbers in DNS start to be high enough for some properties to show only a weak dependence on the Reynolds number, an observation referred to as Reynolds number similarity (Dimotakis,
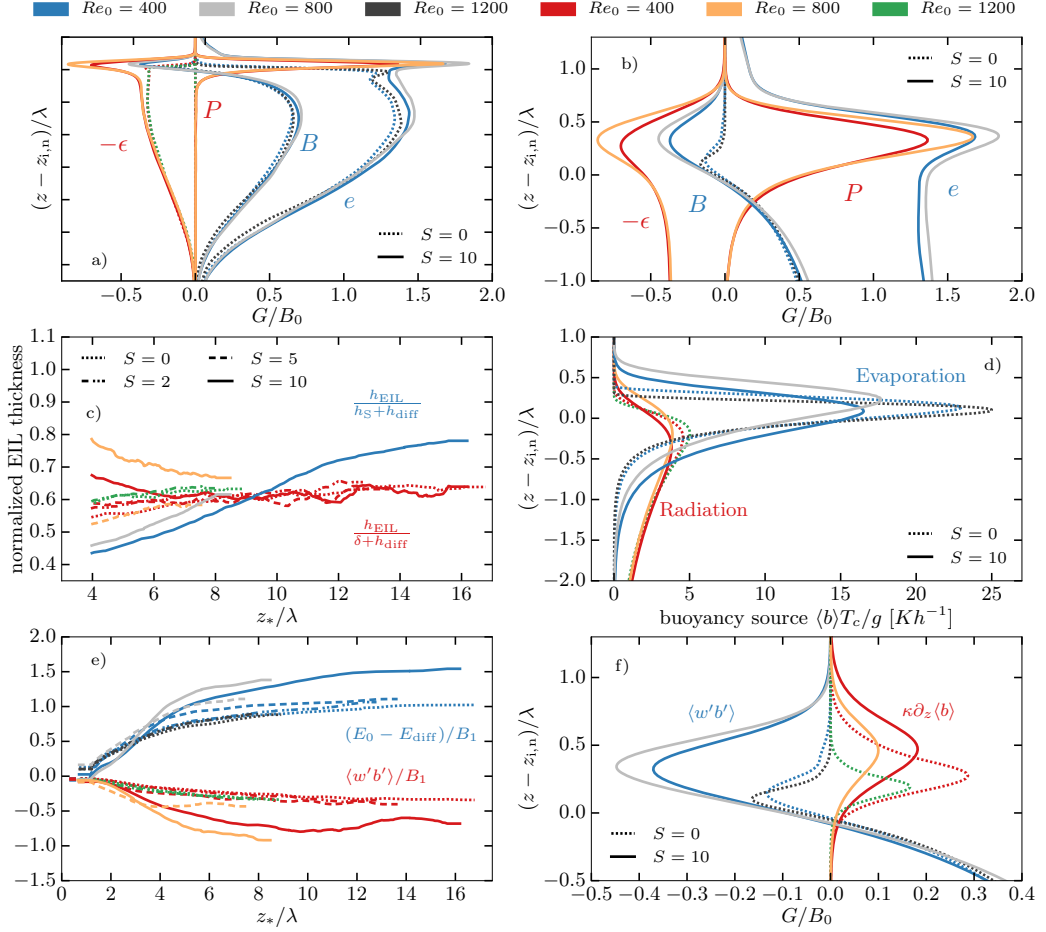
Figure 13: Reynolds number effects for figures discussed in the main text. Fig. **a)** and **b)** show vertical profiles of the TKE budget at $z_*/\lambda = 7.5$ (cf. Fig. 4), **c)** shows the time evolution of the normalized EIL thickness (cf. Fig. 3), **d)** shows vertical profiles of the buoyancy source terms at $z_*/\lambda = 7.5$ (cf. Fig. 10), **e)** shows the time evolution of the total evaporative cooling term and the turbulent buoyancy flux (cf. Fig. 12), and **f)** shows vertical profiles of the turbulent and molecular flux at $z_*/\lambda = 7.5$ (not presented in the main text). Different colors indicate different Reynolds numbers Re_0 and different line styles correspond to different shear numbers S. Note that dashed lines for $Re_0 = 800$ correspond to $S = 6$ (cf. Table 2).

Table 3: The Ozmidov scale δ_{Oz} and its ratio with the Kolmogorov scale η for different shear numbers S and different Reynolds numbers Re_0. Variables are evaluated at the reference height z_i for the final value of z_*/λ.

S	Re_0	δ_{Oz} [m] at $z_{i,f}$	δ_{Oz} [m] at $z_{i,n}$	δ_{Oz}/η at $z_{i,f}$	δ_{Oz}/η at $z_{i,n}$
0	400	0.3	1.0	1.5	5.0
10	400	0.6	2.2	3.5	11.0
0	1200	0.2	0.9	2.5	10.0
10	800	0.6	2.1	6.0	18.0

2005; Mellado et al., 2018). This allows us to extrapolate our results to a certain extend to atmospheric conditions.

The major Reynolds-number effects that we observe are that a substantial part of the mixing contribution w_e^{mix} to the mean entrainment velocity stems from the molecular term, and that a substantial part of the total evaporative cooling E_0 is associated with molecular diffusion. The first effect has been discussed in the Section 5.2. Regarding the second effect, we follow Lozar and Mellado (2015) and account for this effect by applying a diffusive correction $E_{diff}/B_1 \simeq 0.3 - 0.45$ to E_0/B_1 (cf. Fig 12). Note that the diffusive correction E_{diff} is related to the diffusive length scale h_{diff} by $E_{diff} = \nu\Delta b(D/\chi_{sat} + 1)/h_{diff}$ (cf. Section 2.2.2). With this correction, we find that the lines $(E_0 - E_{diff})/B_1$ for different Reynolds numbers are close to each other, so that the discussion in terms of $(E_0 - E_{diff})/B_1$ is approximately independent of the Reynolds number (cf. Fig. 13).

Last, analyzing the Ozmidov length scale further supports that our low-to-moderate Reynolds numbers simulations start to appropriately represent mixing in the EIL. The Ozmidov length is defined as $\delta_{Oz} = (\varepsilon/N^3)^{1/2}$, where ε is the viscous dissipation rate of turbulent kinetic energy and N is the mean buoyancy gradient, and δ_{Oz} varies between 0.5 m and 4 m for typical atmospheric conditions (Katzwinkel, Siebert, and Shaw, 2012; Mellado, Stevens, and Schmidt, 2014; Jen-La Plante et al., 2016). The Ozmidov length separates larger motions that are dominated by gravity waves, which are not efficient in mixing scalars, from smaller motions that are dominated by turbulence, which are very efficient in mixing scalars. If the Ozmidov scale is not resolved in a numerical simulation, unphysical down-gradient mixing from turbulence models or other numerical artifacts overestimate the actual mixing. For the performed simulations, we find $\delta_{Oz} \simeq 0.2\,\text{m} - 2\,\text{m}$ in the EIL, which results in $(\delta_{Oz}/\eta)_{z_{i,f}} \simeq 2 - 6$ and $(\delta_{Oz}/\eta)_{z_{i,n}} \simeq 5 - 18$ (cf. Table 3). These ratios, although moderate, are sufficiently large for the DNS to reproduce the entrainment rates observed in measurements, and to show certain degree of Reynolds number similarity in the properties discussed in this work, as argued above.

REFERENCES

Ackerman, Andrew S et al. (2004). "The impact of humidity above stratiform clouds on indirect aerosol climate forcing". In: *Nature* 432.7020, p. 1014.

Ackerman, Andrew S et al. (2009). "Large-eddy simulations of a drizzling, stratocumulus-topped marine boundary layer". In: *Monthly Weather Review* 137.3, pp. 1083–1110.

Albrecht, Bruce A, Richard S Penc, and Wayne H Schubert (1985). "An observational study of cloud-topped mixed layers". In: *Journal of the atmospheric sciences* 42.8, pp. 800–822.

Antonia, RA (1981). "Conditional sampling in turbulence measurement". In: *Annual review of fluid mechanics* 13.1, pp. 131–156.

Bony, Sandrine and Jean-Louis Dufresne (2005). "Marine boundary layer clouds at the heart of tropical cloud feedback uncertainties in climate models". In: *Geophysical Research Letters* 32.20.

Bretherton, CS, Peter N Blossey, and Junya Uchida (2007). "Cloud droplet sedimentation, entrainment efficiency, and subtropical stratocumulus albedo". In: *Geophysical research letters* 34.3.

Bretherton, Christopher S (1987). "A theory for nonprecipitating moist convection between two parallel plates. Part I: Thermodynamics and "linear" solutions". In: *Journal of the atmospheric sciences* 44.14, pp. 1809–1827.

Bretherton, Christopher S et al. (1999). "An intercomparison of radiatively driven entrainment and turbulence in a smoke cloud, as simulated by different numerical models". In: *Quarterly Journal of the Royal Meteorological Society* 125.554, pp. 391–423.

Brost, RA, JC Wyngaard, and DH Lenschow (1982). "Marine stratocumulus layers. Part II: Turbulence budgets". In: *Journal of the Atmospheric Sciences* 39.4, pp. 818–836.

Brucker, Kyle A and Sutanu Sarkar (2007). "Evolution of an initially turbulent stratified shear layer". In: *Physics of Fluids (1994-present)* 19.10, p. 105105.

Caughey, SJ, BA Crease, and WT Roach (1982). "A field study of nocturnal stratocumulus II Turbulence structure and entrainment". In: *Quarterly Journal of the Royal Meteorological Society* 108.455, pp. 125–144.

Dal Gesso, S et al. (2015). "A single-column model intercomparison on the stratocumulus representation in present-day and future climate". In: *Journal of Advances in Modeling Earth Systems* 7.2, pp. 617–647.

De Roode, Stephan R et al. (2014a). "A mixed-layer model study of the stratocumulus response to changes in large-scale conditions". In: *Journal of Advances in Modeling Earth Systems* 6.4, pp. 1256–1270.

— (2014b). "A mixed-layer model study of the stratocumulus response to changes in large-scale conditions". In: *Journal of Advances in Modeling Earth Systems* 6.4, pp. 1256–1270.

Deardorff, JW (1980a). "Cloud top entrainment instability". In: *Journal of the Atmospheric Sciences* 37.1, pp. 131–147.

Deardorff, James W (1970). "Convective velocity and temperature scales for the unstable planetary boundary layer and for Rayleigh convection". In: *Journal of the atmospheric sciences* 27.8, pp. 1211–1213.

— (1980b). "Stratocumulus-capped mixed layers derived from a three-dimensional model". In: *Boundary-Layer Meteorology* 18.4, pp. 495–527.

— (1981). "On the distribution of mean radiative cooling at the top of a stratocumulus-capped mixed layer". In: *Quarterly Journal of the Royal Meteorological Society* 107.451, pp. 191–202.

Dimotakis, Paul E (2005). "Turbulent mixing". In: *Annu. Rev. Fluid Mech.* 37, pp. 329–356.

Driedonks, AGM and PG Duynkerke (1989). "Current problems in the stratocumulus-topped atmospheric boundary layer". In: *Boundary-Layer Meteorology* 46.3, pp. 275–303.

Faloona, Ian et al. (2005). "Observations of entrainment in eastern Pacific marine stratocumulus using three conserved scalars". In: *Journal of the atmospheric sciences* 62.9, pp. 3268–3285.

Fedorovich, Evgeni and Robert Conzemius (2008). "Effects of wind shear on the atmospheric convective boundary layer structure and evolution". In: *Acta Geophysica* 56.1, pp. 114–141.

Gerber, H, Szymon P Malinowski, and Haflidi Jonsson (2016). "Evaporative and radiative cooling in POST Stratocumulus". In: *Journal of the Atmospheric Sciences* 73.10, pp. 3877–3884.

Gerber, H et al. (2005). "Holes and entrainment in stratocumulus". In: *Journal of the atmospheric sciences* 62.2, pp. 443–459.

Gerber, Hermann et al. (2014). "Radiative Cooling of Stratocumulus". In: *14th AMS Atmospheric Radiation Conference, At Boston, MA, U.S.A.* DOI: 10.13140/2.1.4016.2563.

Haman, Krzysztof E (2009). "Simple approach to dynamics of entrainment interface layers and cloud holes in stratocumulus clouds". In: *Quarterly Journal of the Royal Meteorological Society* 135.638, pp. 93–100.

Hill, Adrian A, Graham Feingold, and Hongli Jiang (2009). "The influence of entrainment and mixing assumption on aerosol–cloud interactions in marine stratocumulus". In: *Journal of the Atmospheric Sciences* 66.5, pp. 1450–1464.

Howland, CJ, JR Taylor, and CP Caulfield (2018). "Testing linear marginal stability in stratified shear layers". In: *Journal of Fluid Mechanics* 839.

Hudson, James G and Seong Soo Yum (1997). "Droplet spectral broadening in marine stratus". In: *Journal of the atmospheric sciences* 54.22, pp. 2642–2654.

J Kurowski, Marcin, Szymon P Malinowski, and Wojciech W Grabowski (2009). "A numerical investigation of entrainment and transport within a stratocumulus-topped boundary layer". In: *Quarterly Journal of the Royal Meteorological Society* 135.638, pp. 77–92.

Jen-La Plante, Imai et al. (2016). "Physics of Stratocumulus Top (POST): turbulence characteristics". In: *Atmospheric Chemistry and Physics* 16.15, pp. 9711–9725.

Katzwinkel, J, H Siebert, and RA Shaw (2012). "Observation of a self-limiting, shear-induced turbulent inversion layer above marine stratocumulus". In: *Boundary-layer meteorology* 145.1, pp. 131–143.

Kopec, Marta K, Szymon P Malinowski, and Zbigniew P Piotrowski (2016). "Effects of wind shear and radiative cooling on the stratocumulus-topped boundary layer". In: *Quarterly Journal of the Royal Meteorological Society* 142.701, pp. 3222–3233.

Larson, Vincent E, Kurt E Kotenberg, and Norman B Wood (2007). "An analytic longwave radiation formula for liquid layer clouds". In: *Monthly weather review* 135.2, pp. 689–699.

Lele, Sanjiva K (1992). "Compact finite difference schemes with spectral-like resolution". In: *Journal of computational physics* 103.1, pp. 16–42.

Lilly, Douglas K (1968). "Models of cloud-topped mixed layers under a strong inversion". In: *Quart. J. Roy. Meteor. Soc* 94.401, pp. 292–309.

Lock, AP and MK MacVean (1999). "The parametrization of entrainment driven by surface heating and cloud-top cooling". In: *Quarterly Journal of the Royal Meteorological Society* 125.553, pp. 271–299.

Lozar, A de and JP Mellado (2014). "Cloud droplets in a bulk formulation and its application to buoyancy reversal instability, QJ Roy". In: *Meteor. Soc* 140, pp. 1493–1504.

Lozar, Alberto de and Juan Pedro Mellado (2013). "Direct numerical simulations of a smoke cloud–top mixing layer as a model for stratocumuli". In: *Journal of the Atmospheric Sciences* 70.8, pp. 2356–2375.

— (2015). "Mixing driven by radiative and evaporative cooling at the stratocumulus top". In: *Journal of the Atmospheric Sciences* 72.12, pp. 4681–4700.

— (2017). "Reduction of the entrainment velocity by cloud droplet sedimentation in stratocumulus". In: *Journal of the Atmospheric Sciences* 74.3, pp. 751–765.

Mahrt, L and DH Lenschow (1976). "Growth dynamics of the convectively mixed layer". In: *Journal of the Atmospheric Sciences* 33.1, pp. 41–51.

Malinowski, SP et al. (2013). "Physics of Stratocumulus Top (POST): turbulent mixing across capping inversion". In: *Atmospheric Chemistry and Physics* 13.24, pp. 12171–12186.

Martin, GM, DW Johnson, and An Spice (1994). "The measurement and parameterization of effective radius of droplets in warm stratocumulus clouds". In: *Journal of the Atmospheric Sciences* 51.13, pp. 1823–1842.

Mellado, Juan Pedro (2010). "The evaporatively driven cloud-top mixing layer". In: *Journal of Fluid Mechanics* 660, pp. 5–36.

— (2012). "Direct numerical simulation of free convection over a heated plate". In: *Journal of Fluid Mechanics* 712, pp. 418–450.

— (2017). "Cloud-Top Entrainment in Stratocumulus Clouds". In: *Annual Review of Fluid Mechanics* 49, pp. 145–169.

Mellado, Juan Pedro and Cedrick Ansorge (2012). "Factorization of the Fourier transform of the pressure-Poisson equation using finite differences in colocated grids". In: *ZAMM-Journal of Applied Mathematics and Mechanics/Zeitschrift für Angewandte Mathematik und Mechanik* 92.5, pp. 380–392.

Mellado, Juan Pedro, Bjorn Stevens, and Heiko Schmidt (2014). "Wind shear and buoyancy reversal at the top of stratocumulus". In: *Journal of the Atmospheric Sciences* 71.3, pp. 1040–1057.

Mellado, Juan Pedro, Lipo Wang, and Norbert Peters (2009). "Gradient trajectory analysis of a scalar field with external intermittency". In: *Journal of Fluid Mechanics* 626, pp. 333–365.

Mellado, Juan Pedro et al. (2009). "Buoyancy reversal in cloud-top mixing layers". In: *Quarterly Journal of the Royal Meteorological Society* 135.641, pp. 963–978.

— (2010). "Two-fluid formulation of the cloud-top mixing layer for direct numerical simulation". In: *Theoretical and Computational Fluid Dynamics* 24.6, pp. 511–536.

Mellado, Juan Pedro et al. (2018). "DNS and LES for simulating stratocumulus: Better together". In: *Journal of Advances in Modeling Earth Systems*, https://doi.org/10.1029/2018MS001312.

Miles, Natasha L, Johannes Verlinde, and Eugene E Clothiaux (2000). "Cloud droplet size distributions in low-level stratiform clouds". In: *Journal of the atmospheric sciences* 57.2, pp. 295–311.

Moeng, C-H (1998). "Stratocumulus-topped atmospheric planetary boundary layer". In: *Buoyant Convection in Geophysical Flows*. Springer, pp. 421–440.

Moeng, Chin-Hoh, Don H Lenschow, and David A Randall (1995). "Numerical investigations of the roles of radiative and evaporative feedbacks in stratocumulus entrainment and breakup". In: *Journal of the atmospheric sciences* 52.16, pp. 2869–2883.

Moeng, Chin-Hoh, Peter P Sullivan, and Bjorn Stevens (1999). "Including radiative effects in an entrainment rate formula for buoyancy-driven PBLs". In: *Journal of the atmospheric sciences* 56.8, pp. 1031–1049.

Nicholls, S and J Leighton (1986). "An observational study of the structure of stratiform cloud sheets: Part I. Structure". In: *Quarterly Journal of the Royal Meteorological Society* 112.472, pp. 431–460.

Noda, AT and M Satoh (2014). "Intermodel variances of subtropical stratocumulus environments simulated in CMIP5 models". In: *Geophysical Research Letters* 41.21, pp. 7754–7761.

Pauluis, Olivier, Jörg Schumacher, et al. (2010). "Idealized moist Rayleigh-Bénard convection with piecewise linear equation of state". In: *Communications in Mathematical Sciences* 8.1, pp. 295–319.

Pedersen, JG et al. (2018). "Anisotropy of observed and simulated turbulence in marine stratocumulus". In: *Journal of Advances in Modeling Earth Systems* 10.2, pp. 500–515.

Pedersen, Jesper G, Szymon P Malinowski, and Wojciech W Grabowski (2016). "Resolution and domain-size sensitivity in implicit large-eddy simulation of the stratocumulus-topped boundary layer". In: *Journal of Advances in Modeling Earth Systems* 8.2, pp. 885–903.

Randall, David A (1980). "Conditional instability of the first kind upside-down". In: *Journal of the Atmospheric Sciences* 37.1, pp. 125–130.

Rogers, R. R. and M. K. Yau (1989). "A Short Course in Cloud Physics". In: *Elsevier* 3d ed. 304 pp.

Roode, Stephan R de and Qing Wang (2007). "Do stratocumulus clouds detrain? FIRE I data revisited". In: *Boundary-layer meteorology* 122.2, pp. 479–491.

Sayler, Bentley J and Robert E Breidenthal (1998). "Laboratory simulations of radiatively induced entrainment in stratiform clouds". In: *Journal of Geophysical Research: Atmospheres (1984–2012)* 103.D8, pp. 8827–8837.

Shao, Qingqiu et al. (1997). "A method to determine the amounts of cloud-top radiative and evaporative cooling in a stratocumulus-topped boundary layer". In: *Quarterly Journal of the Royal Meteorological Society* 123.544, pp. 2187–2213.

Siems, Steven T and Christopher S Bretherton (1992). "A Numerical Investigation of Cloud-Top Entrainment Instability and Related Experiments". In: *Quarterly Journal of the Royal Meteorological Society* 118.507, pp. 787–818.

Smyth, William D and James N Moum (2000). "Length scales of turbulence in stably stratified mixing layers". In: *Physics of Fluids (1994-present)* 12.6, pp. 1327–1342.

Stevens, Bjorn (2002). "Entrainment in stratocumulus-topped mixed layers". In: *Quarterly Journal of the Royal Meteorological Society* 128.586, pp. 2663–2690.

— (2005). "Atmospheric moist convection". In: *Annu. Rev. Earth Planet. Sci.* 33, pp. 605–643.

Stevens, Bjorn, Chin-Hoh Moeng, and Peter P Sullivan (1999). "Large-eddy simulations of radiatively driven convection: Sensitivities to the representation of small scales". In: *Journal of the atmospheric sciences* 56.23, pp. 3963–3984.

Stevens, Bjorn et al. (2003). "On entrainment rates in nocturnal marine stratocumulus". In: *Quarterly Journal of the Royal Meteorological Society* 129.595, pp. 3469–3493.

Stevens, Bjorn et al. (2005). "Evaluation of large-eddy simulations via observations of nocturnal marine stratocumulus". In: *Monthly weather review* 133.6, pp. 1443–1462.

Stull, Roland B (2012). *An introduction to boundary layer meteorology*. Vol. 13. Springer Science & Business Media.

Sullivan, Peter P et al. (1998). "Structure of the entrainment zone capping the convective atmospheric boundary layer". In: *Journal of the atmospheric sciences* 55.19, pp. 3042–3064.

Twomey, S (1974). "Pollution and the planetary albedo". In: *Atmospheric Environment (1967)* 8.12, pp. 1251–1256.

VanZanten, MC et al. (2005). "Observations of drizzle in nocturnal marine stratocumulus". In: *Journal of the atmospheric sciences* 62.1, pp. 88–106.

Vanzanten, Margreet C (2002). "Radiative and evaporative cooling in the entrainment zone of stratocumulus–the role of longwave radiative cooling above cloud top". In: *Boundary-layer meteorology* 102.2, pp. 253–280.

Wang, S, X Zheng, and Q Jiang (2012). "Strongly sheared stratocumulus convection: an observationally based large-eddy simulation study". In: *Atmospheric Chemistry and Physics* 12.11, pp. 5223–5235.

Wang, Shouping, Jean-Christophe Golaz, and Qing Wang (2008). "Effect of intense wind shear across the inversion on stratocumulus clouds". In: *Geophysical Research Letters* 35.15.

Wood, Robert (2000). "Parametrization of the effect of drizzle upon the droplet effective radius in stratocumulus clouds". In: *Quarterly Journal of the Royal Meteorological Society* 126.570, pp. 3309–3324.

— (2012). "Stratocumulus clouds". In: *Monthly Weather Review* 140.8, pp. 2373–2423.

Yamaguchi, Takanobu and David A Randall (2008). "Large-eddy simulation of evaporatively driven entrainment in cloud-topped mixed layers". In: *Journal of the Atmospheric Sciences* 65.5, pp. 1481–1504.

— (2012). "Cooling of entrained parcels in a large-eddy simulation". In: *Journal of the Atmospheric Sciences* 69.3, pp. 1118–1136.

Zhang, Minghua et al. (2013). "CGILS: Results from the first phase of an international project to understand the physical mechanisms of low cloud feedbacks in single column models". In: *Journal of Advances in Modeling Earth Systems* 5.4, pp. 826–842.

3

COMPETING EFFECTS OF WIND SHEAR AND DROPLET SEDIMENTATION WITHIN STRATOCUMULUS TOPS

The attached paper has been published in a modified version as:

Bernhard Schulz (B.S.) and Juan Pedro Mellado (JP.M.) contributed to the paper as follows: JP.M. supervised the findings of this work and provided guidance during the analysis and writing processes. Both JP.M and B.S developed the idea to this work. B.S planned and carried out the numerical simulations. B.S analyzed the data and developed the theoretical formalism that lead to the presented results. In particular, B.S performed the analysis of the entrainment rate equation. B.S took the lead in writing the manuscript, while JP.M. provided critical feedback on the manuscript and helped to finalize this publication.

Competing Effects of Droplet Sedimentation and Wind Shear on Entrainment in Stratocumulus

BERNHARD SCHULZ AND JUAN PEDRO MELLADO

Max Planck Institute for Meteorology, Bundesstr. 53, 20146 Hamburg, Germany

Abstract

The joint effect of droplet sedimentation and wind shear on cloud-top entrainment in stratocumulus is investigated with direct numerical simulations. Although it is well understood that droplet sedimentation weakens entrainment while wind shear enhances entrainment, there is no consensus on the magnitude of each process. We find that the entrainment reduction by droplet sedimentation is sufficiently strong to completely compensate the entrainment enhancement by wind shear, and thus droplet-sedimentation and wind-shear effects can be equally important for cloud-top entrainment. For instance, for the subtropical conditions considered here, droplet sedimentation weakens entrainment by up to 40% while wind shear enhances entrainment by up to 40%. This result implies that the droplet size distribution can substantially affect cloud lifetimes not only because of its effect on rain formation but also because of its effect on cloud-top entrainment, which emphasizes the need for a better characterization of droplet size distributions in stratocumulus. A second implication is that entrainment velocity parameterizations should pay equal attention to droplet-sedimentation and to wind-shear effects.

1 INTRODUCTION

Due to their net cooling effect and large area coverage, stratocumulus clouds are key for the Earth's radiation balance. However, predicting the lifetime of stratocumulus remains a challenge, partly because of the difficulty to quantify the interaction of the various processes that compound cloud-top entrainment (Stevens, 2005; Wood, 2012; Mellado, 2017). In this work, we study the interaction of two processes involved, namely, droplet sedimentation and cloud-top wind shear.

Droplet sedimentation and cloud-top wind shear can substantially alter cloud-top entrainment, and they do it in opposite ways. Droplet sedimentation removes droplets from the entrainment interfacial layer (EIL), which reduces entrainment directly by inducing an upward sedimentation buoyancy flux and indirectly by reducing evaporative cooling (e.g. Ackerman et al., 2004; Bretherton, Blossey, and Uchida, 2007; Ackerman et al., 2009; Hill, Feingold, and Jiang, 2009; Lozar and Mellado, 2017). Meanwhile, wind shear enhances the mixing between free-tropospheric air and cloudy air, which increases entrainment directly by increasing the downward turbulent buoyancy flux and indirectly by enhancing evaporative cooling (e.g. Driedonks and Duynkerke, 1989; Katzwinkel, Siebert, and Shaw, 2012; Wang, Zheng, and Jiang, 2012; Mellado, Stevens, and Schmidt, 2014; Kopec, Malinowski, and Piotrowski, 2016; Schulz and Mellado, 2018). These opposing effects raise the question whether droplet-sedimentation and wind-shear effects can compensate each other. We address this question here by means of direct numerical simulations (DNSs).

An important aspect is the representation of motions at meter and submeter scales. While studies based on large eddy simulations (LESs) report a sedimentation-induced reduction of the entrainment velocity of only 3-25% (Bretherton, Blossey, and Uchida,

2007; Ackerman et al., 2009; Hill, Feingold, and Jiang, 2009), a study based on DNSs indicates that sedimentation effects can be 2 to 3 times stronger (Lozar and Mellado, 2017). This discrepancy is attributed to the size of the smallest resolved scales. The mixing length scale that is physically relevant is on the order of 1 m or less, larger scales being dominated by wave-like motions, which do not mix scalars very efficiently, and smaller scales being dominated by turbulent motions, which mix scalars very efficiently (the Ozmidov scale, see review by Mellado et al., 2018). Down-gradient turbulence models represent wave-like motions very poorly, which explains why LES with grid spacings of 5 m overestimate the upward mixing of liquid water at the cloud top and thereby artificially compensate sedimentation effects. Numerical diffusion aggravates this problem. In contrast, DNS with grid spacings on the order of 0.5 m allows to resolve the mixing length scales that are physically relevant (Lozar and Mellado, 2017; Mellado et al., 2018). Using this high resolution shows that the reduction of the entrainment velocity by droplet sedimentation is about 40% (Lozar and Mellado, 2017), which is comparable to the shear enhancement of the entrainment velocity observed by citetschulz2018wind. This suggests that both processes can indeed compensate each other.

Another important aspect of the analysis of entrainment is the strong vertical variations of the EIL properties. This is particularly relevant for the study of the mean entrainment velocity, where entrainment velocity contributions from radiative cooling, evaporative cooling and turbulent mixing can have order-of-one variations over the few meters that separate the reference heights typically used in the analysis of entrainment, such as the height of minimum turbulent buoyancy flux or the height of maximum mean buoyancy gradient (see discussion in Schulz and Mellado, 2018). Hence, in this work, we also investigate how the relative importance of droplet sedimentation and cloud-top wind shear depends on this choice of the reference height.

This paper is structured as follows. Section 2 introduces the cloud-top mixing layer (CTML) and discusses the simulation set-up. Section 3 introduces some fundamental quantities which characterize the vertical structure of the CTML and in particular discusses sedimentation and shear effects on the EIL. Finally, section 4 investigates whether sedimentation and shear effects on the entrainment velocity can compensate each other. A summary of the results is given in section 5.

2 SIMULATION SET-UP

We use direct numerical simulations of the cloud-top mixing layer (CTML) to assess the combined effect of droplet sedimentation and wind shear on cloud-top entrainment. The CTML mimics the upper part of a stratocumulus topped boundary layer and consists of a layer of relatively warm and dry air, representing the free troposphere, and a layer of relatively cold and moist air, representing the cloud layer below (see Figure 1). Although the simplified set-up of the CTML neglects the effect of the large-scale motions
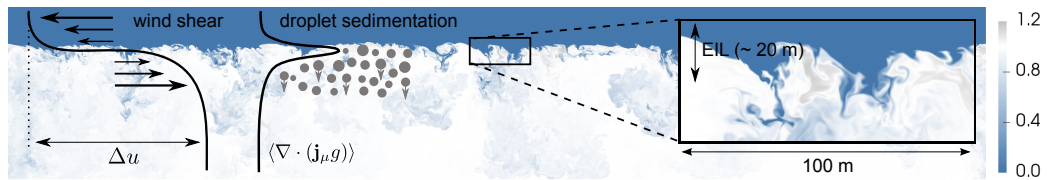
Figure 1: Vertical cross-section of the simulated cloud-top mixing layer showing the liquid water specific humidity field q_ℓ normalized by its in-cloud value q_ℓ^c. The mean velocity profile $\langle u \rangle$ and the mean profile of the divergence of the sedimentation buoyancy flux $\langle \nabla \cdot (\mathbf{j}_\mu g) \rangle$ is added for reference (cf. section 4). The entrainment interfacial layer (EIL) is located in the cloud-top region and is a transition layer between cloudy and free tropospheric air (cf. section 3.2). Presented is the case $Sh_0 = 10$, $Sv_0 = 0$, and $Re_0 = 400$ at $z_*/\lambda = 16$.

Table 1: Simulation details: $Sh_0 = \Delta u/U_0$ defines the shear number; $Sv_0 = u_{\text{sed}}/U_0$ defines the sedimentation number; Sv_b defines the buoyancy sedimentation number [cf. Eq. (5)]; $Re_0 = (\lambda U_0)/\nu$ defines the reference Reynolds number; grid (a) corresponds to $2560^2 x 1408$; grid (b) to $5120^2 x 1792$; grid (c) to $5120^2 x 2048$; L_x is the horizontal domain size; λ is the extinction length (with $\lambda = 15$ m); Δu is the cloud-top velocity jump; η is the Kolmogorov scale; z_* is the convective length scale; w_* is the convective velocity scale; h_{EIL} is the thickness of the EIL; $Ri_* = z_*\Delta b/w_*^2$ is the convective Richardson number; and $Ri_{Sh_0} = h_{\text{EIL}}/(3h_{Sh_0}) = h_{\text{EIL}}\Delta b/(\Delta u)^2$ is the shear Richardson number. The value of z_* indicates the final time considered in the analysis (cf. section 2.2) and all other time dependent variables [column 10-13] are averaged over the period $10 < z_*/\lambda < 12$ for $Re_0 = 400$ and over the period $7.5 < z_*/\lambda < 8.5$ for $Re_0 > 400$.

Sh_0	Sv_0	Sv_b	Re_0	Grid	L_x/λ	Δu ms^{-1}	η cm	z_* m	w_* ms^{-1}	h_{EIL} m	Ri_*	Ri_{Sh_0}
0	0.0	0.0	400	a	54	0.0	22	180	0.61	8.5	109	-
0	0.0	0.0	400	b	108	0.0	22	240	0.60	8.4	113	-
0	0.043	0.064	400	a	54	0.0	22	180	0.61	9.4	113	-
0	0.1	0.15	400	a	54	0.0	23	180	0.58	11.3	124	-
5	0.0	0.0	400	a	54	1.5	21	180	0.61	9.2	109	1.0
5	0.043	0.064	400	a	54	1.5	22	180	0.59	10.3	118	1.1
5	0.1	0.15	400	a	54	1.5	23	180	0.58	12.1	120	1.3
10	0.0	0.0	400	a	54	3.1	20	180	0.62	13.8	106	0.4
10	0.0	0.0	400	b	108	3.1	20	240	0.62	14.0	107	0.4
10	0.043	0.064	400	a	54	3.1	21	180	0.60	14.2	113	0.4
10	0.1	0.15	400	a	54	3.1	22	180	0.57	14.8	122	0.4
0	0.0	0.0	1200	c	54	0.0	10	130	0.53	4.6	105	-
10	0.0	0.0	800	c	54	3.1	12	130	0.54	10.4	100	0.3
10	0.1	0.15	800	c	54	3.1	13	130	0.49	11.5	119	0.3

with sizes of the order of the boundary-layer depth, it allows resolving the meter- and submeter-scale mixing processes that are important for sedimentation and shear effects on cloud-top entrainment (cf. Table 1), complementing thereby previous LES studies where typical grid spacings are on the order of several meters (Mellado et al., 2018).

The formulation of the CTML is identical to the one used in Lozar and Mellado (2017), where sedimentation effects alone are studied by means of DNS. Here, we extend this work by additionally imposing wind shear. Droplet-sedimentation effects are represented by means of a bulk microphysics scheme which is similar to previous LES studies by Ackerman et al. (2004) and Bretherton, Blossey, and Uchida (2007). Besides, inertial effects are neglected, since they are negligibly small for the conditions considered in this study (Lozar and Mellado, 2014; Mellado, 2017). For conciseness, the formulation of the CTML is provided in Lozar and Mellado (2014) and Lozar and Mellado (2017), and this section only includes the discussion of the relevant nondimensional parameters and variables that are needed for the discussion of the results. A nondimensional formulation proves convenient to reduce the degrees of freedom in the parameter space that defines the problem and avoid redundancy of numerical experiments, to facilitate the generalization of results to other physical conditions, as well as to gain some a priori insight into the relative importance of the different processes considered in the study.

2.1 Dimensional analysis

The liquid-water mass flux due to the gravitational settling of the cloud droplets, or sedimentation flux, can be written as (cf., Lozar and Mellado, 2014; Lozar and Mellado, 2017)

$$\rho \mathbf{j}_\mu = -\pi (108\mu_g)^{-1} \rho_\ell^2 N_d \overline{d^5} g \mathbf{k}, \tag{1}$$

where, ρ is the density of the fluid, μ_g is the dynamic viscosity of the environmental air, ρ_ℓ is the density of liquid water, N_d is the droplet number density, $\overline{d^n}$ is the n-th moment of the droplet-size distribution (DSD), g is the magnitude of the gravitational acceleration, and $\mathbf{k}$ is a unit vector pointing upwards in the vertical direction. The dependence of the sedimentation flux on the DSD fifth moment results from the product of the mass of the droplet, proportional to the droplet's volume, and the Stokes terminal velocity, proportional to the droplet's area. This dependence indicates the importance of the large droplets, or the tail of the DSD. The sedimentation flux appears in the evolution equations of the total specific humidity q_t and the specific enthalpy h (Lozar and Mellado, 2017). In addition, the sedimentation flux changes the density field and thus introduces a sedimentation buoyancy flux $-\mathbf{j}_\mu g$ in the evolution equation of the buoyancy, which is an important contribution to the entrainment velocity, as discussed in Section 4.

In the bulk microphysics scheme employed here, we follow previous work and assume a log-normal DSD and a constant droplet number density N_d (cf., Ackerman et al., 2004; Bretherton, Blossey, and Uchida, 2007; Lozar and Mellado, 2014; Lozar and Mellado, 2017). With this assumption and the Boussinesq approximation, the sedimentation flux per unit mass can be written as

$$\mathbf{j}_\mu = -q_\ell^c u_{\text{sed}} \left(\frac{q_\ell}{q_\ell^c} \right)^{5/3} \mathbf{k}, \tag{2}$$

where q_ℓ^c denotes the liquid water specific humidity of cloudy air, and

$$u_{\text{sed}} = g[(\rho_\ell d_v^2)/(18\mu_g)] \exp[5(\log \sigma_{\text{gc}})^2] \tag{3}$$

is a bulk sedimentation velocity. The volume-mean droplet diameter in the cloud is defined as $d_v \equiv (\overline{d^3})^{1/3} = (6\rho^c q_\ell^c)^{1/3} (\pi \rho_\ell N_d)^{-1/3}$, where ρ^c denotes the density of cloudy air, and σ_{gc} is the geometric standard deviation of the log-normal DSD. A bulk value of the sedimentation velocity that includes the factor $\exp[5(\log \sigma_{\text{gc}})^2]$ is appropriate to represent the effect of the whole DSD and not only of one particular droplet size such as d_v, which is important because larger droplets contribute significantly to the sedimentation flux.

According to Eq. (2), the sedimentation flux can be fully characterized by two non-dimensional parameters, namely, one related to the bulk settling velocity describing how fast the droplets fall, and one related to the in-cloud liquid water content, i.e., how much liquid mass is being transported. As the first non-dimensional parameter, we consider the sedimentation number

$$Sv_o = \frac{u_{\text{sed}}}{U_o}, \tag{4}$$

where $U_o = (B_o \lambda)^{1/3}$ is a reference radiative velocity scale. In this definition, λ is the extinction length scale, which characterizes the depth over which the radiative flux divergence concentrates, and $B_o = R_o g/(\rho^c c_p^c T^c)$ is the reference buoyancy flux that is associated with the reference longwave radiative cooling R_o (Lozar and Mellado, 2017; Mellado, 2017). In the definition of B_o, c_p^c and T^c are the specific heat capacity and temperature of cloudy air, respectively. Equation (4) illustrates the advantage of using nondimensional numbers, as a single sedimentation number Sv_o characterizes various ratios of u_{sed} and U_o. As the second non-dimensional parameter, we consider
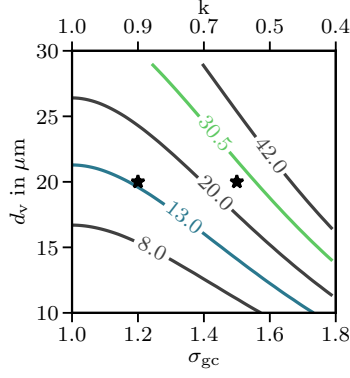
$$Sv_b = \frac{q_\ell^c u_{\text{sed}} g}{\beta B_o}, \tag{5}$$

Figure 2: Contour plot of the bulk sedimentation velocity u_{sed} in mm s^{-1} as function of the volume-mean droplet diameter d_{v} and the geometric standard deviation σ_{gc}. The second horizontal axis at the top shows the related value of $k = (d_{\mathrm{v}}/d_{\mathrm{e}})^3 = \exp[-3(\ln \sigma_{\mathrm{gc}})^2]$, where $d_{\mathrm{e}} = \overline{d^3}/\overline{d^2}$ is the droplet effective diameter. The blue contour line corresponds to $Sv_{\mathrm{o}} = 0.043$ and the green contour line to $Sv_{\mathrm{o}} = 0.1$ for RF01 of DYCOMS-II. The two black stars correspond to the reference cases $\{\sigma_{\mathrm{gc}} \simeq 1.2, d_{\mathrm{v}} \simeq 20\,\mathrm{\tilde{}m}\}$ and $\{\sigma_{\mathrm{gc}} \simeq 1.5, d_{\mathrm{v}} \simeq 20\,\mathrm{\tilde{}m}\}$ discussed in the text.

which characterizes the sedimentation buoyancy flux (cf. Lozar and Mellado, 2017) and which directly appears in the entrainment-rate equation discussed in Section 4. The parameter β is the fraction of radiatively induced enthalpy changes that translate into buoyancy changes.

Cloud-top wind shear is characterized by the shear number

$$Sh_{\mathrm{o}} = \frac{\Delta u}{U_{\mathrm{o}}} \, , \tag{6}$$

where $\Delta u = ||\mathbf{u}^{\mathrm{d}} - \mathbf{u}^{\mathrm{c}}||$ defines a constant jump of the horizontal velocity, with $\mathbf{u}^{\mathrm{d}}$ and $\mathbf{u}^{\mathrm{c}}$ being the mean horizontal velocity vectors in the dry free troposphere and within the cloud, respectively (a superscript 'd' indicates dry free tropospheric air). The parameter Sh_{o} completely characterizes wind-shear effects in the CTML since we can always choose a reference frame which moves with the mean velocity $(\mathbf{u}^{\mathrm{d}} + \mathbf{u}^{\mathrm{c}})/2$, and which is aligned with the vector $\mathbf{u}^{\mathrm{d}} - \mathbf{u}^{\mathrm{c}}$.

In the phase equilibrium formulation adopted here, the buoyancy reversal parameter D, the mixture fraction at saturation conditions χ_{sat}, and the parameter β introduced in Eq. (5) completely characterize the effect of phase changes in the water substance (cf. Lozar and Mellado, 2017). The buoyancy reversal parameter is defined as $D = -b_{\mathrm{sat}}/\Delta b$, i.e., the ratio of the buoyancy at saturation conditions b_{sat} to the buoyancy jump across the cloud-top $\Delta b = b^{\mathrm{d}} - b^{\mathrm{c}}$. Atmospheric conditions in which $D > 0$, such as in the simulations performed in this study, allow for buoyancy reversal instability (Randall, 1980; Deardorff, 1980a).

This set of nondimensional numbers is completed by a reference Richardson number $Ri_{\mathrm{o}} = \lambda \Delta b/U_{\mathrm{o}}^2$, which characterizes the strength of the inversion against eddies of size λ, and reference Reynolds number $Re_{\mathrm{o}} = \lambda U_{\mathrm{o}}/\nu$, which characterizes molecular diffusive effects. In summary, the set of nondimensional numbers $\{Sv_{\mathrm{o}}, Sv_b, Sh_{\mathrm{o}}, D, \chi_{\mathrm{sat}}, \beta, Ri_{\mathrm{o}}, Re_{\mathrm{o}}\}$ completely characterizes the CTML (see Table 1).

2.2 Description of simulations

To assess the effect of droplet sedimentation and wind shear on cloud-top entrainment, we fix all parameters according to the first research flight (RF01) of the DYCOMS-II flight campaign and vary only the sedimentation number Sv_{o} and the shear number Sh_{o}. Major reference parameters for RF01 of DYCOMS-II are summarized in Table 2.

These parameters are representative of subtropical conditions, where substantial jumps in total-water specific humidity Δq_t and temperature ΔT are commonly found across the cloud top.

Regarding sedimentation effects, we investigate three cases, namely, a no-sedimentation case ($Sv_o = 0$), a moderate sedimentation case ($Sv_o = 0.043$), and a strong sedimentation case ($Sv_o = 0.1$), as summarized in Table 1. Figure 2 presents contour plots of u_{sed} as a function of the volume-mean droplet diameter d_v and as a function of the geometric standard deviation σ_{gc}. Droplet diameters are typically reported to be in the range range of $10 - 30\,\bar{}\,m$ (Martin, Johnson, and Spice, 1994; VanZanten et al., 2005; Haman et al., 2007; Ackerman et al., 2009; Katzwinkel, Siebert, and Shaw, 2012; Glienke et al., 2017; Grosvenor et al., 2018) and the geometric standard deviation is reported to be in the range $\sigma_{gc} \simeq 1 - 2$ with the most probable value being on the order of $\sigma_{gc} \simeq 1.2 - 1.5$ (Martin, Johnson, and Spice, 1994; Hudson and Yum, 1997; Miles, Verlinde, and Clothiaux, 2000; Wood, 2000; Pawlowska and Brenguier, 2000; Ackerman et al., 2004; VanZanten et al., 2005; Bretherton, Blossey, and Uchida, 2007; Grosvenor et al., 2018). For RF01 of DYCOMS-II one finds $d_v \simeq 20\,\bar{}\,m$ (that is $N_d = 140\,cm^{-1}$) and $\sigma_{gc} = 1.2$ as most probable values (VanZanten et al., 2005; Bretherton, Blossey, and Uchida, 2007), even though Ackerman et al. (2004) used $\sigma_{gc} = 1.5$ for the very same case. The cases $Sv_o = 0.043$ and $Sv_o = 0.1$ are designed to investigate this sensitivity in σ_{gc}, where $Sv_o = 0.043$ approximates the pair $\{d_v \simeq 20\,\bar{}\,m, \sigma_{gc} = 1.2\}$ and $Sv_o = 0.1$ the pair $\{d_v \simeq 20\,\bar{}\,m, \sigma_{gc} = 1.5\}$. According to Eq. (4), these values correspond to a bulk sedimentation velocity of $u_{sed} \simeq 13\,mm\,s^{-1}$ and $u_{sed} \simeq 30.5\,mm\,s^{-1}$. The exponential factor in Eq. (3) explains why these values are larger than the sedimentation velocities obtained for single droplets, which are typically on the order of $3\,mm\,s^{-1} - 12\,mm\,s^{-1}$ (e.g. Mellado, 2017).

Regarding the second settling parameter, one finds $Sv_b \simeq 1.5\,Sv_o$ for RF01 of DYCOMS II (cf. Table 1). According to Eq. (5), an estimate for the corresponding magnitude of the sedimentation buoyancy flux $-\mathbf{j}_\mu g$ is $0.06 - 0.15 \times 10^{-3}\,m^2 s^{-3}$. This estimate shows that the sedimentation buoyancy flux can be a 20% contribution to the entrainment buoyancy flux, which is estimated as $w_e \Delta b \simeq 0.75 \times 10^{-3}\,m^2 s^{-3}$ when using an entrainment velocity of $3\,mm\,s^{-1}$ and a buoyancy jump of $0.25\,m\,s^{-2}$ (see Appendix C). This estimate already indicates that the sedimentation buoyancy flux can significantly alter entrainment rates.

To determine the sensitivity of cloud-top entrainment to wind shear, we vary the shear number Sh_o for each value of Sv_o. Again three cases are investigated: A no-shear case ($Sh_o = 0$), a moderate shear case ($Sh_o = 5$), and a strong shear case ($Sh_o = 10$), as summarized in Table 1. These shear numbers correspond to cloud-top velocity jumps in the range of $\Delta u = 0 - 3.1\,m\,s^{-1}$. The largest jump of $\Delta u = 3.1\,m\,s^{-1}$ represents typical atmospheric conditions, as most cloud-top velocity jumps are reported to be on the order of $\Delta u = 4\,m\,s^{-1}$, although extreme values of up to $\Delta u = 10\,m\,s^{-1}$ have occasionally been observed (Brost, Wyngaard, and Lenschow, 1982; Nicholls and Leighton, 1986; Faloona et al., 2005; Roode and Wang, 2007; Katzwinkel, Siebert, and Shaw, 2012; Malinowski et al., 2013).

This discussion shows that we match all parameters of RF01 of DYCOMS-II except the Reynolds number, which implies that we need to investigate the sensitivity of our results to changes in the Reynolds number. Sensitivity studies presented in Appendix A reveal that the properties discussed in this paper depend only weakly on the Reynolds number, in particular, increasing the Reynolds number by a factor of two changes the mean entrainment velocity (defined in Equation (12)) by less than 20%. These findings indicates that we start to reach Reynolds numbers that are large enough to observe some degree of Reynolds number similarity (Dimotakis, 2005; Mellado et al., 2018), which justifies the use of DNS for studying some aspects of cloud-top entrainment in stratocumulus.

The grid spacing is isotropic and uniform within the region where the turbulent flow develops. The ratio of the the grid spacing to the Kolmogorov scale η is approximately 1.5, which implies a grid spacing of 20 cm to 32 cm (depending on Re_o, see Table 1). With

Table 2: List of fixed reference parameters for RF01 of the DYCOMS-II campaign. In addition we set $\chi_{sat} = 0.09$, $\beta = 0.53$, $D = 0.031$, $T^c = 283.8\,\mathrm{K}$, and $q_\ell^c = 0.5\,\mathrm{g\,kg^{-1}}$ (cf. section 2). The reference buoyancy flux B_0 corresponds to a reference longwave radiative cooling of $R_0 = 70\,\mathrm{W\,m^{-2}}$.

U_0	$0.3\,\mathrm{m\,s^{-1}}$	reference velocity scale
B_0	$1.9 \times 10^{-3}\,\mathrm{m^2\,s^{-3}}$	reference buoyancy flux
λ	$15\,\mathrm{m}$	extinction length
Δb	$0.25\,\mathrm{m\,s^{-2}}$	jump in buoyancy
Δq_t	$-7.5\,\mathrm{g\,kg^{-1}}$	jump in total-water specific humidity
ΔT	$8.5\,\mathrm{K}$	jump in temperature
Ri_0	40.2	reference Richardson number

this configuration we reach submeter-scale resolution since the compact schemes used in this study allow representing the transfer function of first-derivative operators with a 99% accuracy using 4 grid points per wavelength (e.g., see the numerical analysis in Lele (1992)). In addition, the ratio of the horizontal domain size L_x to the convective length scale z_* needs to be large enough for our results to become independent of L_x (Bailon-Cuba, Emran, and Schumacher, 2010; Mellado, 2012). The convective length scale z_* characterizes the vertical extent of the turbulent flow and is defined by Eq. (7) and further explained in section 3.1. The ratio L_x/z_* diminishes as z_* grows in time, and at the end of our simulations we reach $L_x/z_* \simeq 4.5$ for grid (a) and $L_x/z_* \simeq 6.5$ for grid (b) and (c). A sensitivity study based on the cases $\{Sh_0 = 0, Sv_0 = 0\}$ and $\{Sh_0 = 10, Sv_0 = 0\}$ shows that the ratio of $L_x/z_* \simeq 4.5$ is sufficient for the statistics that we study to become approximately independent of L_x. This result is obtained by observing that statistics at $z_*/\lambda \simeq 12$ using grid (a), where $L_x/z_* \simeq 4.5$, are similar to those obtained using grid (b), where $L_x/z_* \simeq 9$. Using grid (b) improves the statistical convergence when considering the temporal evolution of horizontal averages, and it allows us to run the simulations over a longer interval of z_*/λ, which proves convenient for studying scaling laws. The cases with the large grids, namely grid (b) and (c), are computationally very expensive and for that reason we only run them up to $L_x/z_* \simeq 6.5$, which corresponds to $z_* \simeq 240\,\mathrm{m}$ for grid (b) and to $z_* \simeq 130\,\mathrm{m}$ for grid (c). Further details regarding the simulations are given in Mellado, Stevens, and Schmidt (2014) and Lozar and Mellado (2015b, 2017) and further details regarding the numerical algorithm are given in Mellado (2010) and Mellado and Ansorge (2012).

3 DROPLET-SEDIMENTATION AND WIND-SHEAR EFFECTS ON THE VERTICAL STRUCTURE

This section characterizes in-cloud properties of the performed simulations by introducing convective scalings, and characterizes cloud-top properties by discussing droplet-sedimentation and wind-shear effects on the entrainment interfacial layer (EIL). We show that droplet sedimentation and wind shear can alter cloud-top properties—like the thickness of the EIL—without significantly changing in-cloud properties further below.

3.1 *In-cloud convective scalings*

In stratocumulus, turbulence is generated within the cloud-top region by shear instabilities caused by the mean wind, and by convective instabilities caused by evaporative and

radiative cooling. The generation by wind shear tends to concentrate at the entrainment interfacial layer, a relatively thin region below which free convection prevails. This suggests to introduce convective scalings in the analysis, which can be based on a convective length scale

$$z_* = B_{\max}^{-1} \int_{z_{-\infty}}^{z_\infty} \mathcal{H}(B) dz, \tag{7}$$

and a convective velocity scale

$$w_* = (B_{\max} z_*)^{1/3}, \tag{8}$$

where $\mathcal{H}$ denotes the Heaviside function, $B = \langle w'b' \rangle$ is the turbulent buoyancy flux, and $B_{\max}$ its maximum within the cloud (Deardorff, 1980b; Mellado, Stevens, and Schmidt, 2014). The limits of integration are far enough below and above the cloud-top region for the result of the integration to not depend on them. The angle brackets $\langle \cdot \rangle$ indicate a horizontal average and an prime indicates fluctuations. Note that the definition of w_* deviates by a factor $2.5^{1/3} \simeq 1.4$ from previous work (Deardorff, 1980b; Wood, 2012). The reason is that the CTML does not retain the subcloud layer, where the linear vertical variation of the buoyancy flux justifies the factor of 2.5.

As turbulence propagates downwards the convective length scale z_* increases and we use this link between time and z_* to express the evolution of the system in terms of the nondimensional variable z_*/λ. This is convenient since the variable z_*/λ expresses the scale separation between the integral length scale z_*, associated with in-cloud turbulence, and the extinction length scale λ, associated with radiative cooling. An additional advantage of using z_*/λ is it is directly linked to the in-cloud turbulent intensity w_* by means of Eq. (8). In our simulations we typically reach values of $z_*/\lambda \simeq 12 - 16$ (cf. Table 1) and the initial transient takes roughly $z_*/\lambda \simeq 8$, i.e., statistics for different initial conditions usually deviate by less than 15% for $z_*/\lambda > 8$ (not shown). We therefore focus on the regime $z_*/\lambda > 8$ in our analysis. To improve statistical convergence, a running mean with the period $z_*/\lambda = 2$ is applied to all results presented in the main text.

We observe that w_* is in the range of $0.5 - 0.6 \, \mathrm{ms}^{-1}$ for all sedimentation and shear numbers investigated (cf. Table 2), which shows that w_* is insensitive towards changes in droplet sedimentation and wind shear. In other words, droplet-sedimentation and wind-shear effects can remain localized within the cloud-top region and do not necessarily change in-cloud properties (see Schulz and Mellado, 2018, for details).

3.2 *The entrainment interfacial layer*

The entrainment interfacial layer (EIL) refers to the region where warm and dry air from the free troposphere is mixed with cold and moist air from the cloud interior, and thus defines a transition layer between the cloud and the free troposphere. (Part of the mixing takes place below the EIL as free-tropospheric air is transported deep into the cloud interior through cloud holes, as observed in Figure 3 and as thoroughly studied by Gerber et al. (2005) and Gerber, Malinowski, and Jonsson (2016), but we do not focus on these cloud holes in the current analysis.) This implies that the EIL is characterized by strong vertical variations in temperature, buoyancy, and liquid water specific humidity. We follow previous work by Schulz and Mellado (2018) and define the EIL thickness, h_{EIL}, as

$$h_{\mathrm{EIL}} = z_{0.9\Delta b} - z_{\mathrm{i,n}}, \tag{9}$$

where $z_{0.9\Delta b}$ is the height where the mean buoyancy $\langle b \rangle$ reaches 90% of Δb and $z_{\mathrm{i,n}}$ denotes the height of zero mean buoyancy. With this definition the EIL is stably stratified and approximately coincides with the region where the turbulent buoyancy flux is negative (see Figure 3a). Our definition of the EIL closely follows the definition by Caughey, Crease, and Roach (1982) as the layer containing the majority of the temperature jump

(buoyancy in our case), and $z_{i,n}$ can be interpreted as the base of the capping inversion. However, our definition of the EIL differs from the definition proposed by Malinowski et al. (2013), especially regarding the lower boundary of the EIL, and this difference has to be taken into account when comparing results.

Our simulations show that droplet sedimentation and wind shear thicken the EIL. Sedimentation thickens the EIL by removing cloudy air from the EIL thus leaving behind warmer and dryer air. As a consequence, the mean buoyancy profile deforms in such a way that $z_{i,n}$ moves downward with respect to $z_{0.9\Delta b}$, which thickens the EIL. However, the sedimentation induced thickening of the EIL remains moderate, namely h_{EIL} increases by $\sim 30\%$ when the sedimentation number is increased from $Sv_0 = 0$ to $Sv_0 = 0.1$ for $Sh_0 = 0$ (see Table 1).

The shear induced thickening of the EIL can be substantially stronger but is only observed once the cloud-top velocity jump exceeds its critical value $(\Delta u)_{crit}$ (see Eq. (11)). According to Table 2, a strong shear with $Sh_0 \simeq 10$ thickens the EIL by $\sim 70\%$ for $Sv_0 = 0.0$, while a weak shear with $Sh_0 = 5$ does not significantly thicken the EIL for $Sv_0 = 0.0$. The reason for this is that in the case $Sh_0 = 5$ the width of the shear production term $P = -\langle u'w' \rangle \partial_z \langle u \rangle$ is small compared to h_{EIL}, while h_{EIL} is proportional to the width of the shear production term for the case $Sh_0 = 10$. By comparing these two length scales a critical cloud-top velocity jump $(\Delta u)_{crit}$ is derived in Schulz and Mellado (2018), where shear effects are argued to be significant for $\Delta u > (\Delta u)_{crit}$ and negligible to leading order for $\Delta u < (\Delta u)_{crit}$. This critical cloud-top velocity jump is defined as

$$(\Delta u)_{crit} \simeq \sqrt{\frac{3\alpha_1}{2\alpha_3^{-1} - 3\alpha_2}} w_* , \tag{10}$$

where w_* is the convective velocity defined in Eq. (8). The parameters α_1 and α_2 determine the amount of kinetic energy associated with an air parcel penetrating into the stably stratified EIL, while the parameter α_3 is related to the EIL thickness h_{EIL}, as discussed in Appendix B. We find that sedimentation modifies the set of parameters $\{\alpha_1, \alpha_2, \alpha_3\}$ only mildly, changing from $\{4.7, 0.60, 0.75\}$ for $Sv_0 = 0.0$, to $\{4.8, 0.56, 0.84\}$ for $Sv_0 = 0.043$, and to $\{5.5, 0.55, 0.90\}$ for $Sv_0 = 0.1$. Substituting these parameters into Eq. (10) yields a critical shear velocity in the range of

$$(\Delta u)_{crit} = 4 - 5w_* , \tag{11}$$

where the lower limit of $4w_*$ corresponds to $Sv_0 = 0.0$ and the upper limit of $5w_*$ to $Sv_0 = 0.1$. Hence, droplet-sedimentation effects on the critical cloud-top velocity jump $(\Delta u)_{crit}$ remain moderate, below 25%. Typical values of w_* are in the range $w_* \simeq 0.2 - 0.9\,\mathrm{m\,s^{-1}}$ (Wood, 2012), which implies typical critical velocity jumps in the range $(\Delta u)_{crit} \simeq 1 - 4\,\mathrm{m\,s^{-1}}$. We reach $w_* \simeq 0.6\,\mathrm{m\,s^{-1}}$ at the end of the simulations (cf. Table 1), which corresponds to $(\Delta u)_{crit} = 2.4 - 3.0\,\mathrm{m\,s^{-1}}$. Therefore, only the strongest velocity jump with $\Delta u \simeq 3.1\,\mathrm{m\,s^{-1}}$ ($Sh_0 = 10$) exceeds the critical shear velocity $(\Delta u)_{crit}$, which explains why shear effects in Figure 3, 5, 6 are observed to be negligible for $\Delta u \lesssim 1.5\,\mathrm{m\,s^{-1}}$ ($Sh_0 \lesssim 5$).

We further find that sedimentation-induced and shear-induced broadening of the EIL are not additive but partially compensate each other. As indicated in Table 1, imposing a strong shear broadens the EIL by ~ 6 m compared to the no-shear case, and imposing a strong sedimentation broadens the EIL by ~ 3 m compared to the no-sedimentation case, but simultaneously imposing a strong shear and a strong sedimentation broadens the EIL only by ~ 7 m compared to the no-shear and no-sedimentation case. To understand this behavior, recall that for a sufficiently strong shear such as $Sh_0 = 10$ the EIL thickness is proportional to the width of the shear production term. According to Figure 3, sedimentation significantly weakens the shear production term, thus diminishing the shear induced thickening of h_{EIL} to approximately ~ 7 m instead of $\sim 6\,\mathrm{m} + 3\,\mathrm{m} = 9\,\mathrm{m}$. As
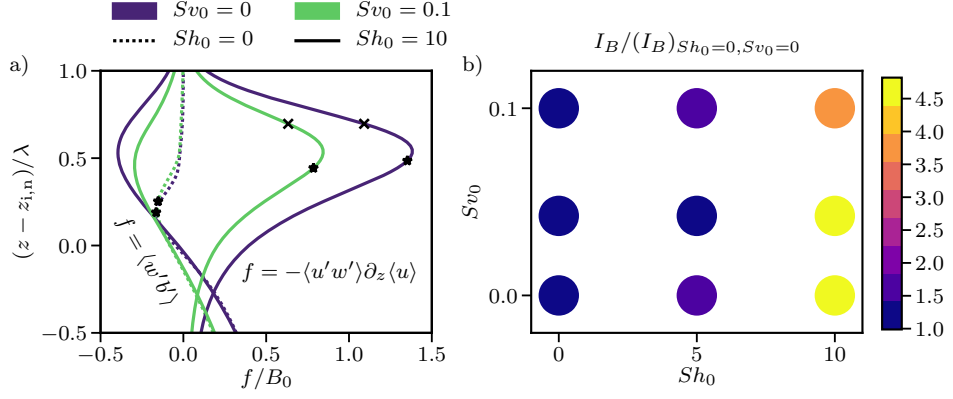
Figure 3: (Panel a) normalized turbulent buoyancy flux and normalized shear production term, where the different symbols indicate different reference heights: The star indicates the height of minimum turbulent buoyancy flux $z_{i,f}$, the cross the height of the maximum gradient of the mean buoyancy profile $z_{i,g}$, and the vertical distance z is plotted with respect to the height of zero mean buoyancy $z_{i,n}$. Colors indicate sedimentation numbers Sv_0 and line styles shear number Sh_0, e.g., the dashed green line indicates the pair $\{Sv_0 = 0.1, Sh_0 = 0\}$. (Panel b) normalized rate of net TKE consumption for entrainment, where I_B is defined as $I_B = \int_{z_{-\infty}}^{z_{+\infty}} B\mathcal{H}(-B)dz$ and $B = \langle w'b' \rangle$. Both figures are presented for $Re_0 = 400$ at $z_*/\lambda \simeq 11$

argued in detail in Appendix B, this compensating effect of sedimentation and shear on the EIL thickness h_{EIL} helps to explain why sedimentation effects on the critical velocity jump $(\Delta u)_{\text{crit}}$ remain moderate.

4 DROPLET-SEDIMENTATION AND WIND-SHEAR EFFECTS ON THE ENTRAINMENT VELOCITY

This section investigates the combined effect of droplet sedimentation and wind shear on the various contributions to the mean entrainment velocity w_e from mixing, radiative cooling, and evaporative cooling. This analysis provides evidence to our initial claim that droplet-sedimentation and wind-shear effects on the mean entrainment velocity w_e can compensate each other.

4.1 *Mean entrainment velocity*

Following Lilly (1968), we define the mean entrainment velocity as

$$w_e = \frac{dz_i}{dt} - \langle w \rangle_{z_i},\tag{12}$$

where z_i defines a reference height marking the cloud-top region, $\langle w \rangle_{z_i}$ is a mean vertical velocity, and a subscript z_i indicates that the corresponding quantity is evaluated at z_i. The choice of z_i is arbitrary and different definitions of z_i have been proposed in literature (e.g., Malinowski et al., 2013; Schulz and Mellado, 2018). Here we consider three reference heights: The height of zero mean buoyancy $z_{i,n}$, the height of minimum turbulent buoyancy flux $z_{i,f}$, and the height of maximum gradient of the mean buoyancy profile $z_{i,g}$. According to Eq. (9) the reference height $z_{i,n}$ coincides with the lower end of the EIL, while the reference height $z_{i,g}$ is located near to the upper end of the EIL (not shown). These different references heights are only separated by a few meters, namely, $z_{i,n}$ lies $7\,\text{m} - 10\,\text{m}$ below $z_{i,f}$, which in turn lies $3\,\text{m} - 6\,\text{m}$ below $z_{i,g}$, as indicated in Figure 4 (with $\lambda \simeq 15\,\text{m}$). In agreement with previous work by Schulz and Mellado
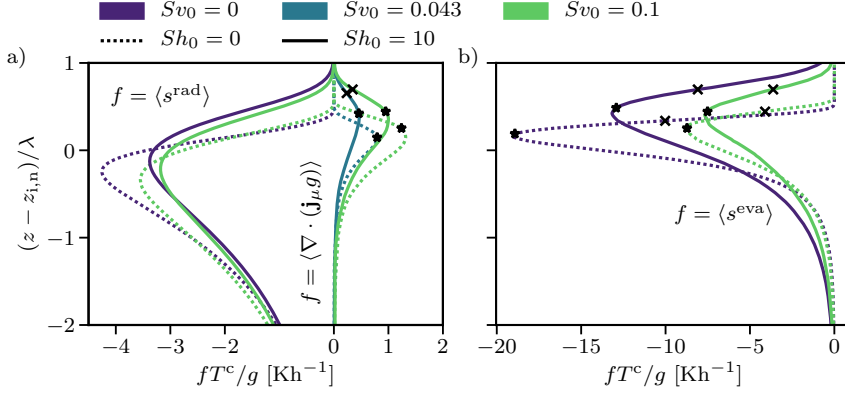
Figure 4: Mean profiles of the different buoyancy source terms according to Eq. (13), where the different symbols indicate different reference heights: The star indicates the height of minimum turbulent buoyancy flux $z_{i,f}$, and the cross the height of the maximum gradient of the mean buoyancy profile $z_{i,g}$. The vertical distance z is plotted with respect to the height of zero mean buoyancy, $z_{i,n}$, and the figure is presented for $Re_o = 400$ at $z_*/\lambda \simeq 11$

(2018) we show below that these small height differences are crucial for some quantities while being negligible for others.

Droplet-sedimentation and wind-shear effects on the mean entrainment velocity are analyzed in more detail by means of the entrainment rate equation, which analytically relates w_e to the sum of six contributions. The entrainment rate equation is obtained by integrating the buoyancy evolution equation

$$D_t b = \kappa_T \nabla^2 b + \nabla \cdot (\mathbf{j}_\mu g) + s^{\mathrm{rad}} + s^{\mathrm{eva}} \ , \tag{13}$$

from an arbitrary reference height $z = z_i$ upwards, where κ_T denotes the thermal diffusivity and the second term defines a sedimentation buoyancy flux contribution. The radiative source term s^{rad} and the evaporative source term s^{eva} are defined in Appendix C. One obtains

$$w_e = w_e^{\mathrm{tur}} + w_e^{\mathrm{sed}} + w_e^{\mathrm{eva}} + w_e^{\mathrm{rad}} + w_e^{\mathrm{mol}} + w_e^{\mathrm{def}} \ . \tag{14}$$

For conciseness, the exact definition of each contribution are provided in Appendix C and only some main aspects of them are discussed here. The turbulent buoyancy flux contribution, w_e^{tur}, is proportional to the turbulent buoyancy flux $-\langle w'b'\rangle_{z_i}$. The sedimentation buoyancy flux contribution, w_e^{sed}, is proportional to the sedimentation buoyancy flux $\langle \mathbf{j}_\mu g \cdot \mathbf{k}\rangle_{z_i}$. The evaporative cooling contribution, w_e^{eva}, is proportional to $E_o - \langle E\rangle_{z_i}$, the difference between the net (or integrated, or accumulated) evaporative cooling across the whole cloud-top region

$$E_o = \int_{z_{-\infty}}^{z_\infty} \langle s^{\mathrm{eva}}\rangle dz \ , \tag{15}$$

and the integrated evaporative cooling up to z_i, $\langle E\rangle_{z_i} = \int_{z_{-\infty}}^{z_i} \langle s^{\mathrm{eva}}\rangle dz$. Likewise, the radiative contribution, w_e^{rad}, is proportional to $\beta(R_o - \langle R\rangle_{z_i})$, the difference of the net radiative flux above the cloud-top, R_o, and its value at z_i, $\langle R\rangle_{z_i}$, where the parameter β accounts for condensational warming effects (cf. section 2.1). Furthermore, w_e^{mol} denotes the molecular flux contributions and w_e^{def} the deformation contribution, where the latter describes temporal changes in the shape of the mean buoyancy profile. In the subsequent analysis, all contributions to the mean entrainment velocity w_e are normalized by the reference entrainment velocity scale $W_{\mathrm{ref}} = \beta B_o/\Delta b$, which is $W_{\mathrm{ref}} \simeq 4\,\mathrm{mm\,s}^{-1}$ for RF01 of the DYCOMS-II field campaign considered here.
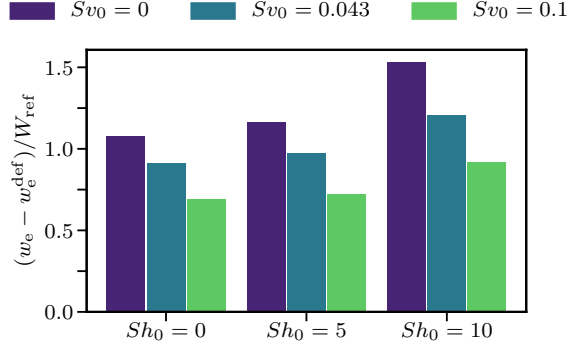
Figure 5: Normalized quasi-steady entrainment velocity $w_e - w_e^{\text{def}}$ [see Eq. (14)] evaluated at the height of zero mean buoyancy $z_{i,n}$ for $Re_0 = 400$ at $z_*/\lambda \simeq 11$. For each triplet the shear number Sh_0 is fixed and the sedimentation number Sv_0 is varied.

Before discussing the combined effect of droplet-sedimentation and wind-shear on the mean entrainment velocity, we need to elaborate on three aspects. Firstly, although the net evaporative and radiative cooling rates are commensurate with each other (E_0 approximately varies between $0.5\,\beta B_0$ and $1.5\,\beta B_0$ for all cases considered in this study), the vertical distribution of those cooling rates varies substantially with height. As observed in Figure 4, the profile of the evaporative cooling rate $\langle s^{\text{eva}} \rangle$ concentrates around the EIL whereas the profile of the radiative cooling rate $\langle s^{\text{rad}} \rangle$ penetrates deeper in the cloud. Hence, the evaporative cooling contribution to the mean entrainment velocity is significantly larger than the radiative contribution for the reference heights that we use in this study, where we focus on the EIL, but this should not be interpreted as radiative cooling effects being negligible.

Second, the simulated entrainment velocities agree well with measurements. According to Figure 5 the quasi-steady entrainment velocity is approximately $4.5\,\text{mm}\,\text{s}^{-1}$ and is thus commensurate with measurements of RF01 of DYCOMS-II, which report entrainment velocities in the range of $3.9\,\text{mm}\,\text{s}^{-1} - 4.7\,\text{mm}\,\text{s}^{-1}$ (Stevens et al., 2003; Faloona et al., 2005). The quasi-steady entrainment velocity $w_e - w_e^{\text{def}} = w_e^{\text{tur}} + w_e^{\text{sed}} + w_e^{\text{eva}} + w_e^{\text{rad}} + w_e^{\text{mol}}$ ignores unsteady effects (characterized by w_e^{def}) and thus characterizes the cloud in a quasi-steady state, which is by definition a state where w_e^{def} is small compared to $w_e^{\text{tur}} + w_e^{\text{sed}} + w_e^{\text{eva}} + w_e^{\text{rad}} + w_e^{\text{mol}}$ (Schulz and Mellado, 2018). Measurements campaigns are often performed within a quasi-steady state and therefore the quasi-steady entrainment velocity is used for comparison. An additional advantage of using the quasi-steady entrainment velocity is that its magnitude is insensitive towards the choice of the reference height z_i, even though the individual entrainment velocity contributions can depend strongly on the choice of the reference height z_i as elucidated in Schulz and Mellado (2018).

Third, previous work by Lozar and Mellado (2017) and Schulz and Mellado (2018) has shown that changes of w_e with droplet sedimentation and wind shear separately, i.e., $\partial w_e / \partial u_{\text{sed}}$ and $\partial w_e / \partial \Delta u$, show little dependence on the low-to-moderate Reynolds numbers of the simulations, even though the magnitude of the molecular flux contribution w_e^{mol} can be comparable with the turbulent buoyancy flux contribution w_e^{tur}.

4.2 Competing effects of droplet sedimentation and wind shear on w_e

Figure 5 shows that droplet-sedimentation and wind-shear effects on the quasi-steady entrainment velocity can completely compensate each other. While imposing a strong wind shear with $Sh_0 = 10$ enhances the quasi-steady entrainment velocity $w_e - w_e^{\text{def}}$ by approximately $0.3 - 0.4\,W_{\text{ref}}$, with the interval indicating the dependence on the

sedimentation strength, sedimentation does the opposite and weakens the quasi-steady entrainment velocity $w_e - w_e^{def}$ by approximately $0.2 - 0.3\,W_{ref}$ for $Sv_o = 0.043$ and by $0.4 - 0.6\,W_{ref}$ for $Sv_o = 0.1$, with the interval indicating the dependence on the shear strength. Moreover, Figure 5 shows that droplet sedimentation and wind shear interact to a good approximation in an multiplicative way. For instance, strong sedimentation alone decreases w_e approximately by a factor of 0.6, while a strong shear alone increases w_e approximately by a factor of 1.4. This result suggests that combining sedimentation and shear would change w_e approximately by a factor of $1.4 \times 0.6 = 0.84$, and indeed Figure 5 reveals a factor of 0.8. (Although not shown, the same is true for the net evaporative cooling contribution E_o.) This multiplicative property might be useful for entrainment velocity parameterizations.

The preceding discussion indicates that sedimentation effects on the shear enhancement of entrainment remain moderate, namely, increasing the shear strength to $Sh_o = 10$ increases the quasi-steady entrainment velocity $w_e - w_e^{def}$ by approximately 40% for $Sv \leq 0.043$ and by approximately 30% for $Sv = 0.1$. Likewise, shear effects on the sedimentation weakening of entrainment are negligible to leading order, namely, $w_e - w_e^{def}$ decreases by approximately 20% if the sedimentation strength is increased to $Sv_o = 0.043$ and by approximately 40% if increased to $Sv_o = 0.1$ irrespective of the imposed shear strength. In addition, Figure 5 demonstrates that a moderate wind-shear $Sh_o = 5$ does not enhance the quasi-steady entrainment velocity, which confirms the critical cloud-top velocity jump $(\Delta u)_{crit}$ discussed in section 3.2. All this suggests that, if the shear enhancement is assumed to be linear within the range of Δu considered here, a shear on the order of $Sh_o = 8 - 9$ (that is $\Delta u \simeq 2.4 - 2.7\,\mathrm{m\,s^{-1}}$ for RF01 of DYCOMS-II) is needed to compensate the sedimentation-induced decrease of w_e associated with $Sv_o = 0.043$, while a shear on the order of $Sh_o = 12 - 13$ (that is $\Delta u \simeq 3.6 - 3.9\,\mathrm{m\,s^{-1}}$ for RF01 of DYCOMS-II) is needed to compensate the sedimentation-induced decrease of w_e associated with $Sv_o = 0.1$.

4.3 *Contributions to w_e from different cloud-top processes*

The various contributions to the mean entrainment velocity change with sedimentation and shear as indicated in Figure 6. Sedimentation and shear mainly alter three of the six contributions of the entrainment rate equation Eq. (14), namely the sedimentation buoyancy flux contribution w_e^{sed}, the turbulent buoyancy flux contribution w_e^{tur}, and the evaporative cooling contribution w_e^{eva}. Although sedimentation and shear effects on the radiative cooling contribution w_e^{rad} are small for RF01 of DYCOMS-II, this might not be the case under different thermodynamic conditions, e.g., smaller jumps in total-water specific humidity are expected to increase the importance of radiative cooling compared to evaporative cooling (Lozar and Mellado, 2015a). The subsequent analysis therefore focuses on the joint effect of sedimentation and shear on these four contributions. A thorough discussion of w_e^{mol} and w_e^{def} can be found in Schulz and Mellado (2018).

While droplet sedimentation promotes an upward sedimentation buoyancy flux that directly opposes entrainment, wind shear does the opposite and promotes a downward turbulent buoyancy flux that directly enhances entrainment, which implies that w_e^{sed} is a negative contribution to w_e in Eq. (14) while w_e^{tur} is a positive contribution to w_e. However, the extent to which these two contributions can compensate each other strongly depends on the choice of the reference height z_i where these contributions are evaluated. For instance, w_e^{sed} is comparable to w_e^{tur} for reference heights near to $z_{i,n}$ while w_e^{tur} dominates over w_e^{sed} for reference heights near to $z_{i,f}$ (see Figure 6a,c). This behavior is expected since the turbulent buoyancy flux contribution w_e^{tur} maximizes by definition near $z_{i,f}$, while q_ℓ and thus the sedimentation buoyancy flux contribution w_e^{sed} increases when lowering the reference height towards $z_{i,n}$. (For this reason Figure 6b,d shows two extreme cases of z_i.) Besides, note that even though w_e^{sed} seems to be small, it is
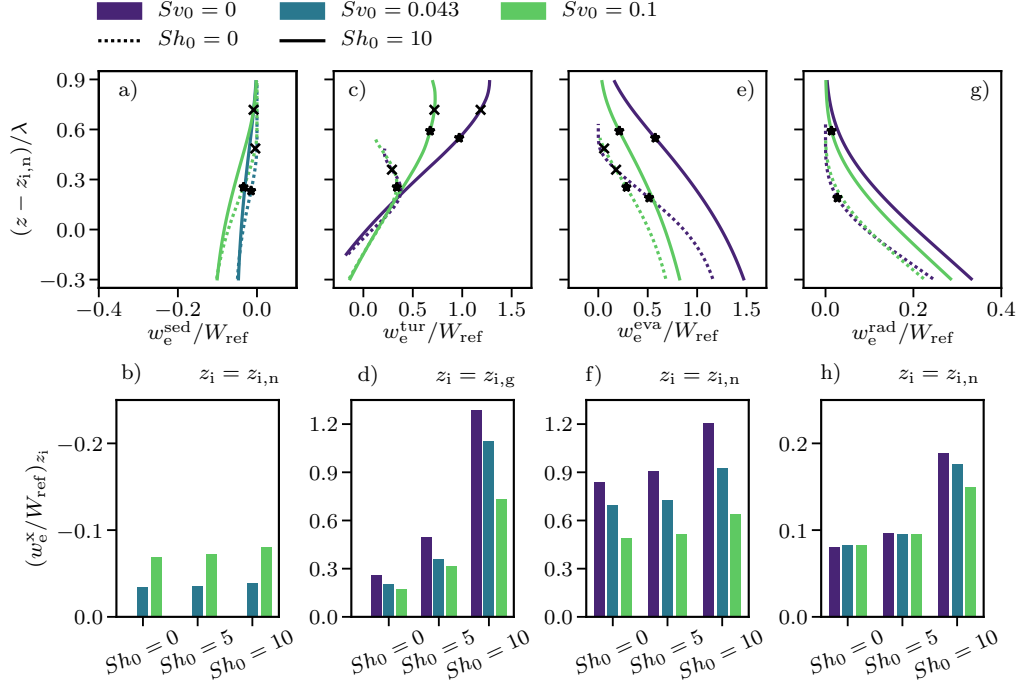
Figure 6: Different contributions to the mean entrainment velocity w_e according to Eq. (14), where the top row presents vertical profiles and the bottom row presents normalized values calculated at the reference height z_i. The stars and crosses in the top row indicate the height of minimum turbulent buoyancy flux $z_{i,f}$ and the height of the maximum gradient of the mean buoyancy profile $z_{i,g}$ respectively. The vertical distance z is plotted with respect to the height of zero mean buoyancy $z_{i,n}$. (Panels a + b) normalized sedimentation buoyancy flux contribution w_e^{sed}/W_{ref}, (panels c + d) normalized turbulent buoyancy flux contribution w_e^{tur}/W_{ref}, (panels e + f) normalized evaporative contribution w_e^{eva}/W_{ref}, and (panels g + h) normalized radiative contribution w_e^{rad}/W_{ref}. Note the different vertical scales in panel a,b,g,h. The figure is presented for $Re_0 = 400$ at $z_*/\lambda \simeq 11$.

a 20% contribution to the overall sedimentation reduction of w_e at $z_{i,n}$. Regarding the interaction of sedimentation and shear, Figure 6a-d shows that shear effects on w_e^{sed} remain weak, whereas sedimentation effects on w_e^{tur} increase with increasing shear as the sedimentation induced thickening of the EIL weakens the turbulent buoyancy flux around $z_{i,f}$ (cf. Figure 3a,b). All this shows that droplet sedimentation can act directly by promoting a significant sedimentation buoyancy flux contribution w_e^{sed} that opposes the turbulent buoyancy flux contribution w_e^{tur}, and can act indirectly by weakening the turbulent buoyancy flux contribution w_e^{tur}.

We further find that droplet-sedimentation and wind-shear effects on the evaporative cooling contribution w_e^{eva} can completely compensate each other. While droplet sedimentation removes cloudy air from the EIL, which prevents cloud droplets from evaporating and thus weakens w_e^{eva}, a sufficiently strong shear with $\Delta u > (\Delta u)_{crit}$ does the opposite and amplifies the mixing of environmental and cloudy air, which enhances evaporation in the EIL and thus enhances w_e^{eva} (e.g., Ackerman et al., 2004, 2009; Bretherton, Blossey, and Uchida, 2007; Mellado, Stevens, and Schmidt, 2014; Lozar and Mellado, 2017; Schulz and Mellado, 2018). This compensating effect of sedimentation and shear on w_e^{eva} is especially important for reference heights located near $z_{i,n}$ since w_e^{eva} is the dominant contribution to the mean entrainment velocity w_e for such reference heights. (w_e^{eva} decays rapidly for reference heights above $z_{i,n}$ and w_e^{tur} is equally or more important than w_e^{eva} at $z_{i,f}$.) Particularized to $z_{i,n}$ Figure 6e,f shows that imposing a strong sedimentation flux with $Sv_0 = 0.1$ weakens w_e^{eva} by approximately 40% while imposing a strong shear with

$Sh_o = 10$ amplifies w_e^{eva} by approximately 40%. Figure 6e,f further shows the sedimentation weakening of w_e^{eva} is to leading order independent of shear and that the shear enhancement of w_e^{eva} is to leading order independent of sedimentation. This indicates that coupling processes between sedimentation weakening and shear enhancement of w_e^{eva} remain moderate.

Regarding their effect on the radiative cooling contribution w_e^{rad}, we observe that droplet sedimentation and wind shear can partly compensate each other as well (Figure 6g,h). While sedimentation removes liquid water from the EIL, which weakens w_e^{rad}, shear does the opposite and puts additional liquid water into the EIL, which enhances w_e^{rad}. In any case, the magnitude of the radiative cooling contribution is small compared to w_e^{tur} and w_e^{eva} (note the different vertical scale in Figure 6h) and therefore quantifying sedimentation and shear effects on w_e^{rad} has no priority for atmospheric conditions similar to those in the RF01 of DYCOMS-II. However, we emphasize once more that the net radiative cooling (i.e., integrated across the whole CTML) remains comparable to the net evaporative cooling for all sedimentation and shear numbers investigated, as discussed in section 4.1.

5 SUMMARY AND CONCLUSION

Direct numerical simulations (DNSs) of the stratocumulus cloud-top have been employed to show that droplet-sedimentation and wind-shear effects on cloud-top entrainment can completely compensate each other for subtropical conditions. Droplet-sedimentation and wind-shear effects have been analyzed by means of an integral analysis of the buoyancy equation, which allows us to analytically decompose the mean entrainment velocity $w_e = dz_i/dt$ into contributions from droplet sedimentation, w_e^{sed}, turbulent mixing, w_e^{tur}, radiative cooling, w_e^{rad}, and evaporative cooling, w_e^{eva}. We observe that droplet sedimentation and wind shear mainly alter w_e^{sed}, w_e^{tur} and w_e^{eva}, while their effect on w_e^{rad} are small. Wind shear enhances w_e^{eva} by amplifying the mixing of free-tropospheric and cloudy air, while droplet sedimentation does the opposite and weakens w_e^{eva} by removing cloudy air from the entrainment interfacial layer and thus preventing cloud droplets from evaporating. In addition, wind shear promotes a positive turbulent buoyancy flux contribution w_e^{tur} that directly enhances entrainment, while droplet sedimentation promotes a negative sedimentation buoyancy flux contribution w_e^{sed} that directly opposes entrainment. For a strongly sheared cloud-top, droplet sedimentation weakens entrainment also indirectly by broadening the entrainment interfacial layer, which causes a weakening of w_e^{tur}.

The importance of the various compensating mechanisms introduced in the previous paragraph strongly depends on the choice of the reference height z_i where w_e^{sed}, w_e^{tur}, and w_e^{eva} are calculated, even though different definitions of the reference height z_i typically differ only by a few meters. For instance, for a strongly sheared cloud-top and for reference heights near to the height of zero mean buoyancy $z_{i,n}$ (the base of the capping inversion), the sedimentation weakening of w_e is primarily caused by changes in w_e^{eva} and to a lesser degree by changes w_e^{sed}, while for reference heights near to the height of minimum turbulent buoyancy flux $z_{i,f}$, the sedimentation weakening of w_e is primarily caused by changes in w_e^{tur} and to a lesser degree by changes w_e^{eva}. Hence, entrainment-rate parametrizations should estimate contributions from different processes at the same reference height.

We further find that the sedimentation weakening of the entrainment velocity w_e is nearly shear independent, while the shear enhancement of the entrainment velocity w_e can moderately depend on sedimentation as sedimentation weakens the turbulent buoyancy flux contribution w_e^{tur} for a strongly sheared cloud-top. For instance, a strong sedimentation with a bulk sedimentation velocity of $u_{sed} \simeq 30\,\mathrm{mm\,s^{-1}}$ weakens the mean entrainment velocity by approximately 40% irrespectively of the imposed shear strength, while imposing a wind shear characterized by a cloud-top velocity jump of $\Delta u \simeq 3\,\mathrm{m\,s^{-1}}$

enhances w_e by approximately 40% for a moderate sedimentation with $u_{sed} \simeq 13\,\mathrm{mm\,s^{-1}}$, and by approximately 30% for a strong sedimentation with $u_{sed} \simeq 30\,\mathrm{mm\,s^{-1}}$ (at the height of zero mean buoyancy $z_{i,n}$).

Last but not least, we also find that, even in the presence of droplet sedimentation, wind-shear enhancement of w_e is only observed once the cloud-top velocity jump Δu exceeds its critical value $(\Delta u)_{crit}$, as obtained previously without droplet sedimentation (Schulz and Mellado, 2018). We find $(\Delta u)_{crit} \simeq 4 - 5w_* \simeq 1 - 4\,\mathrm{ms^{-1}}$ for typical values of the convective velocity scale $w_* \simeq 0.2 - 0.9\,\mathrm{m\,s^{-1}}$ (Wood, 2012), where variations in the prefactor of w_* characterize droplet-sedimentation effects. This shows that droplet-sedimentation effects on $(\Delta u)_{crit}$ remain moderate (below 25%), which indicates that $(\Delta u)_{crit}$ remains a useful quantity for characterizing wind-shear effects even in the case of strong droplet sedimentation.

In summary, this work demonstrates that the mean entrainment velocity can be equally sensitive towards changes in the sedimentation strength and towards changes in cloud-top wind shear. This result implies that entrainment parametrizations should pay equal attention to droplet-sedimentation and to wind-shear effects. Besides, this result implies that the droplet size distribution can substantially affect cloud lifetimes not only because of its effect on rain formation but also because of its effect on cloud-top entrainment, which emphasizes the importance of precise measurements of the droplet size distribution and of appropriate representations of it in numerical models.

Acknowledgments

A   REYNOLDS NUMBER EFFECTS

Reynolds number effects for sedimentation alone and for shear alone are observed to be less than 20% when increasing the Reynolds number by a factor of two in (Lozar and Mellado, 2017) and by a factor of up to three in (Schulz and Mellado, 2018) respectively. A detailed discussion of Reynolds number effects is given in (Schulz and Mellado, 2018; Mellado et al., 2018) and here we only analyze three cases, namely $\{Sh_0 = 0, Sv_0 = 0.0\}$, $\{Sh_0 = 10, Sv_0 = 0.0\}$, $\{Sh_0 = 10, Sv_0 = 0.1\}$. Figure 7 shows that for those three cases most presented quantities vary by less than 20% when increasing the Reynolds numbers by a factor of up to three. A notable exception is that the shear production term $P = -\langle u'w' \rangle \partial_z \langle u \rangle$ varies by up to 50% (corresponding to $0.3B_0$) when doubling the Reynolds number for the case $\{Sh_0 = 10, Sv_0 = 0.1\}$. However, despite this large number, the relative change of the shear production term P with sedimentation, that is how the difference $P_{Sh_0=10,Sv_0=0.0} - P_{Sh_0=10,Sv_0=0.1}$ changes with Re_0, varies by less than 10% with when doubling the Reynolds number. This indicates that our low-to-moderate Reynolds number simulations adequately represent sedimentation effects on the shear production term. Reynolds number effects on net evaporative cooling E_0 and on the normalized quasi-steady entrainment velocity $[(w_e - w_e^{def})/W_{ref}]_{z_{i,n}}$ are not presented in Figure 7 but are also found to be below 20% for the three analyzed cases. This tendency towards Reynolds number similarity is a general characteristic of turbulent flows (Dimotakis, 2005; Mellado et al., 2018) and allows us to partly extrapolate our results to atmospheric conditions.
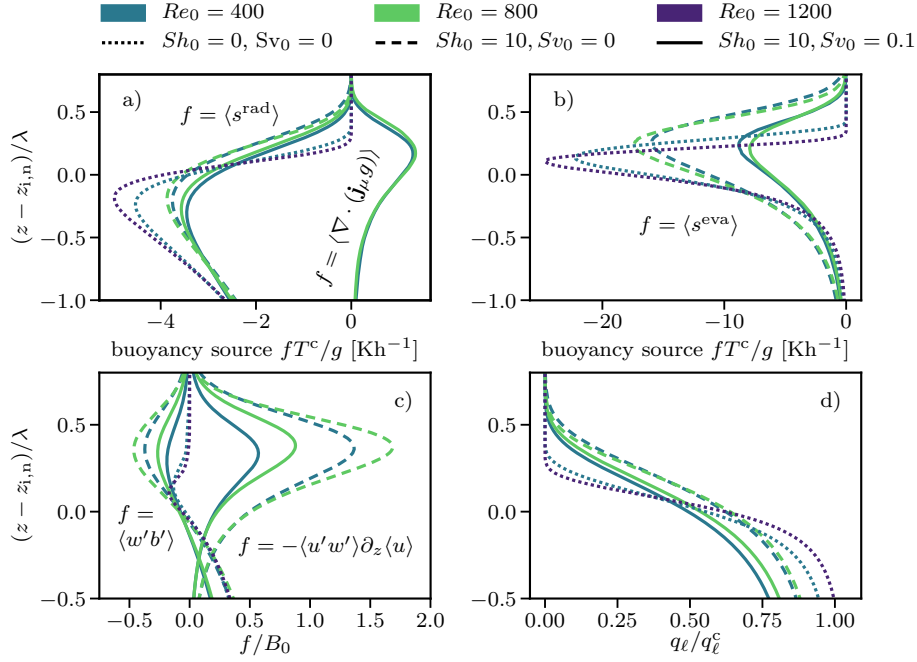
Figure 7: Panel. a) + b) show the different buoyancy source terms (cf. Figure 4) according to Eq. (13), panel c) shows the normalized turbulent buoyancy flux and the normalized shear production term (cf. Figure 3), and panel d) shows the normalized liquid water specific humidity. Different colors indicates different Reynolds numbers and different line styles indicate different sedimentation and shear numbers. Besides, all presented plots are averaged over the period $7.5 < z_*/\lambda < 8.5$ (cf. Table 1).

B   SEDIMENTATION AND SHEAR EFFECTS ON THE EIL THICKNESS

The derivation of the critical cloud-top velocity jump $(\Delta u)_{\mathrm{crit}}$ introduced in section 3.2 is based on the observation that the EIL thickness h_{EIL} is scaled by two different length scales, namely, the penetration depth δ and the shear layer thickness h_{S}. Details of the derivation can be found in Schulz and Mellado (2018) and in the following we only discuss the combined effect of sedimentation and shear on these two scalings of the EIL thickness.

First, h_{EIL} is scaled by the sum of the penetration depth δ and the diffusive thickness h_{diff} as indicated in Figure 8a. The penetration depth δ characterizes the depth that in-cloud turbulent convection can penetrate into the stably stratified EIL and is defined as twice the difference between the height of minimum turbulent buoyancy flux $z_{\mathrm{i,f}}$ and the height of zero mean buoyancy $z_{\mathrm{i,n}}$, that is

$$\delta = 2(z_{\mathrm{i,f}} - z_{\mathrm{i,n}}) \,. \tag{16}$$

The diffusive thickness h_{diff} accounts for low-to-moderate Reynolds number artifacts as elucidated in detail in Mellado et al. (2010), Lozar and Mellado (2015b), and Schulz and Mellado (2018). Moreover, Figure 8a shows that sedimentation effects on the scaling of h_{EIL} with $\delta + h_{\mathrm{diff}}$ is on the order of 20%, and this effect decreases as shear intensifies.

Second, for a sufficiently strong shear h_{EIL} is scaled by the sum of the critical shear layer thickness h_{S} and the diffusive thickness h_{diff} as indicated in Figure 8b. The critical shear layer thickness h_{S} characterizes the vertical extent of wind-shear effects and is defined according to Mellado, Stevens, and Schmidt (2014) as
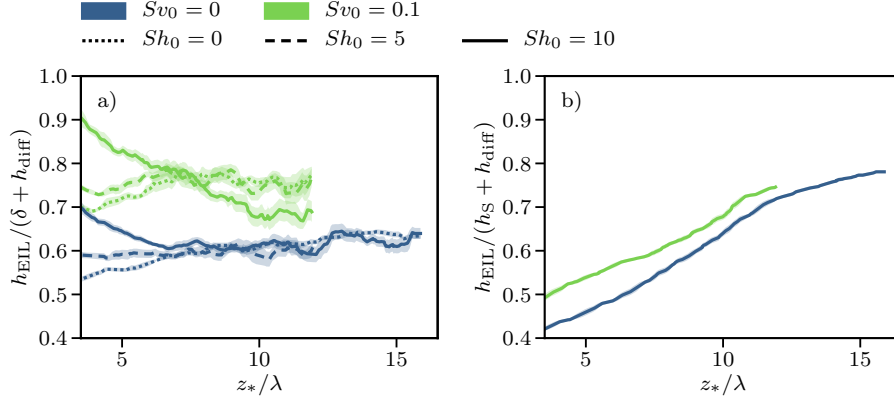
$$h_{\mathrm{S}} = \frac{(\Delta u)^2}{3\Delta b} \,, \tag{17}$$

Figure 8: Panels a) shows the entrainment interfacial layer thickness h_{EIL} normalized by the sum of the penetration depth δ and the diffusive thickness h_{diff}. Panel b) shows h_{EIL} normalized by the sum of the critical shear layer thickness h_{S} and the diffusive thickness h_{diff}. Shaded areas indicate two standard deviations around the mean. The figure is presented for $Re_0 = 400$.

where the subscript 'S' indicates shear. Figure 8b shows that sedimentation effects on the scaling $h_{\mathrm{EIL}}/(h_{\mathrm{S}} + h_{\mathrm{diff}})$ are less than 10%, which indicates that those effects are negligible to leading order. boundary layers (Mahrt and Lenschow, 1976; Fedorovich and Conzemius, 2008), and can be associated with a critical value of the shear Richardson number $Ri_{\mathrm{S}} = h_{\mathrm{EIL}}\Delta b/(\Delta u)^2$. We emphasize that h_{S} is an horizontally averaged and asymptotic quantity. Locally in-cloud turbulent convection penetrates into the stably stratified EIL, which thins the shear layer and thus enables cloud-top shear to create further shear instabilities. Without this thinning process shear-generated turbulence would decay once the EIL reaches its critical thickness h_{S}. Further details regarding h_{S} are given in (Schulz and Mellado, 2018). All this shows that the entrainment interfacial layer thickness h_{EIL} is equally well scaled by the sum $h_{\mathrm{S}} + h_{\mathrm{diff}}$ and by the sum $\delta + h_{\mathrm{diff}}$ for a strongly sheared cloud-top with $Sh_0 = 10$. This indicates that convection and wind shear are similarly important for determining entrainment at this shear number. The case of very strong shear with $h_{\mathrm{EIL}} \simeq h_{\mathrm{S}} + h_{\mathrm{diff}} \gg \delta + h_{\mathrm{diff}}$, which is considered in Mellado, Stevens, and Schmidt (2014), is not investigated in the presented study.

C THE ENTRAINMENT RATE EQUATION

The buoyancy evolution equation (see Eq. (13)), as explained in Lozar and Mellado (2015b, 2017), can be written as

$$D_t b = \kappa_T \nabla^2 b + s^{\mathrm{rad}} + s^{\mathrm{eva}} + \nabla \cdot (\mathbf{j}_\mu g) + C(\epsilon) , \tag{18}$$

where κ_T is the thermal diffusive and the radiative and evaporative source term are defined as

$$s^{\mathrm{rad}} = \left[1 - \frac{\beta_l q_\ell^{\mathrm{c}}}{\psi_{\mathrm{sat}}} \right] \frac{g \nabla \cdot \mathbf{R}}{c_p^{\mathrm{c}} T^{\mathrm{c}}} \quad \text{and} \tag{19}$$

$$s^{\mathrm{eva}} = g \beta^\ell q_\ell^{\mathrm{c}} \left[\frac{-(\partial_t q_\ell)_{\mathrm{pha}}}{q_\ell^{\mathrm{c}}} + \frac{d_\xi f \nabla \cdot \mathbf{R}}{\psi_{\mathrm{sat}} c_p^{\mathrm{c}} T^{\mathrm{c}}} \right] . \tag{20}$$

The parameter ψ_{sat} quantifies radiative effects at saturation conditions and β^ℓ specifies phase change effects of the buoyancy. Due to condensational warming only a part β of the radiatively induced enthalpy changes translates into buoyancy changes, where β is given by $\beta = (1 - \beta^\ell q_\ell^{\mathrm{c}} \psi_{\mathrm{sat}}^{-1}) \simeq 0.53$ and condensational warming is also the origin of the second summand in Eq. (20). Besides, $\mathbf{R} = R\mathbf{k}$ is the one-dimensional longwave radiative forcing

based on Larson, Kotenberg, and Wood (2007), with $\mathbf{k}$ being a unit vector pointing in the vertical direction. The net longwave radiative flux $R = R(z)$ can be well approximated by $R = R_o \exp\left[-\lambda^{-1} \int_z^{z_{top}} q_\ell / q_\ell^c dz'\right]$, where R_o is the net radiative flux cooling the cloud-top region and λ is the extinction length. The sedimentation buoyancy flux $\mathbf{j}_\mu$ is defined in Eq. (2). The function $C(\epsilon)$ is a correction factor that results from the smoothing of the liquid function $\ell(\xi, \epsilon)$ as discussed in Lozar and Mellado (2017). In the limit $\epsilon \to 0$ the correction term vanishes, however, $\epsilon = 1/16$ produces a small integrated correction term equal to 10% of the sedimentation buoyancy flux [i.e., $\int C(1/16)dV \sim 0.1\mathbf{j}_\mu g \cdot \mathbf{k}$].

The entrainment rate equation $w_e = w_e^{tur} + w_e^{sed} + w_e^{eva} + w_e^{rad} + w_e^{mol} + w_e^{def}$ (see Eq. (14)) is obtained by integrating the buoyancy evolution equation from an arbitrary reference height $z = z_i$ upwards (see Mellado et al., 2018, for details). The single contributions are defined as follows:

$$w_e^{tur}(b^d - \langle b \rangle_{z_i}) = -\langle w'b' \rangle_{z_i} \tag{21}$$

$$w_e^{sed}(b^d - \langle b \rangle_{z_i}) = \langle \mathbf{j}_\mu g \cdot \mathbf{k} \rangle_{z_i} \tag{22}$$

$$w_e^{eva}(b^d - \langle b \rangle_{z_i}) = E_o - \langle E \rangle_{z_i} \tag{23}$$

$$w_e^{rad}(b^d - \langle b \rangle_{z_i}) = \beta g (c_p^c T^c)^{-1}(R_o - \langle R \rangle_{z_i}) \tag{24}$$

$$w_e^{mol}(b^d - \langle b \rangle_{z_i}) = \kappa_T \partial_z \langle b \rangle_{z_i} , \tag{25}$$

$$w_e^{def}(b^d - \langle b \rangle_{z_i}) = -\frac{d}{dt} \int_{z_i}^{z_\infty} (b^d - \langle b \rangle(z))dz. \tag{26}$$

REFERENCES

Ackerman, Andrew S et al. (2004). "The impact of humidity above stratiform clouds on indirect aerosol climate forcing". In: *Nature* 432.7020, p. 1014.

Ackerman, Andrew S et al. (2009). "Large-eddy simulations of a drizzling, stratocumulus-topped marine boundary layer". In: *Monthly Weather Review* 137.3, pp. 1083–1110.

Bailon-Cuba, Jorge, Mohammad S Emran, and Jörg Schumacher (2010). "Aspect ratio dependence of heat transfer and large-scale flow in turbulent convection". In: *Journal of Fluid Mechanics* 655, pp. 152–173.

Bretherton, CS, Peter N Blossey, and Junya Uchida (2007). "Cloud droplet sedimentation, entrainment efficiency, and subtropical stratocumulus albedo". In: *Geophysical research letters* 34.3.

Brost, RA, JC Wyngaard, and DH Lenschow (1982). "Marine stratocumulus layers. Part II: Turbulence budgets". In: *Journal of the Atmospheric Sciences* 39.4, pp. 818–836.

Caughey, SJ, BA Crease, and WT Roach (1982). "A field study of nocturnal stratocumulus II Turbulence structure and entrainment". In: *Quarterly Journal of the Royal Meteorological Society* 108.455, pp. 125–144.

Deardorff, JW (1980a). "Cloud top entrainment instability". In: *Journal of the Atmospheric Sciences* 37.1, pp. 131–147.

Deardorff, James W (1980b). "Stratocumulus-capped mixed layers derived from a three-dimensional model". In: *Boundary-Layer Meteorology* 18.4, pp. 495–527.

Dimotakis, Paul E (2005). "Turbulent mixing". In: *Annu. Rev. Fluid Mech.* 37, pp. 329–356.

Driedonks, AGM and PG Duynkerke (1989). "Current problems in the stratocumulus-topped atmospheric boundary layer". In: *Boundary-Layer Meteorology* 46.3, pp. 275–303.

Faloona, Ian et al. (2005). "Observations of entrainment in eastern Pacific marine stratocumulus using three conserved scalars". In: *Journal of the atmospheric sciences* 62.9, pp. 3268–3285.

Fedorovich, Evgeni and Robert Conzemius (2008). "Effects of wind shear on the atmospheric convective boundary layer structure and evolution". In: *Acta Geophysica* 56.1, pp. 114–141.

Gerber, H, Szymon P Malinowski, and Haflidi Jonsson (2016). "Evaporative and radiative cooling in POST Stratocumulus". In: *Journal of the Atmospheric Sciences* 73.10, pp. 3877–3884.

Gerber, H et al. (2005). "Holes and entrainment in stratocumulus". In: *Journal of the atmospheric sciences* 62.2, pp. 443–459.

Glienke, S et al. (2017). "Cloud droplets to drizzle: Contribution of transition drops to microphysical and optical properties of marine stratocumulus clouds". In: *Geophysical Research Letters* 44.15, pp. 8002–8010.

Grosvenor, Daniel P et al. (2018). "Remote sensing of droplet number concentration in warm clouds: A review of the current state of knowledge and perspectives". In: *Reviews of Geophysics*.

Haman, Krzysztof E et al. (2007). "Small scale mixing processes at the top of a marine stratocumulus—A case study". In: *Quarterly Journal of the Royal Meteorological Society* 133.622, pp. 213–226.

Hill, Adrian A, Graham Feingold, and Hongli Jiang (2009). "The influence of entrainment and mixing assumption on aerosol–cloud interactions in marine stratocumulus". In: *Journal of the Atmospheric Sciences* 66.5, pp. 1450–1464.

Hudson, James G and Seong Soo Yum (1997). "Droplet spectral broadening in marine stratus". In: *Journal of the atmospheric sciences* 54.22, pp. 2642–2654.

Katzwinkel, J, H Siebert, and RA Shaw (2012). "Observation of a self-limiting, shear-induced turbulent inversion layer above marine stratocumulus". In: *Boundary-layer meteorology* 145.1, pp. 131–143.

Kopec, Marta K, Szymon P Malinowski, and Zbigniew P Piotrowski (2016). "Effects of wind shear and radiative cooling on the stratocumulus-topped boundary layer". In: *Quarterly Journal of the Royal Meteorological Society* 142.701, pp. 3222–3233.

Larson, Vincent E, Kurt E Kotenberg, and Norman B Wood (2007). "An analytic longwave radiation formula for liquid layer clouds". In: *Monthly weather review* 135.2, pp. 689–699.

Lele, Sanjiva K (1992). "Compact finite difference schemes with spectral-like resolution". In: *Journal of computational physics* 103.1, pp. 16–42.

Lilly, Douglas K (1968). "Models of cloud-topped mixed layers under a strong inversion". In: *Quart. J. Roy. Meteor. Soc* 94.401, pp. 292–309.

Lozar, A de and JP Mellado (2014). "Cloud droplets in a bulk formulation and its application to buoyancy reversal instability, QJ Roy". In: *Meteor. Soc* 140, pp. 1493–1504.

Lozar, Alberto de and Juan Pedro Mellado (2015a). "Evaporative cooling amplification of the entrainment velocity in radiatively driven stratocumulus". In: *Geophysical Research Letters* 42.17, pp. 7223–7229.

— (2015b). "Mixing driven by radiative and evaporative cooling at the stratocumulus top". In: *Journal of the Atmospheric Sciences* 72.12, pp. 4681–4700.

— (2017). "Reduction of the entrainment velocity by cloud droplet sedimentation in stratocumulus". In: *Journal of the Atmospheric Sciences* 74.3, pp. 751–765.

Mahrt, L and DH Lenschow (1976). "Growth dynamics of the convectively mixed layer". In: *Journal of the Atmospheric Sciences* 33.1, pp. 41–51.

Malinowski, SP et al. (2013). "Physics of Stratocumulus Top (POST): turbulent mixing across capping inversion". In: *Atmospheric Chemistry and Physics* 13.24, pp. 12171–12186.

Martin, GM, DW Johnson, and An Spice (1994). "The measurement and parameterization of effective radius of droplets in warm stratocumulus clouds". In: *Journal of the Atmospheric Sciences* 51.13, pp. 1823–1842.

Mellado, Juan Pedro (2010). "The evaporatively driven cloud-top mixing layer". In: *Journal of Fluid Mechanics* 660, pp. 5–36.

— (2012). "Direct numerical simulation of free convection over a heated plate". In: *Journal of Fluid Mechanics* 712, pp. 418–450.

— (2017). "Cloud-Top Entrainment in Stratocumulus Clouds". In: *Annual Review of Fluid Mechanics* 49, pp. 145–169.

Mellado, Juan Pedro and Cedrick Ansorge (2012). "Factorization of the Fourier transform of the pressure-Poisson equation using finite differences in colocated grids". In: *ZAMM-Journal of Applied Mathematics and Mechanics/Zeitschrift für Angewandte Mathematik und Mechanik* 92.5, pp. 380–392.

Mellado, Juan Pedro, Bjorn Stevens, and Heiko Schmidt (2014). "Wind shear and buoyancy reversal at the top of stratocumulus". In: *Journal of the Atmospheric Sciences* 71.3, pp. 1040–1057.

Mellado, Juan Pedro et al. (2010). "Two-fluid formulation of the cloud-top mixing layer for direct numerical simulation". In: *Theoretical and Computational Fluid Dynamics* 24.6, pp. 511–536.

Mellado, Juan-Pedro et al. (2018). "DNS and LES for simulating stratocumulus: Better together". In: *Journal of Advances in Modeling Earth Systems*.

Miles, Natasha L, Johannes Verlinde, and Eugene E Clothiaux (2000). "Cloud droplet size distributions in low-level stratiform clouds". In: *Journal of the atmospheric sciences* 57.2, pp. 295–311.

Nicholls, S and J Leighton (1986). "An observational study of the structure of stratiform cloud sheets: Part I. Structure". In: *Quarterly Journal of the Royal Meteorological Society* 112.472, pp. 431–460.

Pawlowska, Hanna and Jean-Louis Brenguier (2000). "Microphysical properties of stratocumulus clouds during ACE-2". In: *Tellus B* 52.2, pp. 868–887.

Randall, David A (1980). "Conditional instability of the first kind upside-down". In: *Journal of the Atmospheric Sciences* 37.1, pp. 125–130.

Roode, Stephan R de and Qing Wang (2007). "Do stratocumulus clouds detrain? FIRE I data revisited". In: *Boundary-layer meteorology* 122.2, pp. 479–491.

Schulz, Bernhard and Juan Pedro Mellado (2018). "Wind-Shear Effects on Radiatively and Evaporatively Driven Stratocumulus Tops". In: *Journal of the Atmospheric Sciences* 2018.

Stevens, Bjorn (2005). "Atmospheric moist convection". In: *Annu. Rev. Earth Planet. Sci.* 33, pp. 605–643.

Stevens, Bjorn et al. (2003). "On entrainment rates in nocturnal marine stratocumulus". In: *Quarterly Journal of the Royal Meteorological Society* 129.595, pp. 3469–3493.

VanZanten, MC et al. (2005). "Observations of drizzle in nocturnal marine stratocumulus". In: *Journal of the atmospheric sciences* 62.1, pp. 88–106.

Wang, S, X Zheng, and Q Jiang (2012). "Strongly sheared stratocumulus convection: an observationally based large-eddy simulation study". In: *Atmospheric Chemistry and Physics* 12.11, pp. 5223–5235.

Wood, Robert (2000). "Parametrization of the effect of drizzle upon the droplet effective radius in stratocumulus clouds". In: *Quarterly Journal of the Royal Meteorological Society* 126.570, pp. 3309–3324.

— (2012). "Stratocumulus clouds". In: *Monthly Weather Review* 140.8, pp. 2373–2423.

ACKNOWLEDGMENTS

First and foremost I would like to thank Juan Pedro Mellado for being a great supervisor. Your enthusiasm for understanding fluid dynamical aspects of clouds was always inspiring and provided continual encouragement. I am also most grateful to Bjorn Stevens and Gualtiero Badin for motivating, instructive discussions, and for providing guidance over the last 3.5 years. Moreover, a special thanks goes to Armin Haghshenas for being a marvelous office mate. It was great always having had somebody with whom I could discuss my daily buisness. A big thanks also goes to Katherine Fodor, Mortiz Hartmann, Mona Karimi, and Alberto de Lozar for complementing our group on turbulent mixing processes and for being helpful in so many different ways. In addition, I would like to thank Szymon P. Malinowski for all the inspiring discussions we had at several conferences and for being such a welcoming host in Warsaw. I would also like to thank Julia Windmiller and David Leutwyler for doing the internal review of my two papers. Furthermore, I am most grateful to the IMPRS[1] office, namely to Antje Weitz, Cornelia Kampmann, and Michaela Born, without your support and help my PhD life would have been much more burdensome. I was also most lucky of having had a wonderful group of PhD colleagues. It was your friendship, your support, and your creativity who made the IMPRS such a welcoming and positive place. However, it is an impossible task to name all of you without forgetting somebody. So I would like to thank you all! Nonetheless, since lunch breaks are such an essential part of doing a PhD, I would like to thank Lukas Krönert, Tobias Becker, Tobias Haufschild, Sebastian Müller, Hauke Schulz, and Leonore Jungandreas for being frequent and great lunch companions. A big thanks also goes to all the people from the atmosphere department, your supportive and welcoming attitude was exceptionally nice. I am also grateful for the remarkably good support from the administration and from the Scientific Computing Laboratory (SCLab).

Last but not least, I am incredibly lucky of having my partner Sandra. Your love, your laughs, and your support are meaning the world to me! Moreover, I am most grateful to Daniel and Luisa for supporting me in so many different ways—thanks for sharing so many delicious meals with me. For a very similar reason a big thanks also goes to my current roommate Veit. In addition, I would like to thank all the 'couch-potatos' I have spent so many Tuesday (and Wednesday) evenings with. Without you my life in Hamburg would have been much more one-dimensional. Above all, I am most grateful for my family, it is great to have you! Finally, this thesis is dedicated to my parents Margarete and Christian. Without your love and invaluable support I would not have written this dissertation.

---

1 International Max Planck Research School on Earth System Modelling

AFFIRMATION ON OATH

Hiermit versichere ich an Eides statt, dass ich die vorliegende Dissertation mit dem Titel: 'On the Role of Wind Shear and Cloud Droplet Sedimentation on Entrainment in Stratocumulus' selbstständig verfasst und keine anderen als die angegebenen Hilfsmittel – insbesondere keine im Quellenverzeichnis nicht benannten Internet-Quellen – benutzt habe. Alle Stellen, die wörtlich oder sinngemäß aus Veröffentlichungen entnommen wurden, sind als solche kenntlich gemacht. Ich versichere weiterhin, dass ich die Dissertation oder Teile davon vorher weder im In- noch im Ausland in einem anderen Prüfungsverfahren eingereicht habe und die eingereichte schriftliche Fassung der auf dem elektronischen Speichermedium entspricht.

Hamburg, Mai 2019

<div style="text-align:right">

_____

Bernhard Schulz

</div>

Hinweis / Reference

Die gesamten Veröffentlichungen in der Publikationsreihe des MPI-M
„Berichte zur Erdsystemforschung / Reports on Earth System Science",
ISSN 1614-1199

sind über die Internetseiten des Max-Planck-Instituts für Meteorologie erhältlich:
http://www.mpimet.mpg.de/wissenschaft/publikationen.html

All the publications in the series of the MPI -M
„Berichte zur Erdsystemforschung / Reports on Earth System Science",
ISSN 1614-1199

are available on the website of the Max Planck Institute for Meteorology:
http://www.mpimet.mpg.de/wissenschaft/publikationen.html